SPATIAL REGULATION OF RAS SIGNALING STUDIED WITH CORRELATIVE SUPER-RESOLUTION AND ELECTRON MICROSCOPY

By

Ying Zhang

A DISSERTATION

Presented to the Department of Biomedical Engineering

and the Oregon Health & Science UniversityS

School of Medicine

In partial fulfillment of

the requirements for the degree of

DOCTOR OF PHILOSOPHY

August 2018

School of Medicine

Oregon Health & Science University

CERTIFICATE OF APPROVAL

This is to certify that the PhD dissertation of

Ying Zhang

has been approved

Xiaolin Nan, Ph.D. (Mentor/Advisor)

Eric Barklis, Ph.D.

James Korkola, Ph.D.

Young Hwan Chang, Ph.D.

Owen McCarty, Ph.D.

TABLE OF CONTENTS

LIST OF FIGURES

LIST OF TABLES

LIST OF ABBREVIATIONS

AFM	Atomic force microscopy
BSE	Backscattered electron
CCP	Clathrin-coated pit
CLEM	Correlative light and electron microscopy
CPD	Critical point drying
CRD	Cysteine-rich domain
DNA-PAINT	DNA-based point accumulation for imaging in nanoscale topography
DRM	Detergent-resistant membrane
DS	Docking strand
EGF	Epidermal growth factor
EGFR	Epidermal growth factor receptor
EM	Electron microscopy
ERK	Extracellular signal-regulated kinases
FM	Fluorescence microscopy
FRAP	Fluorescence recovery after photobleaching
FRET	Förster resonance energy transfer
FTase	Farnesyltransferase
GA	Glutaraldehyde
GAP	GTPase activating protein
GDP	Guanosine diphosphatase
GEF	Guanine exchange factors
GPI	Glycosylphosphatidylinositol
GRB2	Growth factor receptor-bound protein 2
GTP	Guanosine triphosphate
HMDS	Hexamethyldisilazane
HVR	Hyperviable region
ICMT	Isoprenylcysteine carboxylmethyltransferase
IS	Imaging strand
MAPK	Mitogen-activated protein kinases
MEK	Mitogen-activated protein kinases
PALM	Photoactivated localization microscopy
PDEδ	Phosphodiesterase δ-subunit
PFA	Paraformaldehyde
PI3K	Phosphatidylinositide 3-kinases
PIP	Phosphoinositol phosphate
PS	Phosphatidylserine
Raf	Rapidly accelerated fibrosarcoma
RALGDS	Ral guanine nucleotide dissociation stimulator

Ras	Rat sarcoma
RBD	Ras binding protein
RCE1	Ras-converting enzyme 1
RTK	Receptor tyrosine kinase
SE	Secondary electron
SEM	Scanning electron microscopy
SMLM	Single-molecule localization microscopy
SMT	Single molecule tracking
SOS1	Son of sevenless homolog 1
SPT	Single particle tracking
SRM	Super-resoluiton microscopy
STORM	Stochastic optical reconstruction microscopy
TEM	Transmission electron microscopy
tH	C-terminal tail of H-Ras
TIAM	Tumor invation and metastasis inducing protein
tK	C-terminal tail of K-Ras
UA	Uranyl acetate

ACKNOWLEDGEMENTS

First and foremost I want to thank my advisor Prof. Xiaolin Nan. It has been an honor to be his first Ph.D. student. Xiaolin provided me with every bit of guidance, assistance and expertise during my first two years; and then when I felt ready to explore the research on my own, Xiaolin gave me the freedom and support to do the projects that I was interested with. I appreciate all his contribution of time, ideas and funding to make my Ph.D experience productive and stimulating. On a personal level, Xiaolin inspired me by his hardworking and passionate attitude, which are contagious and motivational to me for my future career.

Besides my advisor, I would like to thank the rest of my dissertation committee, Eric Barklis, James Korkola, Young Hwan Chang and Owen McCarty for their great support and invaluable advice. I am thankful to Prof. Barklis, for serving as my committee chair and for his crucial advice that shaped my thesis. I am also grateful to Prof. Korkola for providing his insightful expertise in cancer biology. I am especially appreciative of Prof. Chang for his extensive contribution to image analysis on my project. I am also thankful to Prof. McCarty, an excellent collaborator and student mentor, for guiding me how to complete Ph.D within specific time frame.

I would like to thank my lab mates for their continued support. The group has been a source of friendships as well as good advice and collaboration. I am especially grateful to the former lab members Andrew Nickerson, Dr. Li-Jung Lin and Dr. Tao Huang, for their patience in answering my naïve questions and for the professional training they provided when I first joined the lab. I would like to acknowledge Yerim Lee for her work of Matlab

coding and image analysis, and Lei Wu for his help with western blot. Other past and present group members that I have had the pleasure to work with or alongside of are grad students Jing Wang and Elliot Gray; postdocs Mo Chen and Carey Phelps; research assistant Alec Peters; and the numerous summer interns who have come through the lab.

The thesis would not have come to a successful completion without the help I received from all my collaborators. I am very thankful to the staff at Multiscale Microscopy Core, Claudia Lopez, Jessica Riesterer, Melissa Williams and Danielle Jorgens, who trained me with using electron microscopies and EM sample preparation. I would also like to thank my collaborators from Cancer Early Detection Advanced Research Center, Matthew Rames, Fehmi Civitci and Ting Zheng for their input with the DNA-PAINT project. My other collaborators, Anke Mulder, Shinji Iizuka and Sunjong Kwon, have taught me with different aspects of cancer biology and advanced imaging.

Lastly, I would like to thank my parents for all their love and encouragement. They raised me with a love of science and supported me in all my pursuits. They are the best parents a daughter could ask for and I am so lucky to have you two as my role models. Thank you.

Chapter I. Introduction

A defining characteristics of biological signaling is that it is both robust and versatile: the system can respond to a wide variety of inputs and consistently generate outputs specific to each input. This gives the ability for biological systems to adapt to complex environments for optimal fitness. How such robustness and versatility are achieved at once, however, has not been well understood. One effective strategy would be to spatially contain specific signaling modules in specific structures. As such, signaling specificity is ensured by putting specific upstream and downstream components in the same space, and versatility is achieved with the large number of component and structure combinations.

The cell is rich in structures that vary in spatial and time scales, shape and composition, and chemical and physical properties, giving rise to limitless scenarios where spatial regulation of signaling or other processes could be implemented. It has long been appreciated that most processes take place at distinct subcellular compartments such as the membrane, cytoplasm, nucleus, or other specialized organelles. With ever more common use of high resolution imaging approaches, it has also become clear that spatial regulation can take place at the nanometer or molecular scales. The plasma membrane, for example, has been increasingly recognized as a heterogeneous system comprising of nano to microscale domains, each of which comprising distinct subsets of lipids and proteins participating in different biological processes.

Among the numerous molecules that function at the cell membrane, the Ras small GTPases are prototypical examples of spatial regulation. The Ras family of GTPases is of central importance for their roles in human health and disease. As will be discussed in

detail in this chapter, formation of nanoscale domains comprising of specific Ras isoforms, lipids, cytoskeletal and other protein components is both a requirement and a primary means to organize and coordinate signaling of the tens of Ras isoforms. In this chapter, we begin with the basic biology of Ras and its best characterized effector, Raf, followed by discussions on current knowledge on the spatial mechanisms that regulate Ras signaling in cells, and will close the chapter with an outline of the thesis.

1.1. Fundamentals of Ras biology

1.1.1. Ras family of GTPase

The Ras (Rat sarcoma) proteins are small GTPase involved in cellular signal transduction. The Ras family is one of the five major families of GTPases in a larger Ras superfamily, with each family distinguished by their protein structure, sequence and function. The five main families are Ras, Rho, Arf, Ran and Rab. Physiological and pathological processes controlled by Ras superfamily proteins range from cell growth, proliferation and transformation to transport, cell motility, and adhesion [1].

The Ras family of proteins can be further classified into 7 subgroups, Ras, Rap, Ral, R-Ras, Rit/Rin, Rheb, and ARRHI/Di-Ras, according to sequence homology and protein function [2]. Discovery of the *RAS* genes dates back to the 1960s when cancer research focused on tumorigenic viruses, then thought to be the main cause of cancer. The *RAS* genes were initially identified as retroviral oncogenes from the genome of Harvey and Kirsten rat sarcoma viruses [3,4], which were later recognized as parts of the human *HRAS* and *KRAS*2 oncogenes, respectively, by Scolnick and colleagues in the late 1970s to early

1980s [5,6]. Thereafter, these genes were found to encode 21kDa membrane-associated proteins [7] that bind GDP and GTP [8], establishing Ras as a family of membrane associated GTP-binding proteins.

As GTPases, Ras can switch between an active GTP-bound state and an inactive GDP-bound state (Fig 1.1). GDP-bound Ras interacts with guanine exchange factors (GEFs), which induce the release of GDP to facilitate GTP binding. Binding of GTP leads to conformational changes in Ras, priming the protein for effectors to bind [9]. In normal and resting cells, Ras-GTP is quickly deactivated by GTPase-activating proteins (GAPs), which accelerate the slow intrinsic GTP hydrolysis by several orders of magnitude. This allows Ras to act as a molecular switch that responds to extracellular stimuli. For example, Ras proteins can become GTP-loaded in response to growth factor stimulation and subsequently recruit its downstream effectors, leading to the activation of signaling cascades involved in diverse cellular processes.

In mammalian cells, three *RAS* genes – *HRAS, NRAS, and KRAS2* – are ubiquitously expressed to give rise to four Ras protein isoforms, H-Ras, N-Ras, K-Ras 4A and K-Ras 4B, with the latter two resulting from alternative splicing of exon 4 in *KRAS2* RNA [10]. Conventionally, the K-Ras 4B isoform is simply referred to as K-Ras. The *RAS* genes are highly conserved across different species, with common functional roles in important signaling pathways that regulate cell growth, proliferation, differentiation and survival, among others [11]. In the animal kingdom, while the different Ras isoforms (such as H-Ras, N-Ras, and K-Ras) are highly homologous in sequence and structure, they are each expressed at varying levels in a tissue-dependent manner, perform overlapping but nonredundant biological functions, and exhibit drastically different mutation frequencies

in human cancers [12]. In pursuit of attacking the activated mutants of the different Ras isoforms for cancer therapy, much insight has been obtained through the search for molecular mechanisms that cause the isoform-specific Ras biology, which will be touched upon in the next few sections.

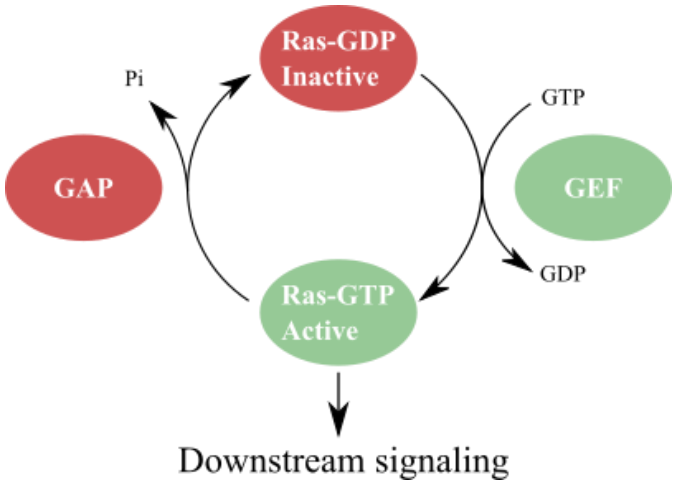

Figure 1.1 Activation cycle of Ras GTPases

1.1.2. Ras protein structure

Ras is approximately 21 kDa in size with 189 (H-Ras, N-Ras and K-Ras 4A) or 188 (K-Ras 4B) amino acids. Ras proteins consist of two domains, a globular (G-) domain of 165/166 amino acids and a C-terminal membrane targeting domain of ~20 amino acids. The G-domain is where nucleotides and effectors bind, which is nearly identical among the Ras isoforms. The C-terminal domain, including the last four residues (CAAX-COOH, where C=Cys, A=aliphatic, and X=any; also known as the CAAX motif), is distinct for each Ras isoform and hence named the hypervariable region (HVR) [13].

Due to the small size of the molecule, structural analysis of Ras has been challenging; it has been particularly difficult to express and crystalize full length Ras.

Therefore, the vast majority of structural studies on Ras were done using only the G-domain.

G-domain

The Ras G-domain is responsible for guanine nucleotide binding and hydrolysis. The domain consists of 6 α-helices and 5 β-sheets interconnected with loops (Fig 1.2A), including a phosphate binding loop (p-loop) and regions for effector interactions known as switch I, II, and III [14]. The phosphate binding loop is the pocket where the nucleotides bind to Ras and is comprised of conserved amino acid residues among the members of the Ras superfamily. This rigid region is important for nucleotide binding and GTP hydrolysis [14]. Nucleotide binding is made by the interaction of the nucleotide base with the N/TKXD motif [where X is any amino acid] and of the β, γ-phosphates with the conserved P loop, the GXXXXGKS/T motif [15]. The residue T35 (G2 box) and the DXXGQ/H/T motif (G3 box) make contacts with the phosphates and Mg^{2+}, which is required for nucleotide binding and GTP hydrolysis. The motifs N/TKXD (G4 box) and SAK (G5 box) contribute as contacts with nucleotide base [15,16].

Major conformational rearrangement of the G-domain occurs at Switch I (residues 32-38) and Switch II (residues 59-67) during the recycling of Ras between active (loaded) and inactive (resting) states [17,18]. The mechanism of this conformational change is described as the loaded-spring model (Fig 1.2B). In the GTP-bound state, Switch I and II are bound to the γ-phosphate via residues Thr35 and Gly60. This keeps the conformation as a 'loaded spring'. GTP hydrolysis leads to the release of the γ-phosphate, and this loss of mass causes the relaxation of switch motifs into a GDP-bound conformation [15].

Hypervariable Region of Ras

The C-terminal HVR of Ras encodes signals required for Ras targeting to the membrane. The HVRs of all Ras isoforms undergo post-translational lipid modifications [19], with the CAAX motif at the C-terminus considered the 'first signal' and residues upstream of the CAAX motif the 'second signal' for plasma membrane targeting (Fig 1.2C) [20,21].

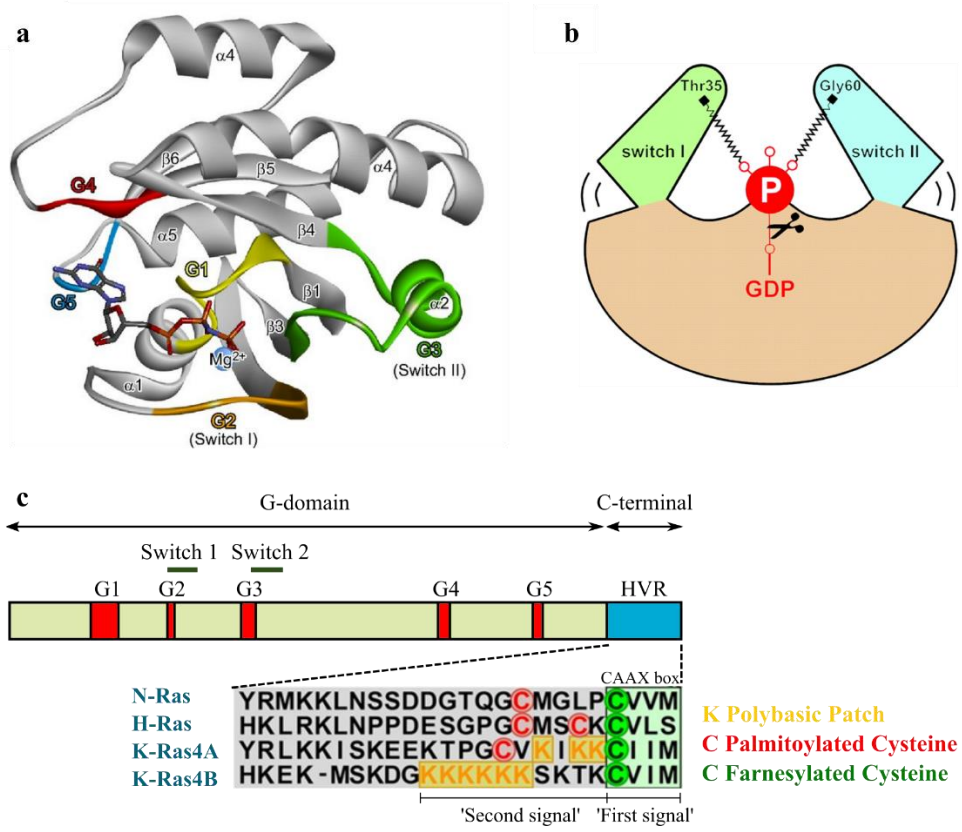

Figure 1.2 Structure of Ras protein. (a) Ras protein structure illustrated by the structure of H-Ras in complex with GTP [22]. (b) Schematic diagram of the universal switch mechanism called a loaded spring mechanism [15]. (c) C-terminal membrane targeting domains of Ras isoforms [23].

After synthesis in the cytoplasm, Ras is first modified at the CAAX motif by three enzymes that work sequentially: farnesyltransferase (FTase), Ras-converting enzyme 1 (RCE1) and isoprenylcysteine carboxylmethyltransferase (ICMT). First, a farnesyl moiety is attached to the cysteine by a thioether bond catalyzed by the FTase. Then the AAX piece

is cleaved by RCE1 at the endoplasmic reticulum (ER). This renders the farnesylcysteine the new carboxyl terminus, which is then further methylated (-OMe) by ICMT. Through these modifications, the C-terminus of Ras proteins are converted from a hydrophilic domain to a lipidated hydrophobic domain in which the charge of the C-terminal carboxylate is negated by methylation [20].

The 'second signal' for membrane targeting of Ras, which is immediately upstream of the CAAX motif, contains different membrane targeting information for each Ras isoform. H-Ras is dual-palmitoylated on residues Cys181 and Cys184. N-Ras and K-Ras 4A are mono-palmitoylated on residue Cys181 and Cys180, respectively. K-Ras 4B, however, is not palmitoylated at all. The secondary signal is provided through a hexalysine polybasic region which interacts with negatively charged head groups of membrane phospholipids to yield a tight binding between K-Ras and the membrane [20].

1.1.3. Ras signaling pathways

The Ras signaling pathways are typically downstream of membrane receptors, including the canonical receptor tyrosine kinases (RTKs) that respond to growth factors (Fig 1.3). Phosphorylation and activation of RTKs lead to formation of receptor complexes that comprise adaptor proteins such as SH2-containing protein (SHC), growth factor receptor-bound protein 2 (GRB2) and GRB2-associated binding proteins (Gab). These proteins recruit SHP2 and son of sevenless homolog 1 (SOS1); the latter catalyzes nucleotide exchange of Ras to yield elevated levels of Ras-GTP [20,24]. Activated Ras initiates downstream signaling cascades via binding to its effectors, usually mediated through the Ras binding domain (RBD). There are at least 10 distinct Ras-regulated signaling pathways involved in various cellular processes.

One of the best characterized Ras effector pathways is the Ras-Raf-extracellular signal-regulated kinases (ERK), also known as the mitogen-activated protein kinases (MAPK) pathway [25]. Active Ras-GTP recruits Raf kinases (A-RAF, B-RAF and C-RAF) to the cell membrane and releases them from sequestration by 14-3-3 proteins and from autoinhibition. Raf is then activated through homo- and heterodimer formation [26], which ultimately leads to ERK activation via another kinase, MEK. Activated ERK then enters the cell nucleus and activates many transcription factors to induce gene transcription programs that promote cell survival, division and motility [27]. This signaling cascade is terminated by GAPs, which promote hydrolysis of GTP to GDP at the Ras G-domain. Deregulated Ras-MAPK signaling is frequently implicated in cancer as, for example, a result of abnormal activation of RTKs or activating mutations in the *RAS* or *RAF* genes. These targets are therefore highly pursued for cancer treatment [26].

Another major Ras effector pathway is PI3K-Akt-mTOR, which is also typically initiated by activated RTKs. Class I_A PI3K is a subgroup of the PI3K family. The regulatory subunit of I_A, p85, attaches to phosphotyrosine residues or other adaptors found on the RTKs. I_A will then convert phosphatidylinositol 4,5-bisphosphate (PIP2) to phosphatidylinositol 3,4,5-trisphosphate (PIP3). Once PIP3 is formed, it recruits PDK1 and Akt kinases and brings them in close proximity. PDK1 phosphorylates Akt and consequently, Akt is activated and regulates many cellular processes, including cell survival, proliferation, and growth [28–30].

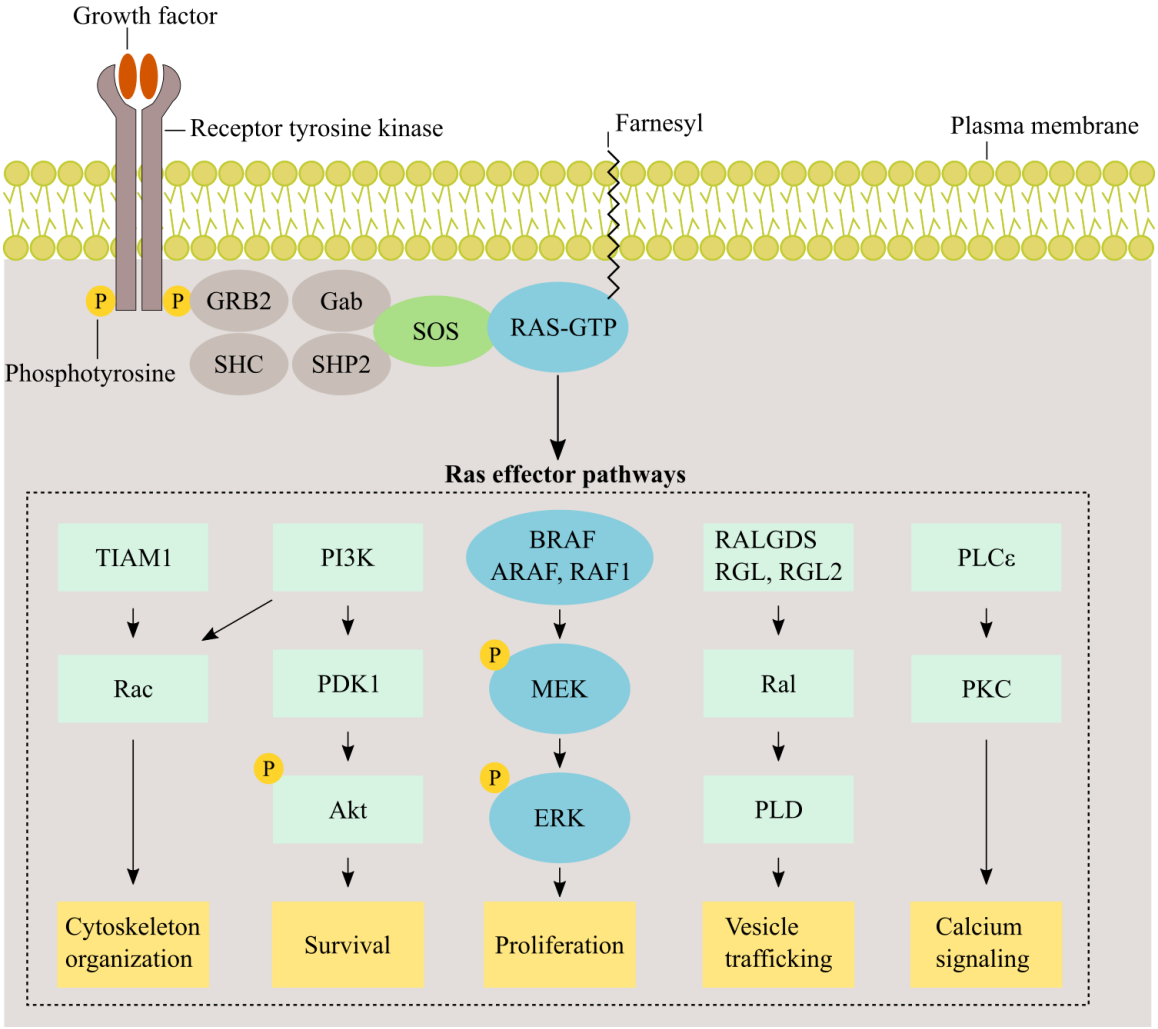

Figure 1.3 Ras signaling cascades

Ras can also activate RALGDS, a GEF for the Ral GTPase [31]. Ral GEFs including RALGDS, RALGDS-like gene (RGL) and RGL2 are able to activate Ral, which in turn stimulates phospholipase D (PLD). The Ral GEFs have been documented in the late 1990s as the third class of Ras-GTPase effectors, which were later established as key components in Ras-dependent tumorigenesis *in vivo* [32].

Other Ras activated signaling molecules include the tumor invasion and metastasis inducing protein 1 (TIAM1), Rac, phospholipase Cε and protein kinase C. Rac is important

for actin reorganization [33]. Phospholipase Cε directly binds to Ras–GTP to become activated, and its activation leads to hydrolysis of PIP_3 to diacylglycerol and inositol-1,4,5-triphosphate, where both products serve as second messengers to cause intracellular release of calcium and activation of protein kinase C, respectively [34].

1.1.4. Raf kinases

Ras signaling requires binding to effectors, which are defined as proteins with strong affinity to Ras-GTP. Effectors of Ras have been studied extensively, in part through the searches for strategies to interfere with aberrant Ras signaling in human cancers. To date, more than 10 Ras effectors have been identified; these include RalGDS, PI3K, p120GAP, Raf and TIAM [35], some of which were discussed earlier. Below we discuss in detail a major class of Ras effectors, the Raf kinases.

The Raf (Rapidly Accelerated Fibrosarcoma) kinases were first identified in the early 1980s, also as retroviral oncogenes. Three Raf isoforms, namely A-, B- and C-Raf were subsequently discovered as Ras effectors and upstream activators of the MAPK kinases [36]. Raf proteins are 55-57 kDa in size and all Raf isoforms have three conserved regions (CR1, 2 and 3). CR1 contains a Ras binding domain (RBD) and a cysteine-rich domain (CRD), which are essential for binding to Ras-GTP and additional membrane interactions, respectively. CR2 contains inhibitory phosphorylation sites required for negative regulation of Ras binding and Raf activation [37]. CR3 contains the activation segment and the kinase domain [38]. Functionally, Raf proteins can be divided into the N-terminal regulatory domain and the C-terminal kinase domain. Under resting conditions, Raf resides in the cytoplasm with the regulatory domain restraining its kinase activity. This auto-

inhibitory state is stabilized by binding of 14-3-3 dimers to phosphorylated S259 and S621 located in the regulatory and C-terminal domains [37].

Activation of Raf begins with recruitment to the plasma membrane by Ras-GTP. Raf RBD and CRD are essential for this step. The RBD of Raf interacts with effector loops of Ras-GTP, while CRD contacts the C-terminal farnesyl moiety of Ras and the membrane. For the importance of the RBD to Ras-MAPK signal transmission, mutation in a single amino acid (Arg89) disrupts binding of C-Raf to Ras and abolishes membrane recruitment and activation of Raf [39]. CRD interacts with membrane phospholipids including phosphatidylserine (PS), which seems to be also required for Raf membrane recruitment [40]. Binding of Raf to Ras promotes dephosphorylation of S259, which leads to the release of 14-3-3 from the N-terminus to promote membrane anchoring of Raf. Thus, both RBD and CRD interacts with Ras and are essential for Raf membrane recruitment [37].

Recently it has been realized that Raf also needs to be dimerized for MAPK activation in multiple cellular contexts [41,42]. Raf isoforms form homo- or heterodimers with different potencies in promoting MAPK signaling, among which the C-Raf/B-Raf heterodimer is the strongest MAPK activator [42]. Among the three isoforms, B-Raf is the most frequently mutated, and mutations in A- or C-Raf are rare. More than 30 different mutations of the *BRAF* gene were identified in human cancers, the majority of which are located within the kinase domain. B-Raf mutants promote MAPK signaling by activating endogenous C-Raf via an allosteric or transphosphorylation mechanism [43]. Inhibitors targeting B-Raf, such as vemurafenib, have been developed. A subset of B-Raf inhibitors work by competing for the ATP binding pocket, thereby inhibiting its kinase activity; others work through allosteric mechanisms. Intriguingly, while many Raf kinase inhibitors

potently inhibit growth of tumors bearing activating *BRAF* mutations (e.g. B-Raf V600E, which accounts for >1/2 of melanoma tumors), they paradoxically stimulate growth of cells and tumors with wild type *BRAF* [44]. This was found to be mediated by inhibitor induced Raf dimerization, in the form of either B-/C-Raf heterodimers or C-/C-Raf homodimers. Importantly, kinase inhibitor induced paradoxical activation of Raf is dependent on Ras-GTP. This is either because Ras binding causes exposure of 14-3-3 binding sites in the COOH-terminus of C-Raf [45] or because Ras itself forms dimers [46] or multimers [47], which facilitates Raf dimer formation at the cell membrane.

1.1.5. Ras in cancer

Ras mutations in human cancer

Tumorigenesis is a long process during which somatic mutations in DNA lead to unbalanced proliferation and cell death by disrupting the program regulating the processes. Ras is an essential molecular switch in this program, of which mutations are prevalent in human cancers. Mutations in the Ras family of proto-oncogenes were found in 20% to 30% of all human tumors. Although the three Ras isoforms share almost identical G-domains, incidence rates of activating mutations vary considerably among the isoforms and with tumor type (Table 1.1). Out of all detected Ras mutations, K-Ras is the predominantly mutated isoform (85%), followed by N-Ras (11%) and H-Ras (4%). Data available at the cBioPortal database showed that mutated K-Ras has been found with high occurrence in pancreatic, colon, lung and endometrial carcinoma. N-Ras mutations have been reported in colon cancer, melanoma, bone marrow and thyroid carcinoma. Finally, H-Ras is primarily mutated in melanoma, bladder cancer, thyroid cancer, and adrenal gland carcinoma (Table 1.1).

More than 99% of Ras mutations are substitutions at residues G12, G13 and Q61. Quantitative analysis revealed distinctive codon mutation signature of each isoform. 80% of K-Ras mutations occur at codon 12, with very few mutations observed at codon 61. For N-Ras, 61% of tumors mutated at codon 61, and 35% at codon 12. In the case of H-Ras, it has about equal mutations at codon 12 (50%) and codon 61 (40%) [12]. As discussed previously, Ras activation is regulated by GEFs and GAPs. GEFs promotes Ras binding to GTP for activation, while GAPs inactivate Ras by accelerating GTP hydrolysis. Structural analysis revealed that mutations of G12 or G13 present a steric block that prevents the arginine finger of GAPs from entering the GTP site. Q61 is also part of the GTP hydrolysis mechanism and similarly affected. Therefore, mutations at residues G12, G13 and Q61 make Ras-GTP insensitive to GAP-mediated GTP hydrolysis, such that the cell is no longer able to switch off the transmitted signal [48].

Tissue	KRAS (%)	NRAS (%)	HRAS (%)
Pancreas	91	0	<1
Colon	42	9	0
Lung	33	<1	<1
Skin (melanoma)	2	27	1
Endometrium	21	4	<1
Testicular germ cell	13	5	<1
Bone marrow	4	8	0
Thyroid	1	8	3
Thymus	<1	2	8
Stomach	9	1	<1
Adrenal glands	0	0	10
Bladder	0	1	5
Brain	1	1	0
Cervix	6	<1	<1
Bile duct	6	0	0

Table 1.1 Frequency of Ras mutations in human cancers. Data were compiled from the TCGA datasets present in the cBioPortal database for cancer genomics [49].

Cancer therapies targeting Ras

With some of the mechanisms that regulate Ras activity revealed, extensive efforts were made to develop anti-cancer therapies targeting mutant Ras with both direct and indirect strategies. These strategies include i) disrupting Ras association with the membrane, ii) inhibiting binding of Ras to GTP or effectors and iii) blocking Ras downstream signaling pathways.

Association with the membrane and trafficking to specific cellular locations is essential for the oncogenic activities of Ras, which makes this association a logical target for anti-Ras cancer therapeutics. Phosphodiesterase δ-subunit (PDEδ) is a small molecule that binds to K-Ras and facilitates its trafficking to the plasma membrane. Recently, Zimmermann *et al.* developed a small molecule inhibitor that selectively binds to the prenyl-binding pocket of PDEδ [49] where farnesylated K-Ras interacts, thereby disrupting K-Ras trafficking to the membrane. Disruption of K-Ras and PDEδ interaction reduced K-Ras signaling in cells, but this approach has not been proven effective in vivo. In the early 1990s, farnesyltransferase (FTase), an enzyme responsible for prenylation of the Ras CAAX motif, was targeted as an anti-Ras strategy. Several FTase inhibitors including lonafarnib and tipifarnib exhibited highly specific inhibition of FTase in cells and proceeded to clinical trials. The outcome, however, was disappointing, which was a major setback for targeted cancer therapy. It turns out that Ras proteins are still able to associate with the plasma membrane through alternative post-translational modification mechanisms such as geranylgeranylation [23].

A more direct strategy is to inhibit GTP binding of Ras or to prevent it from interacting with its effectors. Ostrem *et al.* reported an inhibitor targeting Ras mutant G12C which is present in a substantial proportion of lung tumors. This inhibitor containing a thiol (SH) group will bind to the side chain of cysteine residues by forming a disulphide (S-S) bond [50]. Structural analysis indicated that K-Ras G12C binding to the inhibitor increases the relative affinity of K-Ras G12C for GDP over GTP, leading to trapping of inactive K-Ras. However, this compound targets only K-Ras G12C. It did not affect cells expressing other, more common K-Ras mutations such as G12V or G12D [50]. Other small molecule

inhibitors blocking Ras interaction with SOS1 [51] or Ras effectors [52] were also identified, but it is still unclear whether further optimization will improve the affinity enough to develop compounds that are clinically effective.

An alternative approach to inhibit Ras is to block its downstream signaling pathways. MAPK and PI3K are the most prominent pathways of Ras that are often deregulated in cancer. Inhibitors targeting either pathway alone, however, has only been effective in the short term against Ras-driven cell lines. Negative feedback and reflexive activation of other Ras or RTK pathways were commonly observed, and tumor cells eventually gained resistance [53]. In the case of blocking the MAPK pathway, approaches have been focused on developing Raf or MEK inhibitors. Sorafenib is the first Raf inhibitor tested in clinical trials and was approved by the U.S. Food and Drug Administration (FDA) in December 2005 for the treatment of advanced renal cancer. It showed inhibiting capacity not only against Raf but also against several other receptor tyrosine kinases such as VEGFR, PDGFR and FGFR-1. Sorafenib disables the B-Raf kinase domain by trapping the enzyme in its inactive form and blocks the ATP binding pocket via high-affinity binding [43]. However, sorafenib is much lesss effective for V600E mutant B-Raf than wild type B-Raf, which led to the second generation of Raf inhibitor, vemurafenib (compound PLX4032). Vemurafenib potently suppressed Raf-MEK-ERK signaling and showed improved clinical benefit in BRAF V600E melanoma, but it unexpectedly activated MAPK in *BRAF*-wild type cells, as discussed earlier. This paradoxical effect led to growth of hyper-proliferative skin lesions and squamous-cell carcinomas in some patients [54].

Small-molecule compounds that selectively inhibit MEK have also been developed. Early trials with those inhibitors demonstrated tumor growth inhibition, but their

effectiveness was mostly limited by toxicity. Side effects including skin rash and visual disturbances were observed with MEK inhibitors [55]. Later, several compounds with improved pharmaceutical properties were developed. One of those compounds, trametinib, became the first MEK inhibitor approved by FDA in May 2013 for the treatment of patients with metastatic melanoma. A Phase III clinical trial demonstrated benefits for metastatic melanoma carrying B-Raf V600E mutations, but the resistance to single agent trametinib often occurs within 6-7 months. To overcome this, in a Phase III trial, trametinib was combined with a Raf inhibitor, dabrafenib, and the combination showed better efficacy than the single agents alone and was approved by the FDA in 2014 for the treatment of patients with *BRAF*-V600E/K melanoma [55].

In summary, efforts to date to inhibit mutant Ras activity in human cancer have met limited success, which urged the search for new mechanisms regulating Ras activities and development of novel therapeutic approaches to target mutant Ras.

1.2. Spatial mechanisms regulate Ras signaling at the membrane

1.2.1. Membrane heterogeneity

Membrane rafts

The cell membrane surrounds the cytoplasm of a cell, separating the intracellular components from the extracellular environment. Biological membranes typically consist of a lipid bilayer with embedded proteins and is selectively permeable to ions and organic molecules, which helps the membrane to protect the integrity of the cell interior [56]. The model of cell membrane structure was proposed as a *fluid mosaic model* by Singer and

Nicolson in 1972 [57]. In this model, the plasma membrane was described as a mosaic of phospholipids, cholesterol, protein and carbohydrates. The *fluid mosaic model* is a major advance in understanding the membrane structure and function. However, it has now become clear that simply picturing the membrane as a lipid sea where all molecules float freely is not enough to explain how the cell membrane functions.

The presence of distinct membrane sub-compartments was observed by Yu *et al*. using nonionic detergents to separate the membrane into detergent-labile and detergent-resistant fractions [58–63]. A number of follow-up studies using biochemical and biophysical tools suggested that the cell membrane is laterally heterogeneous [64]. Lipid rafts were then defined as liquid ordered (L_o) domains enriched in cholesterol and sphingolipids. The initial concept of lipid rafts, however, was controversial in part due to the lack of tools for direct observation of these domains. The biochemical methods used in the early studies, including cholesterol depletion [59] and detergent resistant membrane isolation [65], were considered too harsh to authentically preserve or reflect the compositions of physiological membranes or membrane domains. Lipid rafts were also considered small structures, sub-micrometer to nanometer scale, highly dynamic, and lacking a distinct morphology, thus posing a serious challenge to any existing techniques during the infancy of membrane domain research.

More recently, the concept of lipid rafts has been influenced by development of imaging techniques such as super-resolution fluorescent microscopy (SRM), single particle tracking (SPT) and Förster resonance energy transfer (FRET). These techniques allow visualization of protein-protein interaction and their behavior on the cell membrane in real time at nanometer scale. The term ‘lipid rafts’ is applied to many distinct types of

membrane assemblies [66]. It is defined as transient, relatively ordered membrane domains, which are enriched in saturated phospholipids, glycolipids, cholesterol, lipidated proteins and glycosylphosphatidylinositol (GPI) - anchored proteins (Fig 1.4). The formation of such membrane domains is essential for the recruitment and interaction of certain proteins and lipids [67–69]. The asymmetric property of the cell membrane and lipids distributed in the inner and outer leaflet of the membrane further affect the membrane heterogeneity. Increase of lipid packaging and order leads to decreased fluidity of the domain, further affecting diffusion of certain membrane molecules. It has been shown that the lipid domains serve as functional platforms for various cellular processes including signal transduction and virus entry [70,71].

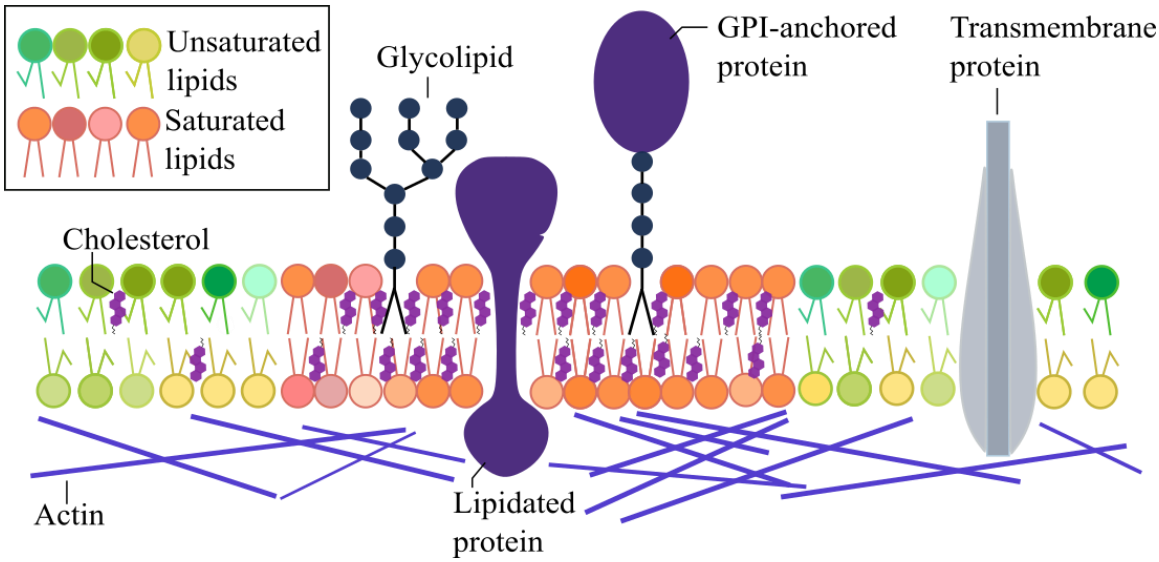

Figure 1.4 Lateral heterogeneity in the plasma membrane

Picket-fence model (Cortical actin cytoskeleton)

The cortical actin cytoskeleton, which consists of elaborate and complicated filament networks, is directly situated on the cytoplasmic surface of the plasma membrane. The picket-fence model suggests that the mobility of membrane-bound molecules is hindered by actin-based membrane-skeleton 'fences' and anchored transmembrane protein 'pickets' (Fig 1.5). This model was proposed based on single particle tracking of membrane molecules in living cells [71]. For example, a G-protein coupled receptor, μ-opioid receptor (μOR), was observed undergoing short-term (~45 ms on average) confined diffusion within the membrane compartments (~210 nm on average) and long-term hop diffusion over these compartments [72]. This observation suggests that the diffusion of proteins are confined within individual corral and proteins are occasionally able to escape into an adjacent corrals due to the motion of cortical filaments. This result is consistent with a recent report that resolved the cortical actin using super-resolution fluorescence imaging while simultaneously tracking individual membrane proteins in live mammalian cells [53]. They found that cortical actin transiently confines Kv channels and the molecules are able to hop between compartments.

The cortical actin cytoskeleton as an integrated component of the plasma membrane is different from bulk actin cytoskeleton both structurally and functionally. It interacts dynamically with membrane molecules and regulates their anchoring to membrane compartments. The effectiveness of a membrane molecule hopping between corrals is dependent on the size of its cytoplasmic domain and on its association with other membrane proteins [73]. A protein with a larger cytoplasmic domain will make it harder to hop across corrals. If a protein binds to other membrane molecules, the larger protein complex will also make it more difficult to escape from corrals. It has been suggested that

the confinement created by the cortical cytoskeleton assists receptor signaling processes by increasing the concentration of activated receptors [12,74,75].

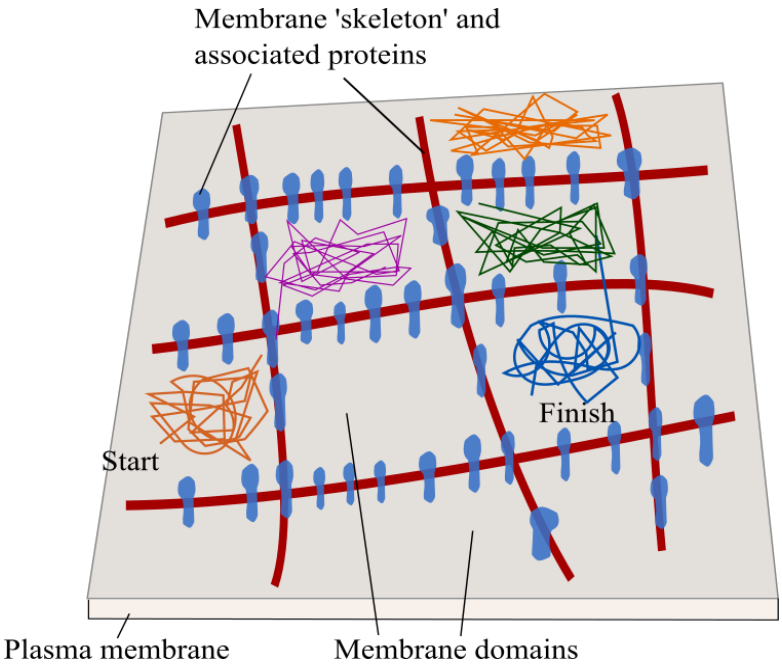

Figure 1.5 Corralling of membrane proteins by cortical cytoskeletal filaments [71].

1.2.2. Spatial organization of Ras on the membrane

Nanoclustering of Ras at the membrane

Recently it has been realized that many membrane proteins are clustered at the cell membrane at the nanoscale. There is clear evidence for membrane proteins such as glycosylphosphatidyl (GPI)-anchored proteins and immune receptors organizing into nanoclusters [76]. This nanoclustering activity of Ras has also been directly observed with quantitative imaging with immuno electron microscopy (immuno-EM) [74] and super-resolution microscopy (SRM) [46], and it is supported by other measurements such as single molecule tracking (SMT) [77], fluorescence resonance energy transfer (FRET) [77], and fluorescence recovery after photobleaching (FRAP) [78]. A highly dynamic spatial

organization of Ras proteins at the cell membrane has been revealed. Early investigations by Plowman *et al*. and Prior *et al.* used antibody-gold nanoparticles to label GFP-Ras on prepared membrane sheets. This approach involves overexpression of GFP-Ras to compensate for the low labeling efficiency of antibody-gold nanoparticle conjugates. Individual Ras molecules tagged with a gold nanoparticle were directly visualized under electron microscopy and thus a distribution map was achieved. With this technique, about 40% of Ras proteins were estimated to form nanoclusters at the cell membrane with the remaining molecules as monomers [75]. The size of Ras nanoclusters are about 20 nm in diameter, and each nanocluster contains 5-8 Ras molecules. Judging from the durations of Ras molecules in immobile states in live cell SPT experiments, the lifetime of the Ras nanoclusters was likely short, typically around 0.1-1 second [77]; if this were true, the Ras nanoclusters should be considered highly dynamic entities constantly assembling and disassembling. Interestingly, C-terminal HVR of Ras exhibited similar clustering properties and membrane localization as full length Ras, which will be further investigated in Chapter 3.

Moreover, Ras nanoclusters have been hypothesized as an essential platform for Ras signaling based on immuno-EM data showing Raf recruited to Ras nanostructures [79]. Experimental and computational analyses by Tian *et al.* observed that signal transduction to activate ERK is completely dependent on Ras spatial organization and that it fails if nanoclustering is abrogated [79]. Nanoclusters also establish an analog-digital-analog circuit, enabling a high precision signal transmission across the cell membrane [80]. Tian *et al.* also showed that epidermal growth factor (EGF) stimulates Ras-GTP loading and

leads to nanocluster formation, and that the number of resulting Ras nanoclusters is proportional to EGF concentration [80].

Dependency of Ras nanoclustering on membrane nanodomains

The connection between Ras and the plasma membrane is mediated via the Ras HVR. As described earlier, different Ras isoforms undergo different post-translational modifications on their HVR. For example, K-Ras is tethered to the membrane by a farnesyl group and a polybasic region, whereas H-Ras is anchored by two palmitoyl chains and a farnesyl group. Therefore Ras isoforms possess distinct interactions with the cell membrane. Mechanisms regulating these interactions are complicated by their dependency on the HVR structure of Ras isoforms, the organization of Ras nanoclusters and the heterogeneous compositions of the cell membrane, which is just beginning to be understood.

Cholesterol is a basic component of the cell membrane, and early studies demonstrated the preference of tH (H-Ras HVR) and H-Ras-GDP to cholesterol enriched membrane domains (Fig 1.6) [47,78]. Upon activation, H-Ras is loaded with GTP and segregates into cholesterol independent nanoclusters. In contrast, K-Ras was shown to localize to cholesterol independent nanodomains regardless of its activation states. In the case of N-Ras, nanoclusters of tN (N-Ras HVR) and N-Ras-GDP appear to be cholesterol independent, and nanoclusters of N-Ras-GTP are cholesterol dependent [47].

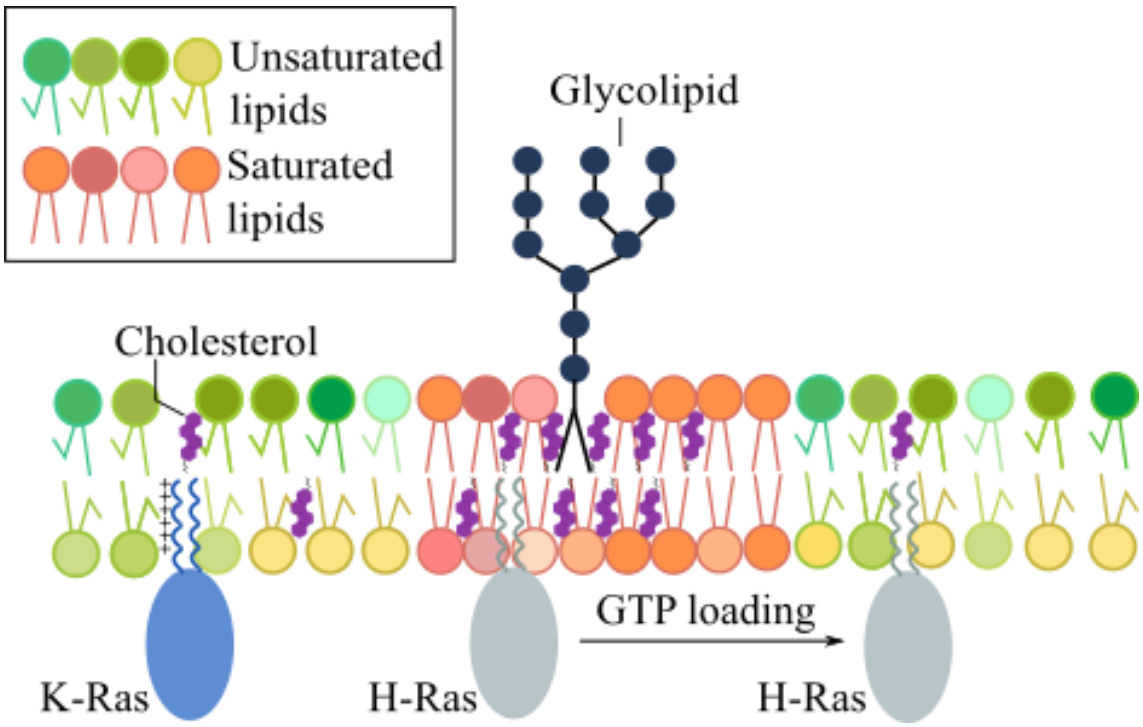

Figure 1.6 Ras isoforms segregate into distinct membrane compartments [81]**.**

Recent studies have also shown that Ras nanoclusters interact with membrane anionic lipids. Phosphatidylserine (PS) is a common membrane constituent that interacts with all Ras nanoclusters, but is only an obligate component for organization of K-Ras nanoclusters. Redistribution of phosphatidylserine by membrane depolarizations disrupts nanoclustering of K-Ras and inhibits MAPK signaling. This dependency of K-Ras nanoclusters, but not H-Ras or N-Ras nanoclusters, on membrane phosphatidylserine can be explained by the electrostatic interactions between anionic PS and positively charged K-Ras HVRs [82].

The advancement of imaging techniques, together with biochemistry methods, revealed the interplay between Ras function and its spatial localization. Based on recent data, it has now been clear that aside from the biochemical mechanism using the GTP/GDP switch, Ras signaling is also regulated via nanoscopic spatial organization. To better

understand how Ras functions in a cell, it is therefore imperative to understand how the membrane is organized.

Ras dimerization

Because Raf activation by Ras is known to involve Raf dimerization yet Raf binds to Ras as a monomer, it has been proposed that Ras may act as a dimer [49]. The existence of Ras dimers, however, has been observed in only a few studies [46,83,84] and remains controversial. In 2012, Güldenhaupt *et al*. demonstrated dimerization of full length N-Ras on an artificial POPC membrane [83]. In their study, orientation of N-Ras attached to POPC bilayers was probed via attenuated total reflectance Fourier transform infrared (ATR-FTIR). They found that the stable orientation of N-Ras has a tilt angle of 23°. Simulations of Ras orientation on the membrane indicated that this unusual tilt angle likely resulted from Ras dimers. It was proposed that the dimerization interface is established through the helix α4, helix α5 and β2-β3-loop [83]. Later in 2014, another study showed H-Ras dimers when tethered to artificial membranes [84], which was subsequently found to be an artifact due to photo oxidation [85].

The existence of K-Ras dimers in live cells was also observed by Nan *et al.* [46] using quantitative SRM. In this study, each K-Ras was tagged with PAmCherry1, a photoactivable fluorescent protein. Cells expressing this construct were imaged through photoactivated localization microscopy (PALM) that allows single molecule counting. Using this technique, the presence of Ras dimers in live cells was visualized. This work also showed activation of the MAPK pathway at minimal Ras expression levels that resulted in dimers. They also observed that forced Ras dimerization results in activation of the pathway [46].

More recently, Spencer-Smith *et al.* developed a synthetic binding protein (monobody) with high affinity to both GTP- and GDP-bound states of H-Ras and K-Ras [86]. This monobody binds to the α4-β6-α5 region of Ras and disrupts Ras dimerization and nanoclustering. As a result of this, formation B-Raf/C-Raf heterodimerization and activation of downstream signals were blocked [86].

While the pharmacological inhibition of Ras in human cancer has been challenging over decades, the Ras dimer has become a new potential therapeutic target [87]. The importance of helices 4 and 5 as a potential dimer interface have been exploited in two recent studies [83,86]. The possibility that Ras may function as dimers adds both exciting new insights and complexity into how Ras signaling may be regulated in cells. At present, it is unclear how Ras dimers and nanoclusters are related to each other. For simplicity, we collectively call these structures Ras multimers in the remainder of this thesis.

1.3. Tools for studying membrane domains and spatial regulation

1.3.1. Previous tools for studying membrane domains

Detergent-resistant Membranes

Initial evidence for the lateral heterogeneity of the cell membrane was based on the observation of detergent-resistant membranes (DRMs). This method utilizes the relative insolubility of Lo membrane fractions in cold, non-ionic detergents to help separate Lo membranes from whole cells or membranes [64]. Membrane proteins including sphingolipids and GPI-anchored proteins were found in fractions insoluble in Triton X-100 at 4 °C, floating to a characteristic density after density gradient centrifugation [62]. DRM

isolation was then widely adopted as the method to characterize protein compositions of lipid rafts. However, it is now clear that DRMs are not equal to lipid rafts. Treatment with strong detergents does not confer convincing characterization of native membrane composition and lipid raft organization in cells. Moreover, the results were heavily influenced by experimental variations such as the choice of detergent, detergent concentration, and temperature. Subtle changes in these conditions could yield different results, accounting at least in part for the contradictory reports on lipid raft composition [64]. Therefore, although DRM was instrumental to initial understanding of membrane heterogeneity and lipid rafts, additional methods are required to validate and in some cases, rectify the observations.

Artificial Model Membranes

Along with DRMs, artificial model membrane systems were also developed to investigate the biophysical and chemical origins of lipid rafts. Two artificial membrane systems, namely supported lipid bilayers [88] and giant unilamellar vesicles (GUVs) [89], have been widely used for such purposes. These membrane systems are relatively robust to prepare in the lab, enabling high-resolution imaging of synthetically attached or natively inserted membrane proteins and lipids. These model systems also permit modifications to their biochemical composition and physical properties such as fluidity, curvature and rigidity. Using proper chemical compositions, phase segregation between lipid species were readily demonstrated. In general, two distinct liquid phases were defined: a highly packed, ordered phase enriched in saturated lipids and cholesterol (liquid ordered, L_o), and a relatively more fluid, disordered phase mainly comprising unsaturated lipids (liquid disordered L_d) [89]. Because the L_o phase is tightly packed and enriched in cholesterol, it

has been considered to represent lipid rafts. Physical properties and dynamics of L_o have been analyzed through conventional microscopy and fluorescence correlation spectroscopy [90]. However, there are still some major gaps between the model membranes and lipid rafts in biological membranes. Given the highly complex composition and structure of biological membranes, one of the biggest concerns is whether findings obtained from artificial model membranes faithfully reflect those from the living system. For example, most of the experiments were performed in a liquid-only system and failed to generate high protein/lipid ratio, which is in contrast to biological membranes [64]. Although more natural systems such as cell-derived giant plasma membrane vesicles (GPMVs) [91] have been developed, other important cellular structures such as the cortical cytoskeleton and extracellular matrix are still missing in this model. Therefore, while model membranes were useful for recapitulating specific aspects of membrane organization and dynamics, much of the biology related to membrane domains (including lipid rafts) may only be learned by studying actual biological membranes.

Electron Microscopy

For the foreseeable difficulties in purifying the numerous, heterogeneous membrane domains from cells, various high-resolution imaging techniques capable of 'in situ' analysis of membrane ultrastructures have come to the rescue. Among these, electron microscopy (EM) offers the best spatial details and has been one of the most commonly used tools. Many specialized membrane structures such as clathrin coated pits, caveolae, or cortical cytoskeleton have distinct morphologies or high EM contrast, and they have been readily characterized with EM in nanometer resolutions [92,93]. As most cells are too thick for EM, membrane sheets peeled off from intact cells or thin sections from resin-

embedded samples are routinely used to expose the membrane. For mapping the spatial distribution of certain proteins or lipids, conjugation of antibody and gold nanoparticles (immuno-gold) are commonly used as label agents. A distribution pattern of gold nanoparticles is obtained through EM and then analyzed statistically to determine their association.

This approach, widely known as immuno-EM, was used by Prior *et al.* to investigate Ras nanoclustering on the membrane in 2002 [75]. This method enabled direct visualization of Ras localization on the membrane with nanometer spatial resolution, a new precedent in Ras research. In the following decade, a series of studies by the Hancock lab used this method to further investigate the nanoclustering of multiple Ras isoforms [47,82,94]. However, the limitations of this method are also obvious: no dynamic information of lipid raft and low labeling efficiency with immuno-gold. To overcome this labeling issue, Ras proteins had to be highly overexpressed [75], which may affect Ras nanocluster formation. The number of molecular species to be imaged at once was also limited to ~2 due to this labeling scheme.

Fluorescence Microscopy

Fluorescence microscopy (FM) is a versatile imaging tool that has been widely used in biomedical research for decades. Its pros and cons are somewhat opposite to those of the EM: high labeling efficiency, live cell compatibility, multi-color capability, but diffraction-limited resolution. Through special imaging schemes, however, the limitation in resolution could be circumvented and information at the nanoscale could be retrieved using conventional FM. In this section, we will discuss two of such schemes, single molecule

tracking (SMT) and Förster resonance energy transfer (FRET), both of which have been used to study the dynamics and/or interactions of membrane molecules [77].

SMT involves tagging proteins of interest with either an organic dye or a fluorescent protein and continuously observing the motion of individual molecules in living cells. The trajectories of individual molecules are then measured to determine their types of motion. For membrane-bound molecules, different motion types such as directed motion, confined motion or anomalous diffusion, and free diffusion have all been observed [95]. FRET utilizes the energy transfer between two spectrally overlapped fluorescent molecules, one emitting at a shorter wavelength and designated the donor and the other the acceptor, when they are within a few nanometers. Since FRET efficiency is very sensitive to the distance between the donor and the acceptor, it has been used to measure small changes in distance for example in the case of protein-protein interactions. Work by Murakoshi *et al.* combined SMT and FRET to observe Ras diffusion and interaction with effectors on the membrane at the single molecule level [77]. In their experimental design, Ras and GTP were tagged with yellow fluorescent protein (YFP, donor) and BodipyTR (acceptor), respectively. Trajectories of YFP molecules, representing inactive Ras-GDP, were first recorded. After EGF stimulation, BodipyTR-GTP binding to YFP-Ras generated FRET signal due to the proximity between BodipyTR and YFP. Using this approach, Murakoshi *et al.* demonstrated that Ras exhibits transient immobile states when activated [77].

Atomic Force Microscopy

Atomic force microscopy (AFM) has been a traditional method for material science and has not been widely used for biological specimens until recent years. In a typical AFM

setup, a cantilever with a sharp tip is used to scan over a sample surface. When the tip is brought into proximity of a sample surface, forces between the tip and the sample surface lead to a deflection of the cantilever [96]. The deflection is detected by reflecting an incident laser beam off the cantilever onto a position-sensitive photo diode (PSPD).

A nice example for applying AFM to probe the cytoplasmic surface of the membrane was illustrated by Usukura *et al.* [97]. In their paper, the upper cell membrane was removed by a custom-made sonicator. This 'unroofing' method allowed the accessibility of AFM tips to the cytoplasmic surface. Visualization of membrane structures including cortical actin filaments, clathrin coats, and caveolae was achieved at nanometer resolution comparable to EM. Short periodicity on actin filaments and the terminal domain of clathrin molecules were resolved. The biggest advantage of AFM is that the imaging can take place in a liquid environment without dehydration and drying, which are always concerns for causing artifacts during EM sample preparation. In addition to resolving ultastructures, AFM is also able to measure forces such as cell-adhesion forces. As a novel imaging technique in cell biology, AFM is expected to provide new perspectives to explore cellular dynamics.

1.3.2. Correlative super-resolution and electron microscopy

Super-resolution microscopy

Super-resolution microscopy (SRM) refers to a class of light microscopy techniques that overcome the diffraction limited resolution of conventional light microcopy. Based on their principles, current SRM can be categorized into three types: stimulated emission depletion (STED) [98], structured illumination microscopy (SIM) [99,100], and single-molecule localization microscopy (SMLM) [101,102]. In this thesis, we will focus on

SMLM, which again has three main variations: Photoactivated localization microscopy (PALM) [102], stochastic optical reconstruction microscopy (STORM) [101], and DNA-PAINT [103]. These SMLM variations are all based on the same two concepts, 1) nanometer localization of single point emitters, and 2) stochastic switching of densely packed emitters to achieve single-emitter localization (Fig 1.7).

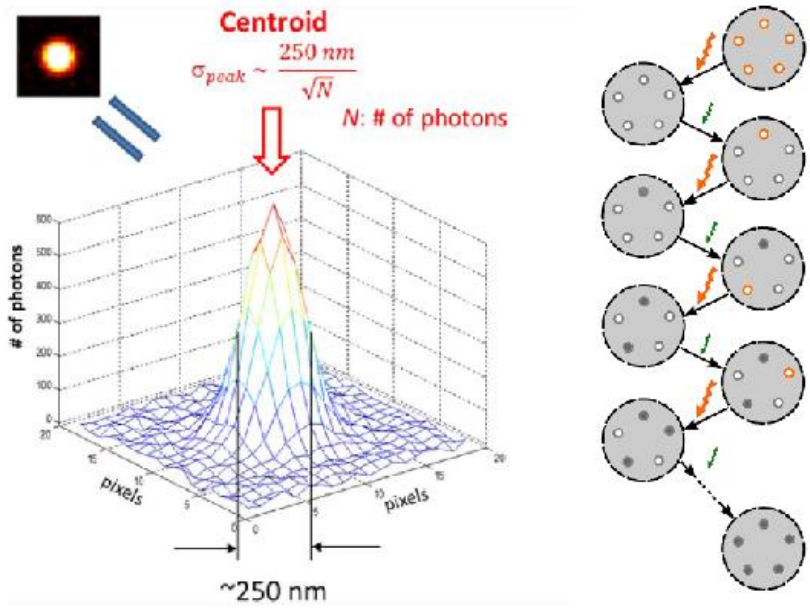

Figure 1.7 Principles of single-molecule localization microscopy (SMLM)

The resolution of conventional light microscopy is limited by the fact that each single fluorophore (a point emitter) appears much larger in the far field due to the diffraction of light. The image of each fluorophore will be a spot with a finite size (~250 nm at least). However, the intensity profile of this spot, also known as the point spread function (PSF), describes the probability density of photons falling within a certain distance from the 'true' position of the emitter (centroid) with standard deviation σ. Therefore, the centroid localization of a single fluorophore can be calculated by averaging N measurements of the

same PSF, with the localization precision given by $\sigma = \Delta/\sqrt{N}$; here Δ is the size of the PSF [104]. That is to say, if 1000 photons can be collected, the localization of a single fluorophore achieved can be as precise as ~13 nm.

Nanometer localization requires isolated PSFs, but biological samples are almost always densely labeled for typical targets. Therefore, the second concept of SMLM is to temporally isolate spatially overlapping emitters. One idea was to use switchable fluorophores that can be turned 'on' stochastically, for example by illuminating with violet light or through other means. In one switching cycle, only a small fraction of fluorophores is turned 'on' to emit fluorescence, and the emitters are sufficiently sparse for each emitter to be detected and localized unambiguously. Their PSFs are recorded before the emitters are turned 'off', either due to photobleaching or transient residence in a nonfluorescent state. By repeating this cycle thousands of times, isolated PSFs of most fluorophores are recorded to allow their precise centroid locations to be calculated. A final, super-resolved image can then be reconstructed by putting all the localization coordinates together [102].

As a major breakthrough in biological imaging, SMLM allows various biological applications such structural analysis [105], single-molecule counting [46] and high-throughput single molecule tracking [106]. For example, with quantitative PALM, Nan *et al.* were able to directly visualize K-Ras-GTP dimers and multimers in cells. PALM imaging of PAmCherry1 tagged K-Ras allows localization of Ras molecules at nanometer resolution while expressed at a physiological level [46].

Correlative super-resolution and electron microscopy

Correlative light and electron microscopy (CLEM) combines fluorescence microscopy (FM) with electron microscopy to leverage the advantages of both modalities.

Fluorescent labels attached to specific species can be visualized with FM to determine the distribution of the species within a cell, and a corresponding EM image can provide a detailed view of the cellular ultrastructure, which assigns a biological context to the targets imaged with FM. An outstanding problem with CLEM is the large resolution gap between the two modalities. While EM offers an impressive resolution on the Angstrom scale, diffraction-limited FM only provides ~200 nm resolution. Thus, the spatial distributions revealed through FM can only be coarsely related to the ultrastructures revealed through EM. To bridge this resolution gap, recent work has attempted to combine SRM with EM, because the resolution afforded by SRM is much closer to that of EM, which would greatly enhance the accuracy in relating the FM and EM features.

Correlative SRM and EM has been reported in many different settings, for example on unembedded SEM samples [107], plastic-embedded TEM samples [108–110], and cryo-TEM samples without staining or embedding [111]. Yet correlative SRM and EM imaging remains sub-optimal since the imaging quality of one technique is generally compromised by improvements in the other. For example, EM fixation and staining reagents, which are important for preserving cellular ultrastructures and providing good EM image contrast, are detrimental to organic dyes and fluorescent proteins in terms of fluorescence intensity and switching properties. Several studies [108–110,112] were carried out to optimize the TEM sample preparation process for correlative imaging. These studies included variations in fluorescent molecules, embedding resins, and the fixation and staining protocol. Paez-Segalaet *et al.* [110] have engineered two mEos4 variants, mEos4a and mEos4b, and demonstrated that they retained their fluorescence and photoswitching properties after 0.5-1% OsO_4 fixation in the hydrophilic resin glycol

methacrylate (GMA). It was noted that these mEos4 variants did not survive in the EPON resin, which typically provides better ultrastructure preservation compared to GMA. Chemical tags such as the SNAP-tag have also been used successfully for correlative SRM and EM [113]. A comprehensive work by Watanabe *et al.* optimized each step of the sample preparation [108]. They used 0.001% osmium tetroxide supplemented with 0.1% potassium permanganate, and the combination showed better preservation of cellular morphology of neurons than using a low concentration of osmium tetroxide (0.1%) as the fixative. As for resins, GMA embedded samples were reported to generate the brightest fluorescence signals for Citrine and tdEos as compared to other choices of hydrophilic resins such as Lowicryl K4M, LR Gold, and LR White. As pointed out earlier, however, these hydrophilic resins yield lower sectioning and imaging qualities due to poor polymerization despite the better preservation of fluorescence.

There have also been useful attempts to combine SRM with cryo-TEM to image samples at cryogenic temperatures. Fast freezing techniques allow vitrification of biological samples in amorphous ice without disrupting the cellular structure. Samples prepared in this way are free of chemical fixatives and the associated artifacts, and are immobilized in their native state. A correlated cryo-PALM and cryo-electron tomography (CET) method was introduced recently to resolve structures of type VI secretion system (T6SS) in V. cholera at macromolecular resolution [111]. Due to their dynamic nature and random localization within the cell, T6SS structures are hard to identify in cryo-tomograms. To overcome this difficulty, cryo-PALM was developed to localize the sheath protein VipA tagged with PA-GFP in frozen-hydrated cells on EM grids. However, to date, cryo-PALM has achieved limited spatial resolution for a number of reasons: the photon yield from PA-

GFP is low at a temperature of 80 K, a long-working distance objective with a moderate NA of 0.7 had to be used for imaging samples placed in the cryo chamber, and the excitation laser power must remain low to avoid devitrification of the sample. Within these limitations, on average only ~200 photons were collected for each PA-GFP molecule. Nevertheless, SRM and CET offer the best spatial resolution in FM and EM, respectively, and further improvements to correlative SEM and CET would potentially enable high-resolution structural analysis of proteins and protein complexes in their native environment without fixation artifacts.

1.4. Layout of the thesis

The remainder of the thesis is organized as follows. Chapter 2 focuses on developing a correlative SRM and SEM imaging workflow and optimizing EM sample preparation to better preserve biological samples. In Chapter 3, the correlative imaging workflow developed was applied to visualize and identify membrane nanodomains that organize Ras multimers and regulate isoform specific signaling. Chapters 4 introduces DNA-PAINT as the future work for multiplexed imaging in an effort to further identify compositions of membrane components regulate Ras activity.

Chapter II. Quantitating morphological changes in biological samples during SEM sample preparation with correlative super-resolution microscopy [114]

Ying Zhang, Tao Huang, Danielle M. Jorgens, Andrew Nickerson, Li-Jung Lin, Joshua Pelz, Joe W. Gray, Claudia S. López , Xiaolin Nan

Author contributions

Y. Zhang and X. Nan developed the hypothesis, conceptual and experimental designs, and are responsible for data analysis and interpretation. Y. Zhang performed all experiments and image analysis. For developing correlative imaging, T. Huang, A. Nickerson, L.J. Lin and J. Pelz assisted with experimental design. D.M. Jorgens and C.S. López helped with SEM instrument training. Y. Zhang and X. Nan wrote the manuscript with the help of C.S. López and J.W. Gray.

Abstract

Sample preparation is critical to biological electron microscopy (EM), and there have been continuous efforts on optimizing the procedures to best preserve structures of interest in the sample. However, a quantitative characterization of the morphological changes associated with each step in EM sample preparation is currently lacking. Using correlative EM and super-resolution microscopy (SRM), we have examined the effects of different drying methods as well as osmium tetroxide (OsO_4) post-fixation on cell morphology during scanning electron microscopy (SEM) sample preparation. Here, SRM images of the sample acquired under hydrated conditions were used as a baseline for evaluating morphological changes as the sample went through SEM sample processing. We found that both chemical drying and critical point drying lead to a mild cellular boundary retraction of ~60 nm. Post-fixation by OsO_4 causes at least 40 nm additional boundary retraction. We also found that coating coverslips with adhesion molecules such as fibronectin prior to cell plating helps reduce cell distortion from OsO_4 post-fixation. These quantitative measurements offer useful information for identifying causes of cell distortions in SEM sample preparation and improving current procedures.

Introduction

Scanning electron microscopy (SEM) is extensively used to study structural details on the surface of biological samples. The conventional sample preparation process for SEM includes fixation, dehydration, drying, and optionally, conductive coating. Fixation is typically performed in aldehyde buffer; in certain cases, this is followed by a post-fixation step in osmium tetroxide (OsO_4) or uranyl acetate (UA). After fixation, the sample is first dehydrated with organic solvents to replace water and then dried to remove the organic solvents. Each of these steps, i.e., fixation, dehydration, and drying, can introduce artifacts into delicate biological samples such as change in protein localization [115]. Morphological changes were also reported during fixation and drying steps [116]. Much effort has been put into optimizing these procedures to reduce sample preparation artifacts and preserve cell structures and morphology as closely to the native state as possible [117–121]. Such efforts, however, are often based on empirical assessment of the sample quality after preparation, and a quantitative characterization of the morphological changes caused by each step is currently lacking.

It is commonly believed the majority of morphological changes occur in the drying step. Critical point drying (CPD) and chemical drying are most commonly used in SEM sample preparation. In CPD, liquid CO_2 is added to the sample to replace the organic solvent and then brought to the critical point with increased temperature and pressure, when the liquid and gaseous phases coexist without a boundary. Next, all the liquid is driven to the gas phase by decreasing pressure; this allows removal of liquid from cells without surface tension effects [122]. In chemical drying, an organic solvent is gradually replaced with a volatile chemical with low surface tension, such as hexamethyldisilazane (HMDS),

which is then air-dried to completion [123]. HMDS is typically used as a time-saving and cheaper alternative to CPD. In terms of sample preservation, CPD usually is better although some have reported that CPD and HMDS yield similar results [124]. While CPD and HMDS seem to suffice for most biological specimens, drying artifacts such as lines and ridges on the cell surface due to cell shrinkage and even cellular collapse have been documented for both methods [125].

Post-fixation with OsO_4 is reported to help preserve cellular structure by reacting with lipids, which are the main components of the cell membrane and intracellular organelles but are not fixed by aldehydes. However, OsO_4 treatment has also been shown to alter cell morphology. For example, Nordestgaard and Rostgaard [126,127] quantitatively traced volume changes by Nomarski differential interference contrast microscopy in isolated hepatocytes during EM specimen preparation. Swelling ranged from 9 to 19% during secondary fixation in 2% OsO_4. Additionally, OsO_4 is a strong oxidizing reagent and may cause undesired destruction of membrane components [128], which may be a concern in certain applications such as immuno SEM.

Continued improvement of SEM sample preparation requires a clear understanding of the changes to the specimen during each step, which necessitates the use of light microscopy. Several methods had been used for tracing the volume changes of tissues or cells during each stage of sample preparation. Time-lapse cinematography with light microscopy was used by Boyde [120] and Arborgh [121] to record continuous dimensional changes in cultured cells. Other optical methods including Nomarski [129,130] or phase-contrast optics [118] were also used. Sample shrinkage was also estimated by measuring the gross dimensions of tissue sample [131] or measuring the gross weight loss [132].

However, these methods fall short in distinguishing the influence of each sample preparation step on individual cells. Often times evaluation of sample quality at fine scales has to be based on SEM imaging results when all steps have already been completed, making it difficult to account for the contributions of individual steps.

Recently, the resolution gap between light and electron microscopy has been filled by super-resolution microscopy (SRM) techniques such as photoactivated localization microscopy (PALM) and stochastic optical reconstruction microscopy (STORM). Based on stochastic switching and subdiffractive localization of individual fluorescent molecules, both PALM and STORM offer spatial resolutions on the order of 10 nm. For their high resolving power and compatibility with existing fluorescence labeling approaches, PALM and STORM have been widely used for imaging biological samples to reveal otherwise hidden details [102,133]. More recently, correlative SRM and EM have combined their complementary capabilities in biological imaging, where SRM provides the target specific contrast and EM the morphological features.

In this chapter, we used SRM to examine morphological changes to the sample during SEM sample preparation. Using SRM images of fully hydrated samples as a standard, we were able to quantitate differences in the cell morphology as the sample goes through different SEM processing steps and imaged with the SEM, after which the two images were precisely registered and compared. We introduced a distortion index as a quantitative indicator for the extent of distortions in cellular shape. Using this approach, we found that the dehydration and drying steps caused a mild boundary retraction at an average of 60 nm to cells cultured on glass, and the effect was similar between CPD and chemical drying using HMDS. Post-fixation by OsO_4 causes at least an additional 40 nm boundary

retraction; this result contrasts current beliefs that OsO_4 helps to preserve cell morphology. Lastly, we showed that fibronectin coating of coverslips prior to cell plating helps to significantly reduce cell distortion from OsO_4 post-fixation. These findings offer quantitative insight into factors that affect SEM sample quality, which will be helpful to improve the current procedures for better SEM sample preservation.

2.1. Materials and Methods

2.1.1. Molecular cloning and establishment of stable cell lines

We used two genetically encoded photoactivatable fluorescent proteins, mEos4 and PAmCherry1, to label tubulin and the C-terminal tail of H-Ras (tH) respectively. The mEos4 plasmid was a gift from Dr. Loren Looger (Janelia Farm)[110]. To generate expression plasmids for mEos4-tubulin and PAmCherry1-tH, PCR fragments used for In-Fusion reactions were generated using Phusion High-Fidelity DNA Polymerase (M0530, New England Biolabs). We used the In-Fusion PCR HD Cloning kit (Catalog number 639649, Clontech) to generate genetic fusions in the pENTR (Life Technologies) backbones, and the Gateway LR Clonase II kit (11791, Life Technologies) to shuttle the resulting fusion constructs from the entry clones to expression clones. Lentiviral backbone (pLenti-puro-CMV/TetOn, 17293, Addgene) was used for expressing these clones. Viral particles containing the pLenti-puro-CMV/Teton-mEos4-tubulin or pLenti-puro-CMV/Teton-PAmCherry1-tH were generated using the ViraPower lentiviral packaging system (K497500, Life Technologies), which were then used to infect U2OS cells (HTB-96, ATCC) to make stable cell lines expressing mEos4-tubulin or PAmCherry1-tH under

tetracycline or doxycline regulation. Single clones were isolated, grown out and assayed for repression of Dox-induced gene expression; good clones were used for subsequent studies.

2.1.2. Sample preparation for correlative microscopy

Cells were cultured at 37°C and 5% CO_2 in DMEM supplemented with 10% FBS (11995 and 10082 respectively, Life Technologies) and were plated on #1.5 indium-tin-oxide (ITO) coated coverslips (SPI supplies 06486-AB). To grow cells on fibronectin coated coverslips, a 5 or 10 µg/mL fibronectin solution was added to the ITO coated coverslips and incubated at room temperature for 3 hours. Excess fibronectin was removed by aspiration before plating cells. Primary fixation of cells was performed with freshly made 3.0% glutaraldehyde or 3.7% PFA and 0.1% glutaraldehyde in PBS for 20 min at room temperature. For PALM imaging of microtubules, cells were first extracted for 60 seconds with 0.1% Triton X-100 before fixation.

After PALM imaging, the PAmCherry1-tH samples were post-fixed at room temperature with 1%, 2% (v/v) or without OsO_4. The samples were then dehydrated by a graded series of ethanol (50%, 60%, 70%, 80%, 90%, 95% and three times 100%) at 20 minute intervals. Following dehydration, solvent was removed by either CPD using a critical point dryer (CPD300, Leica) or air drying with HMDS (440191, Sigma-Aldrich). For HMDS drying, the dehydrated specimens were immersed with HMDS for 20 minutes. Then HMDS was decanted, and the samples were left under a hood to air-dry at room temperature. Samples were then coated with 5 nm carbon using a Leica ACE600 Coater before SEM imaging.

To label U2OS cells with wheat germ agglutinin (WGA) for STORM imaging, the cells were first fixed with 3.7% PFA and 0.1% glutaraldehyde. After washing with PBS, the cells were blocked with 3% (w/v) bovine serum albumin (BSA, 9048-46-8, OmniPur) in PBS for 30 minutes. The cells were then incubated with Alexa Fluor 647 conjugated WGA (W32466, Thermo Fisher Scientific) at 1 μg/mL for 30 min before and after OsO_4 post-fixation. The cells were thoroughly washed with PBS and stored in the same buffer until STORM imaging.

2.1.3. SRM and SEM imaging and image registration

For imaging mEos4-tubulin and PAmCherry1-tH with PALM, PBS with Ca^{2+}/Mg^{2+} (14040133, Life Technologies) was used as the imaging buffer. For imaging WGA-Alexa Fluor 647 with STORM, we used a standard STORM imaging buffer containing 10 mM mercaptoethylamine (MEA, M9768, Sigma-Aldrich) and an oxygen scavenger system [0.5 mg/mL glucose oxidase (G2133, Sigma-Aldrich), 40 μg/mL catalase (C100-50MG, Sigma-Aldrich), and 10% w/v glucose] in a Tris buffer (50 mM Tris supplemented with 20 mM $MgCl_2$ and 10 mM NaCl, pH 8). The STORM imaging buffer was made fresh prior to each imaging session.

SRM (i.e., PALM and STORM) imaging was performed on a Nikon Ti-U inverted microscope equipped with a Nikon 60× APO TIRF objective (NA = 1.49). Total internal reflection (TIR) illumination was used in all SRM imaging experiments. Gold particles (~100 nm in size, Cytodiagnotics, G-100-20) were added to the imaging buffer about 20-30 min prior to imaging so they could adhere to the coverslip and be used as fiduciaries. Unlike PALM and STORM fluorophores (e.g. mEos4, PAmCherry1, and Alexa Fluo 647) that undergo photoswitching between frames, these gold nanoparticles emit fluorescence

continuously; a stably adherent gold nanoparticle can be localized to at least 10-20 nm precision in each frame and thus can be used as a reference to correct for stage drift during PALM/STORM image acquisition. By averaging trajectories of multiple gold nanoparticles, stage drift could usually be corrected to better than 5 nm. An open source software, μManager [134], was used to acquire raw SRM images. SRM image reconstruction was performed using home-written scripts in Matlab (MathWorks, MA).

SEM images were taken at 2 kV with a FEI Helios 650 Nanolab FIB/SEM. All imaging was performed using the solid state concentric backscatter detector at a working distance of 4 mm.

Since the gold particles can be localized with high precision (better than 5 nm) in both SRM and SEM, they were used to align and register all correlative SRM - SEM datasets. Image registration was done using custom scripts based on the Control Point Registration toolbox in Matlab (Mathworks, Natick, MA). Typically a total number of 15-20 gold nanoparticles were used to register each SRM-SEM dataset.

2.1.4. Quantitation of cell distortion

After image registration using gold nanoparticles as fiduciary markers, correlated SRM and SEM images were both analyzed with custom Matlab scripts to define the cell boundaries using functions built in the Imaging Processing Toolbox. The distortion in cell morphology was calculated as the total area between the cell boundaries (white and green lines in Fig 2.1) in the two images, which is dependent on the contour length of the cell boundary. To obtain a normalized distortion value, the SRM image was first divided into 100 x 100 nm^2 blocks (Fig 2.1); the total area of boundary blocks (Fig 2.1, gray) was then

determined by counting the number of blocks at the SRM image boundary (Fig 2.1, green), which is then used to normalize the area difference between the two boundaries. This yields a *Distortion Index* defined as,

$$Distortin\ Index\ = \frac{Total\ area\ between\ boundaries}{Total\ area\ of\ boundary\ blocks}$$

In essence, the *Distortion Index* describes the average distance between the two boundaries in units of 100 nm; in other words, a *Distortion Index* of 1 indicates that there is a 100 nm distance across the two cell boundaries on average. Of note, both retraction and expansion contribute positively to the total area difference between boundaries.

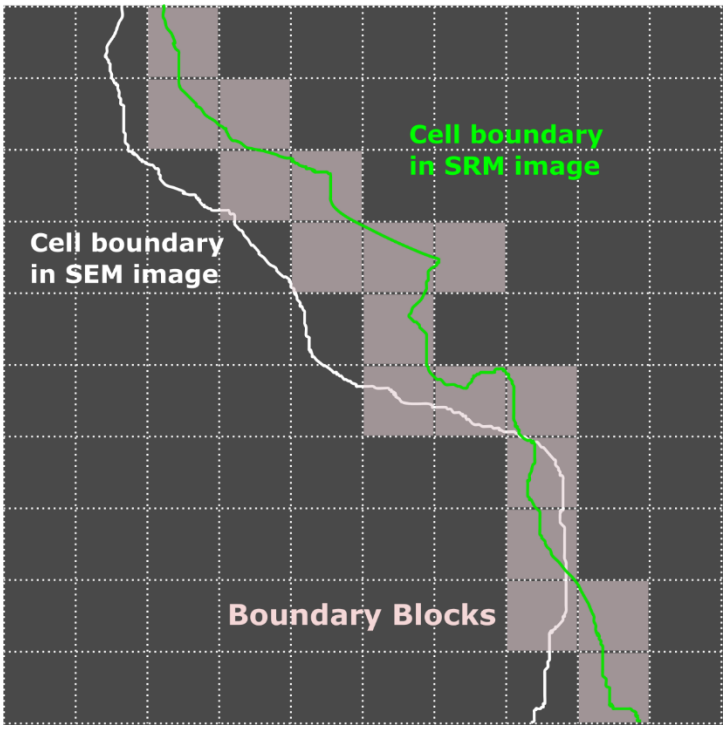

Figure 2.1 Schematics for quantitating morphological changes in correlative SRM and EM images. Cell boundaries in both SRM (green) and SEM (white) images are defined with custom Matlab scripts. The SRM image is also divided into 100 x 100 nm^2 blocks. The difference in cell areas are calculated and normalized to the contour length determined by counting the number of blocks (gray) along the cell boundary in the SRM image (green). As such, both the area difference and contour length have the units of nm^2.

2.2. Results

2.2.1. Correlative PALM and SEM imaging

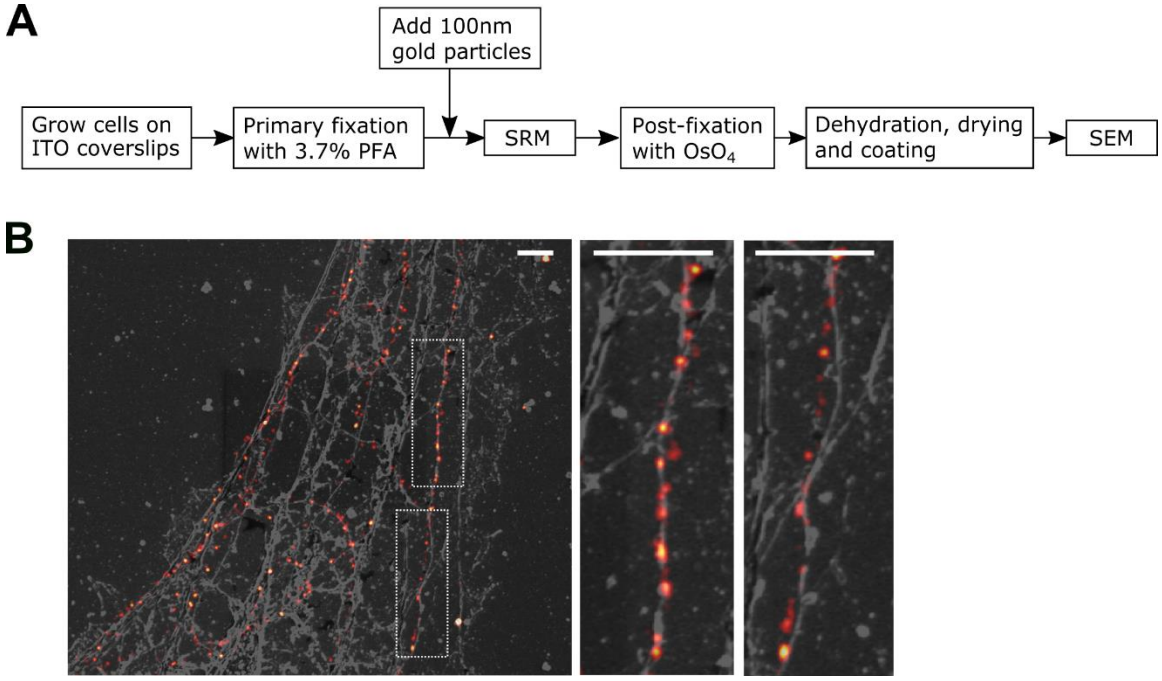

Figure 2.2 Correlative SRM and SEM imaging. (A) Workflow of imaging the same cell with correlative SRM and SEM; (B) Correlative SRM and SEM image of U2OS cells expressing mEos4 tagged tubulin. Magnified views of the boxed regions in the left image are shown to the right. Scale bars, 1 µm.

We first tested the correlative workflow (Fig 2.2A) by imaging microtubules. Microtubules are about 25 nm in diameter and are typically single filaments; the microtubule network in U2OS cells was well resolved by imaging mEos4-tubulin with PALM (red in Fig 2.2B). Here the cells were briefly extracted with detergent to remove tubulin monomers, the membrane, and many other soluble cytosolic components; the cytoskeleton, including microtubules, was left behind in this process. The sample then went through SEM sample preparation and imaging. We were able to identify the same regions

that were imaged with PALM during SEM imaging. In SEM images, filamentous structures are also clearly visible, of which a subset represent microtubules (gray in Fig 2.2B). Indeed, many microtubule filaments revealed by PALM overlap well with filaments in the SEM image (Fig 2.2B, middle panel). A significant fraction of microtubule filaments, however, overlap loosely between the two images (Fig 2.2B, right panel), indicating morphological changes during the sample preparation.

2.2.2. Effects of different drying methods and OsO_4 post-fixation on cell morphology

In order to quantitate morphological changes during different SEM sample preparation procedures, we applied the workflow shown in Fig 2.2A to image U2OS cells overexpressing PAmCherry1-tH, which targets to the cell membrane and demarcates the cell boundary with approximately 20 nm spatial resolution in the PALM images (Fig 2.3A-G, red). Next, the sample was processed for SEM imaging and the same cell of interest was located (Fig 2.3A-G, gray). In both PALM and SEM images, 100 nm gold nanoparticles were present, allowing us to register the two images with high precision. Of note, the SRM images were rendered by using all raw localizations without combining any events even if they were from the same molecules or gold nanoparticles; in this case, the gold nanoparticles appeared as a halo of 80-100 nm, but the mean location of the gold nanoparticle could be determined with better than 5 nm accuracy (typically 2-3 nm). The mean locations of gold nanoparticles in the SRM images were used for registration with the corresponding SEM images to achieve better than 20 nm precision (typically better than 10 nm, Figs 2.3E and F). Differences in the cell boundaries became evident at this

resolution in the registered PALM – SEM images (Fig 2.3G), which were quantitated using the approach described in Fig 2.1, as shown in Fig 2.3G-J.

We have also observed retraction of cell boundaries by ~100 nm, more evidently at the trailing edge (Fig 2.3A) than at the leading edge, which usually displays a high density of protrusions (Fig 2.3B). In order to obtain unbiased quantitation, we calculated cell distortion from different regions of the cell boundary that make up the cell contour. Fig 2.4 shows example images and the quantitation results of cell distortion under different fixation and drying methods. Among all the situations examined, shrinkage accounts for most of the cell distortions. Boundary retraction was apparent in samples dried with either CPD or HMDS. For samples fixed with the 3.7% paraformaldehyde and 0.1% glutaraldehyde only, the two drying methods resulted in a cell distortion index of 0.64 and 0.60, corresponding to an average cell border retraction of 64 and 60 nm, respectively. For samples dried with CPD, primary fixation using 3% glutaraldehyde slightly reduced the distortion index from 0.64 to 0.56, compared with using 3.7% paraformaldehyde and 0.1% glutaraldehyde as the primary fixative (Fig 2.4B). However, Strong glutaraldehyde fixation could negatively impact the immunogenicity of biological specimen due to its high crosslinking activity [135,136]. Hence, for correlative imaging, 3.7% paraformaldehyde and 0.1% glutaraldehyde is deemed more suitable without sacrificing sample quality for SRM [137].

Additionally, we have examined whether OsO_4 post-fixation helps to preserve cell morphology and to reduce cellular distortion. After primary fixation and SRM imaging, U2OS cells were post-fixed with 1% or 2% OsO_4 before dehydration and drying. We found that post-fixation by OsO_4 caused greater cell distortions compared to the samples only fixed by aldehyde buffer, and the distortions increased with higher OsO_4 concentration (Fig

2.4A). Among samples dried by CPD, the calculated cell distortion index with 1% OsO_4 post-fixation was 1.29, which doubles the index of samples without OsO_4 post-fixation (0.64). The distortion index further increased to 1.51 in samples treated with 2% OsO_4. Of note, these distortion index values represent an average magnitude of cell membrane retraction of 64 nm, 128 nm and 151 nm for no OsO_4 post-fixation, 1% and 2% OsO_4 post-fixation, respectively. A similar trend was observed for HMDS dried samples, where post-fixation with 1% and 2% OsO_4 led to evidently more cell distortion.

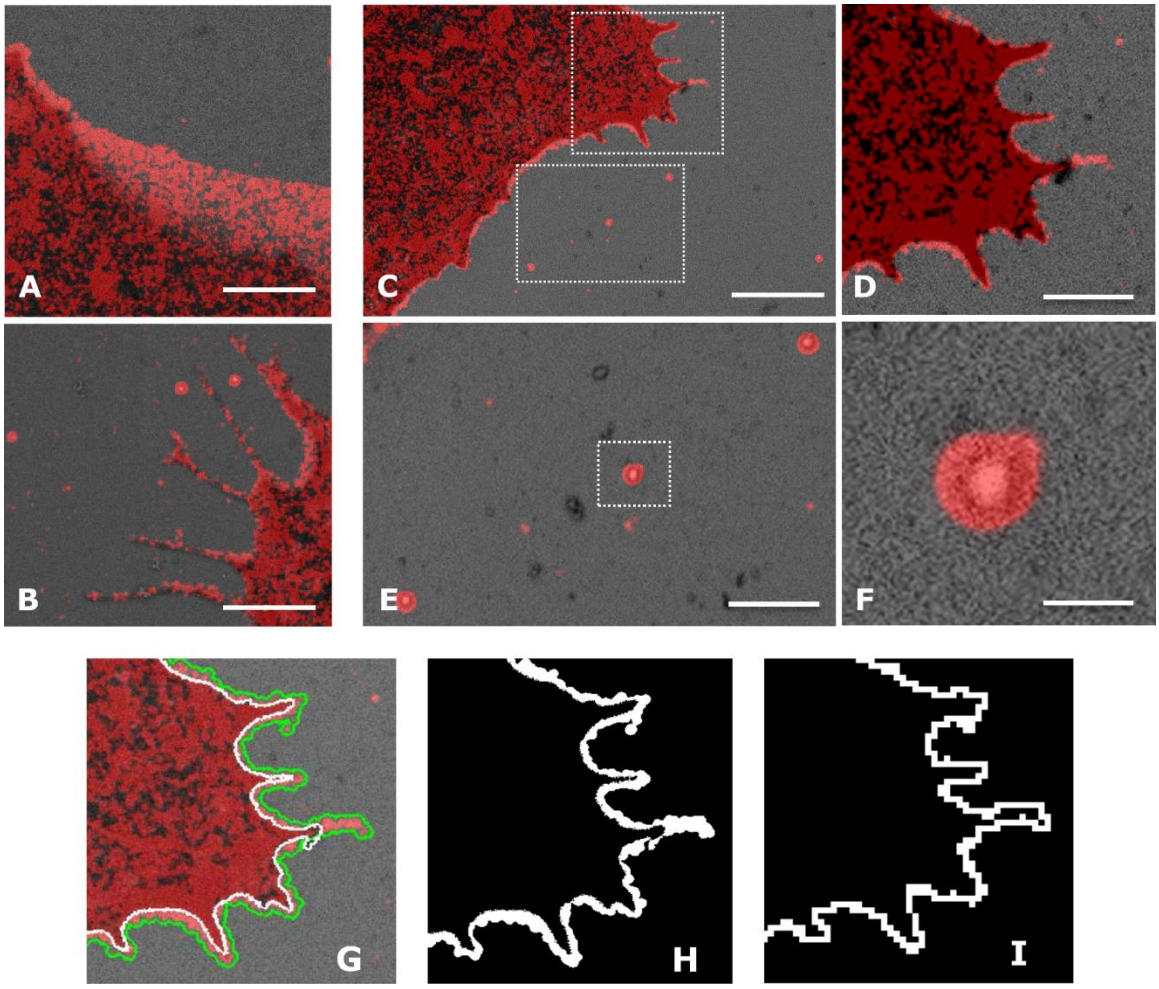

Figure 2.3 Image registration and quantitation of cell distortion. (A, B, C) Registered SRM and SEM image of U2OS cells expressing PAmCherry1 tagged with the C-terminal tail of H-Ras. Distortions in cell morphology were evident in multiple regions of the cell; (D, E) Magnified views of the boxed regions in (C); Gold particles are both fluorescent

and electron dense and thus were seen in both the SRM and the SEM images (E, F); (F) Magnified view of the gold particles in (E); (G) Defining cell boundaries in the SRM (green line) and the SEM (white line) image; (H) Area difference between the cells boundaries in the two images in (G); (I) Total area of the blocks that fell on the boundary of the SRM image ('boundary blocks') were used to represent the contour length in units of nm^2 and to normalize the area difference. Scale bars, 1 µm in (A, B, D and E), 2 µm in (C), and 100 nm in (F).

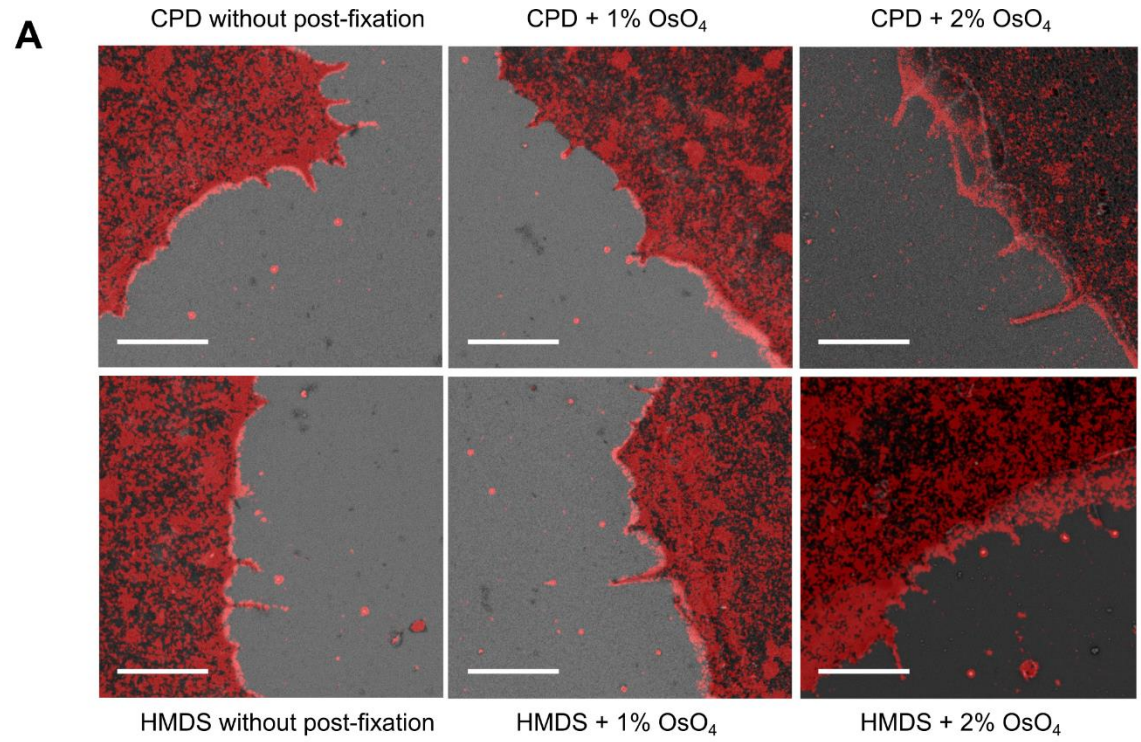

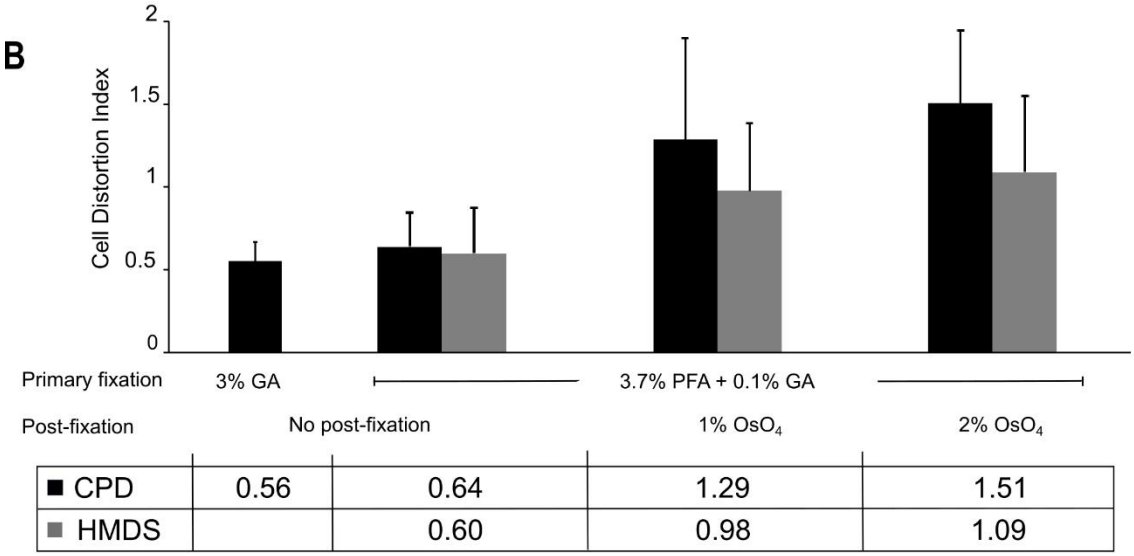

■ CPD	0.56	0.64	1.29	1.51
■ HMDS		0.60	0.98	1.09

Figure 2.4 Cell distortion under different fixation and drying conditions. In sample either dried with CPD or HMDS, larger cell distortions were observed with OsO_4 post-fixation (A). The resulting images were then quantitatively analyzed for distortion (B) as described earlier. Effects of different primary fixation, drying and post-fixation conditions on cell distortion were examined. For each condition, images of 16-20 cells from 4-5 experiments were analyzed. Error bars represent standard deviations. Scale bars, 2 µm in (A).

2.2.3. Characterizing effects of OsO_4 post-fixation with SRM

To further verify effects of OsO_4 post-fixation on the observed morphological changes, we took STORM images of the same cells before and after OsO_4 post-fixation. In this case, the sample remained hydrated and no drying or other steps for SEM sample preparation were involved. We labeled the cells with wheat germ agglutinin (WGA) conjugated to Alexa Fluor 647 for STORM imaging. WGA is a carbohydrate-binding protein that recognizes sialic acid and N-acetylglucosaminyl sugar residues, both highly abundant on the plasma membrane [138]. Fluorescent WGA effectively labels plasma membranes and can be used as a counter stain to outline cells in STORM imaging.

STORM images of the same cells before and after post-fixation were registered using the same Matlab routines as described for SRM-SEM image registration (Fig 2.5A-C). Changes in cell morphology, including cell shrinkage, protrusion distortion and discontinued membrane features after 1% OsO_4 post-fixation were commonly observed (Fig 2.5D-F). Additionally, much of the WGA labeling was lost after OsO_4 post-fixation, and the cell boundary in the STORM images became discontinuous, making it difficult to accurately define the cell contour. To quantitate cell boundary distortion, we draw a broad line perpendicular to each visually detected membrane segment in the registered pre- and post-fixation SRM images (yellow line in Fig 2.5G). Then the intensity profiles of both pre- (red in Fig. 2.5G) and post- (green in Fig 2.5G) fixation image segments were plotted along the distance of the line (Fig 2.5H). The cells boundaries from both channels were defined as the position at the half maximum intensities (dashed line in Fig 2.5H). Cell distortion was then calculated as the distance between the two boundary positions. As such, we clearly observed that 1% OsO_4 post-fixation alone caused an average of 120 nm cell

boundary retraction on the sample (Fig 2.5I), even in the absence of dehydration or drying steps. Damage to the WGA signal was too high in samples treated with 2% OsO_4 to permit a reliable estimation of the morphological change.

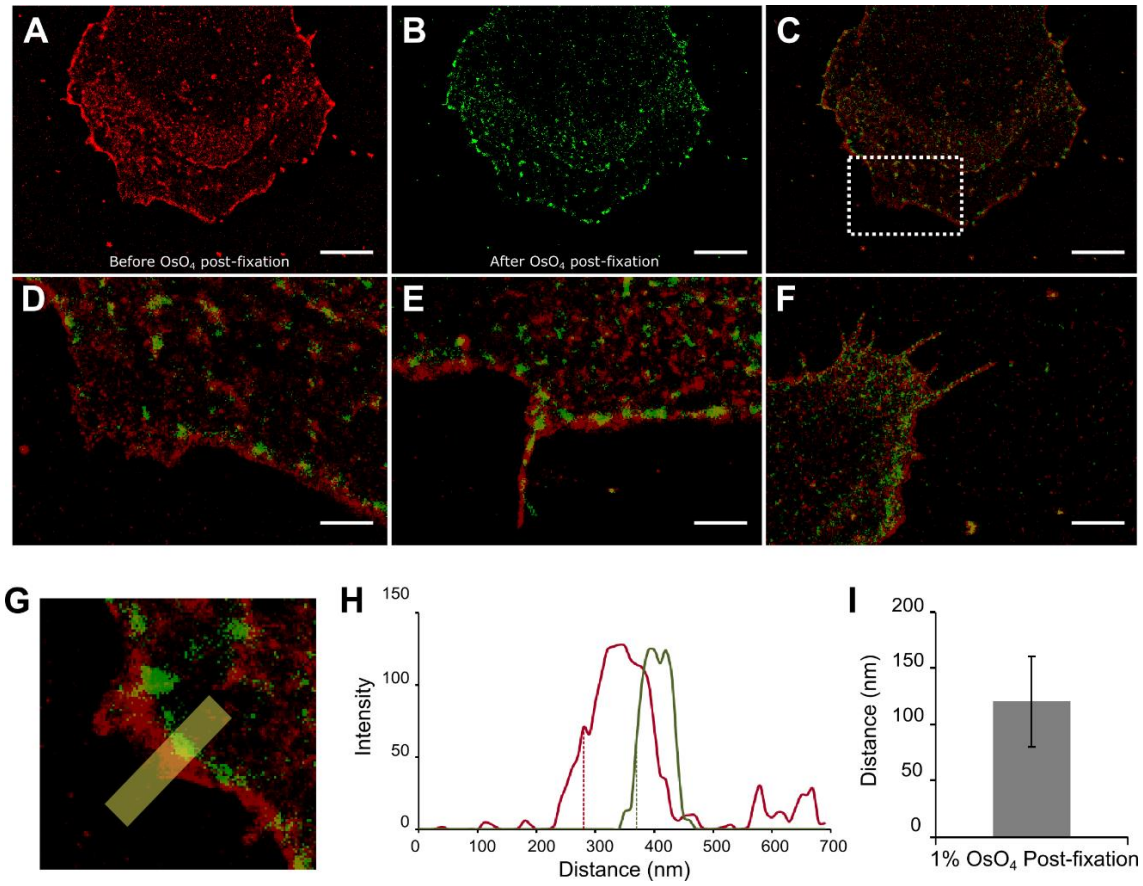

Figure 2.5 Effects of OsO4 post-fixation on cell morphology. (A) STORM image of a cell stained with WGA conjugated to Alexa Fluor 647; (B) STORM image of the same cell after post-fixation with 1% OsO_4 and re-staining with WGA-AF 647; (C) Overlaid image of (A) and (B); (D) Magnified view of the boxed region in (C); Cell shrinkage (D), distortion of protrusions (E), and discontinued membrane features (F) after OsO_4 post-fixation were observed; (G-I) Quantitation of morphological changes after OsO_4 post-fixation. In the absence of a continuous cell boundary after post-fixation, the morphological changes were quantitated by comparing line profiles of short segments at the cell boundary, where features were present in both images (G). In both line profiles, the 'forefront' of the cell boundary was defined as the pixel position at the half maximum intensities (H), and the distortion was then calculated as the distance difference between the two positions; (I) Average cell distortion after 1% OsO_4 post-fixation (n = 20). The error bar represents standard deviation. Scale bars, 5 µm in (A, B and C), 1 µm in (D, E) and 2 µm in (F).

2.2.4. Fibronectin coating alleviates morphological changes by OsO_4 post-fixation

Since less cell distortion was observed mostly at the leading edge of cells, improving cell adhesion may help preserve cell morphology. Among other cell adhesion molecules, fibronectin is an extracellular matrix protein that mediates cellular interactions with extracellular matrix components via integrins and other fibronectin receptors. It is often used to coat glass or plastic surfaces to enhance cell attachment *in vitro*. We therefore investigated whether fibronectin would help stabilize cell morphology during SEM sample preparation.

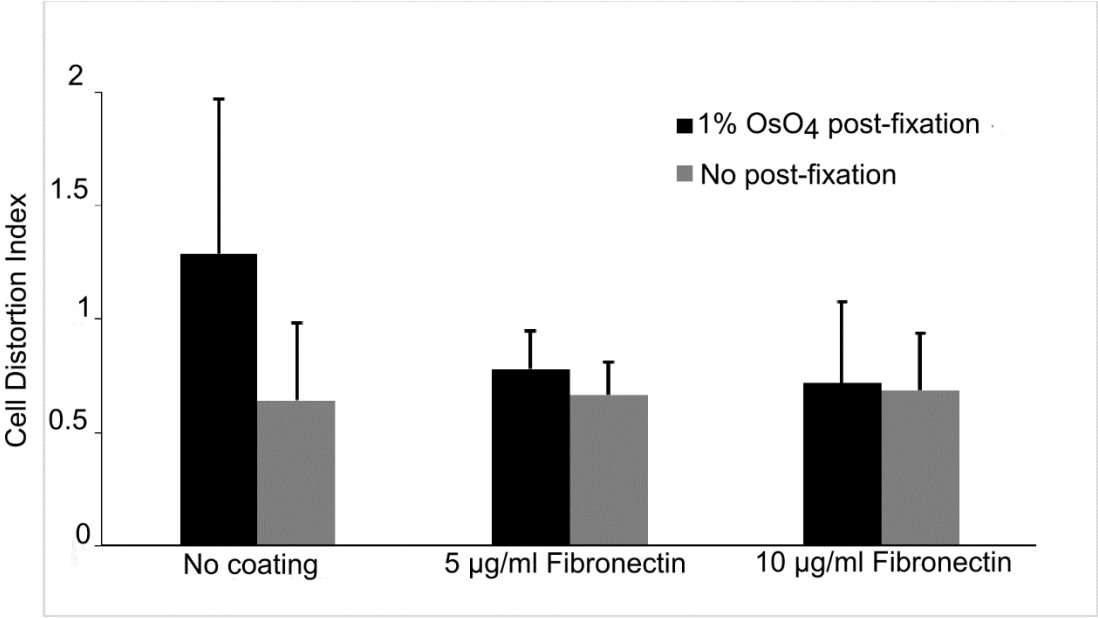

Figure 2.6 Growing cells on fibronectin-coated coverslips reduced morphological changes by OsO4 post-fixation. The cells were grown on non-coated coverslips (left) or those coated with 5 µg/mL (middle) or 10 µg/mL (right) fibronectin, fixed in an aldehyde buffer, then processed either directly (gray bars) or after OsO_4 post-fixation (black bars) for SEM. The cell distortion index was reduced from 1.29 to 0.78 and 0.72 after coating with 5 or 10 µg/mL fibronectin, respectively (black bars). For samples only fixed with the aldehyde buffer (3.7% paraformaldehyde plus 0.1% glutaraldehyde, gray bars), morphology preservation was not evidently improved by fibronectin coating.

Indeed, cells grown on ITO coverslips pre-coated with 5 or 10 µg/mL fibronectin showed much reduced the cellular distortion caused by OsO_4 post-fixation (Fig 2.6). Cell distortion indices were reduced from 1.29 to 0.78 and 0.72 with 5 and 10 µg/mL fibronectin coating, respectively. With fibronectin coating, the distortion indices were approaching that of cells grown on bare ITO without OsO_4 post-fixation (0.64). Importantly, fibronectin coating did not improve morphological distortion index for samples that were fixed only with primary aldehyde fixatives (Fig 2.6). These data suggest that substrate coating with fibronectin mostly protected cells from distortion by OsO_4 post-fixation but not from shrinkage during dehydration and drying.

2.3. Discussion

Correlative SRM and EM promises to be a powerful tool for studying protein localization and organization in the native cellular context [107]. For workflows that perform SRM before EM, it is important to ensure that the cell morphology is well preserved when the sample goes through the preparation steps. In this study, we have examined morphological changes to adherent cells grown on a solid substrate during SEM sample preparation, by imaging the cells with SRM in hydrated state prior to SEM sample processing. Our results indicate that the degree of cell distortion, measured as the differences between the cell boundaries defined by SRM and SEM images, ranges from ~60 nm to ~130 nm depending on the sample processing protocol. For example, post-fixation with OsO_4 causes more pronounced cell boundary retraction whereas fibronectin coating helps reduce the morphological change. These quantitative measurements help to

identify factors that contribute to cell distortion during SEM sample processing and to develop strategies to better preserve cellular structure.

OsO_4 has been extensively used as a post fixative and staining reagent in EM for preserving ultrastructure and providing membrane contrast, but its exact effects on biological specimen have not been clearly understood. Our study shows that OsO_4 causes slight shrinkage of the cell boundaries. This shrinkage is likely due to the strong oxidizing activities of OsO_4 that, while important for staining membranes [139], may also destroy some adhesion molecules that help the cell to attach to the substrate. Consistently, we have observed that OsO_4 post-fixation caused loss of WGA-binding sites in cells, some of which is attributed to cell surface glycans. This adverse effect of OsO_4 is further corroborated by the fact that coating the substrate with fibronectin almost completely reversed the shrinkage caused by OsO_4 treatment. Here, the role of fibronectin is likely to enhance cell attachment to the substrate, by making the cell - substrate interface more resistant to OsO_4 treatment.

Similar effects of cell attachment on OsO_4 resistance were also observed on cells with a leading and trailing edge, indicative of cell migration. As shown in Fig 2.3 (A, B), the leading edge of the cell usually experiences significantly less morphological changes than the trailing edge. The leading edge is typically characterized by a flat morphology and a higher density of protrusions, where integrins, extracellular matrix proteins, and adapter proteins form adhesion complexes to mediate cell attachment [140]. The trailing edge is where the adhesion complexes dissolve to allow the cell body to migrate in the direction of movement, resulting in a loose attachment with the substrate. Hence, coating with fibronectin and potentially other molecules that improve cell adhesion seems a viable approach to counter the cell boundary retraction observed during OsO_4 post-fixation.

It is worth mentioning that previous reports seem to mostly suggest that OsO_4 post-fixation cause cell swelling, which was attributed to a difference between the osmotic pressure of the fixative and that of the cytoplasm [126]. This does not necessarily contradict our observation, because a retraction in cell boundary does not prevent the rest of the cell body from expanding. For example, the cells may have a slightly reduced footprint but become significantly taller (i.e., overall rounding of the cell), and the net result is increased volume. Therefore, a complete assessment in the morphological change of cells during SEM sample preparation should compare SRM and SEM images of the same cell in all three dimensions. While whole cell imaging with SEM is possible with volumetric techniques such as FIB-SEM, similar imaging with SRM with comparable resolutions is still in development [141]. Future work can utilize three dimensional super-resolution techniques combined with volumetric SEM (such as FIB-SEM) to evaluate these effects during sample preparation.

In this study, we also compared CPD and chemical drying with HMDS, which are two of the most commonly used drying methods for biological specimen. Our results indicate that CPD and HMDS yielded comparable cell boundary distortion. Between the two, CPD has been the popular drying method designed to avoid artifacts due to surface tension. HMDS is a cheaper and time-saving alternative that has been proven to work with most biological sample types [117,142,143]. Together, CPD may still offer some advantages in terms of preserving cell morphology although HMDS seems to suffice for many samples.

Approaches for correlative SRM and EM have been reported for imaging plastic-embedded TEM samples. The sample preparation procedures for those samples including

high pressure freezing, freeze substitution and resin embedding are critical for preserving cell morphology and cellular structures. Preserving cell morphology in these experiments is similarly of concern, and the workflows developed here could potentially be adopted for quantitation of morphological changes in those cases. With information provided through these measurements, specific steps in the sample processing procedures of these experiments may be modified for optimal preservation of specimen morphology and ultrastructure.

Chapter III. Cortical cytoskeleton and dynamin-dependent membrane compartments differentially regulate Ras multimer formation and signaling

Ying Zhang, Lei Wu, Yerim Lee, Young Hwan Chang, and Xiaolin Nan

Author contributions

Y. Zhang and X. Nan developed the hypothesis, conceptual and experimental designs, and are responsible for data analysis and interpretation. L.J. Lin and A. Nickerson established the stable cells lines. Y. Zhang developed correlative imaging workflow and performed all experiments. Y.H. Chang, Y. Lee and Y. Zhang developed the image analysis. L. Wu assisted with western blot. Y. Zhang and X. Nan wrote the manuscript.

Abstract

Multimer formation in specialized membrane compartments has been implicated in Ras signaling, but the identities of these compartments and how they regulate Ras multimer formation and signaling remain unclear. Here, we combined super-resolution and scanning electron microcopies to analyze the nanoscale organization of Ras and its immediate cellular context. We found that K-Ras multimers are almost exclusively associated with the cortical cytoskeleton and H-Ras multimers preferentially localize to dynamin-dependent vesicles, although their monomers showed only a weak preference to either compartment. Interestingly, Ras multimers associated with the cortical cytoskeleton are predominantly dimers, and larger multimers were only found on the membrane vesicles, indicative of distinct mechanisms of multimer formation in the two compartments. Lastly, dynamin inhibition diminished Raf-MAPK activation by H-Ras but did the opposite for K-Ras. Together, these results provide direct insight into how distinct membrane compartments differentially regulate multimer formation and signaling of different Ras isoforms.

3.1. Introduction

The membrane-bound Ras GTPases regulate essential cellular functions such as growth, proliferation, and survival through canonical pathways such as Raf-MAPK and PI3K-Akt [144]. To activate the effectors, Ras needs to be both GTP-bound and on the membrane [87]. GTP-binding is at the soluble, globular domain (G-domain, residues 1-165/166), which is also the domain for GTP hydrolysis and effector binding. Point mutations, such as those at residues G12, G13, and Q61, can lock Ras in the GTP-bound state to cause constitutive effector activation, and these Ras mutations are frequently found in human cancers [49]. For its roles in both physiologic and pathologic signaling, Ras has been studied intensively for decades, revealing rich details of how the G-domain functions. Historically, the vast majority of biochemical and structural studies on Ras have used truncated proteins comprising only the soluble G-domain and missing the C-terminal, membrane targeting motif [145]. To date, there is no high-resolution structure available for full length Ras on the membrane, and efforts to reconstitute Ras functions *in vitro* using model membranes have only had limited success. In fact, many aspects of Ras biology seem to be relevant only when Ras is on an actual cell membrane, which is far more complex in composition and structure than current model membrane systems. As a result, relatively little is known about how Ras operates on the membrane despite that it was appreciated early that the membrane is required for Ras to be biologically active. Fundamental questions, for example, why the membrane is even necessary when all the 'essential functions' of Ras seem to be contained within the G-domain, have not been addressed.

Using a combination of high-resolution imaging, live cell imaging, and other experimental and computational approaches, a series of recent studies started to suggest at least two related roles of the membrane in regulating Ras activities in cells [47,78,79,82]. First, the membrane is implicated in spatially segregating different Ras isoforms into compositionally and functionally distinct nanodomains. It is now well accepted that biological membranes are not simply fluidic lipid bilayers where proteins float freely and interact randomly; instead, subsets of lipids, proteins, and other species can transiently aggregate to yield numerous, heterogeneous membrane compartments that span many spatial and temporal scales [64]. Depending on the membrane targeting signal and biological context, each membrane-bound species could be 'sorted' into specific membrane compartments. While all Ras proteins target to the membrane through the post-translationally modified C-terminal domain, the sequence of this domain and post-translational modifications vary among Ras isoforms, hence the name hypervariable region (HVR) [19]. For example, both H-Ras and K-Ras are prenylated at the last cysteine (C186), but only H-Ras is palmitoylated at two other cysteines; another distinction is that K-Ras HVR contains a string of six lysines and is therefore positively charged, which is not the case for H-Ras. This major difference in the HVRs is expected to have a direct impact on which membrane compartment these Ras isoforms preferentially localize to [146,147]. GTP-binding status also seems to have an impact on the spatial localization of the Ras isoforms. In the current model, which is largely based on immuno-EM studies by Hancock and colleagues, H-Ras primarily targets to caveolae when GDP-bound but migrates to non-caveolae compartments when GTP-bound, whereas both K-Ras-GDP and K-Ras-GTP are in undefined, no-caveolae compartments, likely those enriched in phosphatidylserine

[47,82,148,149]. By targeting to distinct membrane compartments, the Ras isoforms may exhibit distinct biological activities in cells and in vivo [1,150]. Indeed, H-Ras and K-Ras preferentially activate PI3K and Raf, respectively, despite the fact that the two isoforms have nearly identical G-domains and both bind to Raf and PI3K in vitro. Additionally, in human cancers K-Ras is the predominantly mutated isoform (85%), followed by N-Ras (11%) and H-Ras (4%) [49].

Second, Ras may form multimers such as clusters and dimers on the membrane, potentially a direct consequence of enrichment in nanoscopic membrane compartments [46,47,86,151]. While the molecular nature and functional relevance of Ras multimers are still debated, there is strong evidence that Ras mediated activation of Raf (and potentially other effectors as well) involves Ras multimer formation. Nanoscopic clustering of H-Ras and K-Ras on the cell membrane was first observed on prepared membrane sheets, based on which it was estimated that each Ras nanocluster contains 5-8 Ras molecules [47,75]. More recently, quantitative single-molecule and super-resolution microscopy (SRM) showed that K-Ras primarily exists as mixed monomers and dimers at physiological expression levels, and higher order multimers are rare. Recombinant N-Ras may also form dimers when tethered to artificial membranes via a synthetic linker [152], but the same still needs to be validated for H-Ras and K-Ras. Both Ras nanoclusters and dimers have been implicated in Raf-MAPK activation. Conditions such as depletion of cholesterol using cyclodextrin and depolymerization of the actin cytoskeleton using latrunculin-A reduced nanocluster formation of H-Ras and K-Ras, respectively, as well as Raf-MAPK activation. Force dimerization of monomeric K-Ras-GTP at low expression levels caused strong activation of Raf-MAPK equivalent to expressing K-Ras-GTP at physiological levels [46].

Mutations at a putative G-domain dimer interface inhibited Ras-Ras interaction, Ras-GTP induced Raf dimerization and signaling to Raf-MAPK in cells, as well as cell transformation *in vitro* and *in vivo* [86]. Intriguingly, at least in the case of K-Ras, neither the G-domain alone in solution nor the full length protein on artificial membranes were able to drive dimer (or cluster) formation at physiologically relevant concentrations, arguing for the requirement of scaffolding mechanisms on the membrane for efficient multimer formation. Among other mechanisms, previous experimental and computational investigations suggest that targeting to nanoscopic membrane compartments could be an effective means to promote Ras multimer formation. The membrane compartments could not only increase the local concentration of Ras by orders of magnitude but also bring in additional lipids (such as phosphotidylserine) or proteins (such as galectins) to further support Ras-Ras interactions.

With existing data strongly supporting a critical role of specialized membrane compartments in regulating the signaling activity and specificity of Ras, it is imperative to define the molecular and structural identities of the Ras-associated membrane compartments to fully elucidate how Ras operates on the membrane. Efforts to identify these membrane compartments have been met with severe technical challenges, primarily due to the complexity of biological membranes in composition, structure, and dynamics. The plasma membrane comprises hundreds of lipid, protein, and other species, and the membrane compartments could span length scales from nanometers to microns and time scales as short as milliseconds. Although immuno-EM has been routinely used for observing Ras nanoclusters, it is devoid of chemical specificity other than for the immuno-labeled target(s). In fact, Ras nanoclusters were first reported in 2001, but it was not until

~2014 that common lipids species such as phosphoinositol phosphates (PIPs) and phosphatidylserine (PS) were separately identified in the associated membrane domains [153]. The Ras nanocluster-associated membrane compartments have also never been directly visualized, perhaps because these compartments do not have a strong enough contrast under TEM. Potential connections between Ras nanoclusters with caveolae or the actin cytoskeleton were based on indirect evidence and using harsh perturbations. More recently, quantitative SRM based on single-molecule localization microscopy has been successfully used to visualize Ras dimers in cells. While SRM with 4+ colors have been demonstrated [154], it is still difficult to use SRM to directly analyze the molecular and structural identities of the Ras-associated membrane compartments without having a short list of imaging targets. In consequence, up until now there is little information available about the membrane compartments where Ras forms multimers and potentially also interacts with effectors.

For the complementary information afforded with SRM and EM, in the past five years there have been increasing efforts to combine SRM and various EM contrast mechanisms at both room and cryogenic temperatures for high-resolution imaging of biological targets. In particular, we and others have used correlative SRM and scanning EM (SEM) to investigate specific cellular targets (SRM) along with the ultrastructural details of the biological context. In our workflow, SRM is performed on hydrated samples, followed by SEM sample processing and imaging; this avoids loss of SRM signals typically associated with correlative SRM – EM workflows, which is critical for quantitative SRM. Compared with transmission EM (TEM, as commonly used for immuno-EM), SEM is both more convenient for samples on SRM-compatible substrates, such as prepared membrane sheets

on ITO-coated coverslips. With moderate staining and coating SEM also benefits from the rich contrast from various membrane-associated structures such as the cortical cytoskeleton that are more difficult to directly visualize in TEM. We reasoned that, by combining SRM with SEM, it may be possible to identify the Ras-associated membrane compartments along with the connected cortical cytoskeleton multimers based on their morphological features.

In the present work, we have combined quantitative SRM with SEM to visualize the spatial organization of Ras on the cell membrane along with the associated membrane ultrastructures. Here, SRM allows localization of single H- or K-Ras molecules tagged with PAmCherry1, a photoactivatable derivative of mCherry, on membrane sheets prepared on ITO-coated coverslips at ~20 nm spatial resolution. SEM imaging of the membrane sheets in the same field of view reveals both the cortical cytoskeleton, clathrin-coated pits (CCPs), and various vesicular structures. Using feature extraction algorithms, the various membrane ultrastructures could be identified in the SEM images, and the abundance of Ras within ~20 nm to each structure was quantitated in the overlaid, correlative SRM – SEM images, based on which the potential associations between H- or K-Ras and the ultrastructures were determined. Using single-molecule counting, we further analyzed Ras clustering on the membrane with respect to the nanoscale localizations and stoichiometry of the Ras clusters in the SRM images as well as their associations with specific membrane ultrastructures in the correlative SRM – SEM images. Lastly, we investigated whether Ras signaling is correlated with clustering in specific membrane compartments by quantitating the spatial organization of Ras and its relationship to the membrane ultrastructures under perturbations that disrupt the structures. Results from these imaging experiments and analyses clearly revealed an isoform-specific preference in the associations between Ras

clusters and the various membrane ultrastructures, which dictates not only the locations but also the stoichiometry of the Ras clusters. Additionally, the impact of disrupting subsets of the membrane ultrastructures on Ras signaling was also isoform-specific. Our work for the first time provided direct insight into the structural and compositional identities of the membrane compartments in which Ras clusters form and potentially interact with effectors. Given the importance of abnormal Ras signaling in cancer and the dependence of Ras activity on membrane organization, potential strategies for inhibiting mutant Ras by disrupting their spatial context could be developed.

3.2. Results

3.2.1. Correlative SRM and SEM enables nanoscopic imaging of Ras and membrane ultrastructures at once.

To visualize both Ras molecules and their associated membrane compartments, we prepared membrane sheets from cells expressing PAmCherry1 tagged tH, tK, H-Ras^{G12V}, and K-Ras^{G12D} mutants. Here tH and tK are the HVRs of H-Ras and K-Ras, which are responsible for trafficking and anchoring Ras to the plasma membrane. For the full length proteins, we focus on H-Ras^{G12V} and K-Ras^{G12D} because these mutants are constitutively active and useful for studying the impact of spatial organization on downstream signaling.

The membrane sheets were first imaged with SRM based on photoactivated localization microscopy (PALM) (Fig 3.1a). Despite ITO coating on the coverslips, we achieved 20-30 nm spatial resolution with SRM, which is comparable to previous results from cells grown on uncoated coverslips. The sample was subsequently processed with

moderate heavy metal staining, dehydration, drying and carbon coating for SEM imaging (Fig 3.1a). SRM and SEM imaging of the same membrane sheet was achieved by searching for the same markings on the substrate in the two modalities, and the resulting images were registered using 100 nm gold nanoparticles as previously described [114]. Zoom-in region of Fig 3.1b shows the precise registration between the SRM and the SEM images of the same membrane sheet (Fig 3.1b). From the registered images, localization of Ras molecules with membrane structures can be directly observed. For example, there is clear colocalization of H-Ras^{G12V} with large membrane vesicles at the membrane sheet, which showed as round and dark from SEM image (Fig 3.1b red arrows).

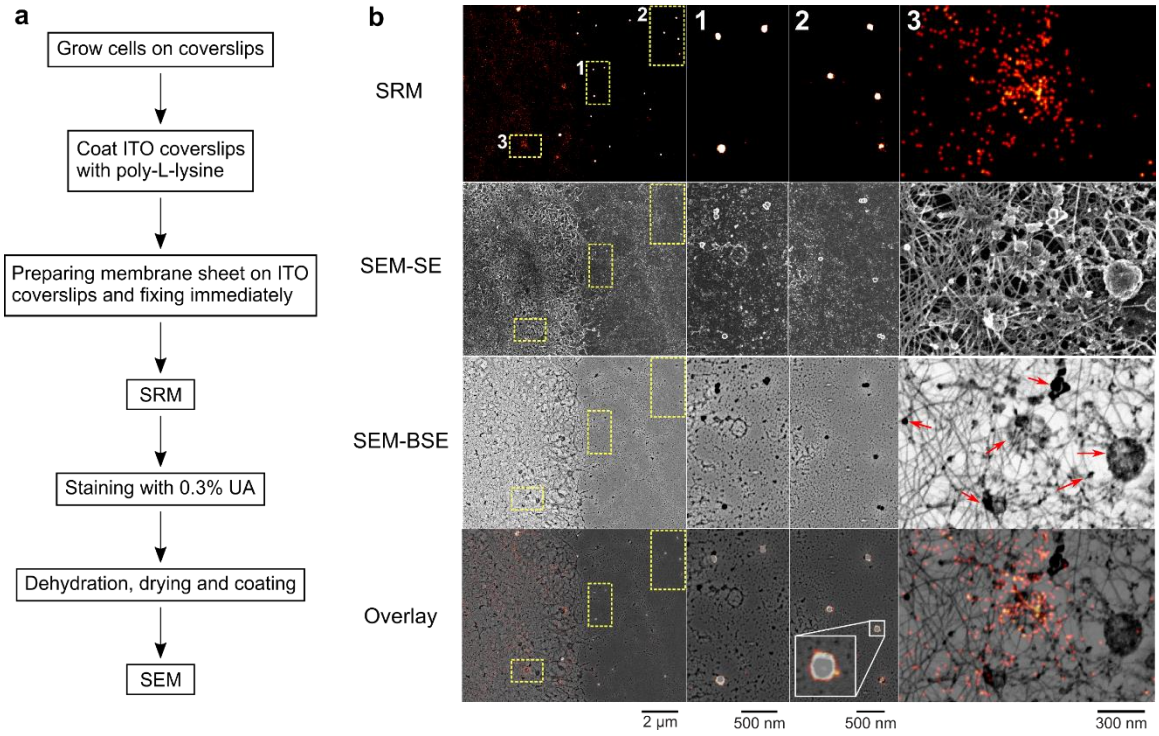

Figure 3.1 Correlative SRM and SEM imaging for visualizing Ras at membrane ultrastructures. (a) Workflow of correlative SRM and SEM imaging of prepared membrane sheets. (b) SRM, SEM-SE and SEM-BSE images taken from the same region of a membrane sheet. Gold nanoparticles (100 nm in size) appeared in both the SRM and the SEM images and were used for image registration.

In our correlative workflow, three imaging contrasts, fluorescence (FL), secondary electron (SE) and backscattered electron (BSE), of the same field of view were obtained. As SE and BSE images highlight structures from the top and bottom of the sample, combination of the two contrasts during SEM imaging offers more complete information of the membrane ultrastructures. In both SE and BSE images of prepared membrane sheets, a network of cortical filaments and various membrane vesicles on the inner leaflet are clearly resolved. To identify the filamentous network, we performed SRM imaging on the membrane sheet stained with phalloidin-Alexa Fluor 647 (Fig 3.2). At least a subset of the network overlapped well between the SRM and the SEM images. We therefore attribute the filaments observed in SEM images to cortical F-actin. During SRM imaging, we observed a constant dissociation of phalloidin from actin filaments, leading to an incomplete staining, which may account for the partial overlap.

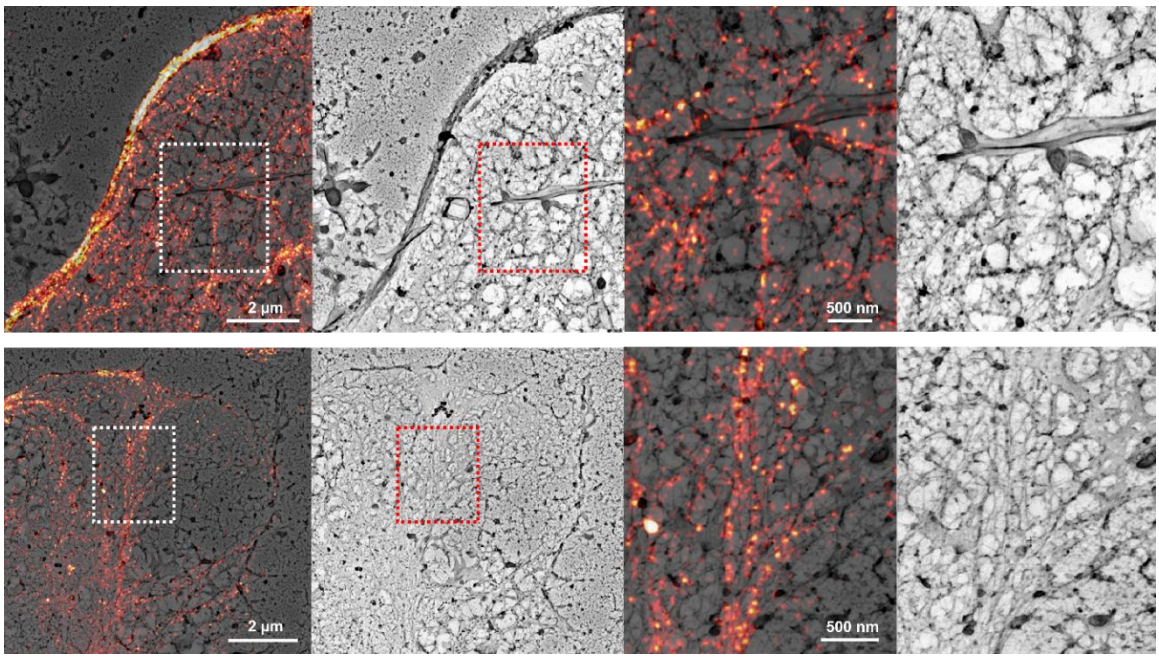

Figure 3.2 Correlative SRM and SEM imaging of actin at the membrane sheet

Visual inspection of the SEM images revealed the two main features: filaments and vesicles. Since the two features are distinct in morphology and dimension, we developed a simple computer algorithm for automated feature extraction. For this analysis, we typically use SEM-BSE images because of the cleaner background and better separation between the ultrastructural features than SEM-SE images. We first used intensity thresholding (Otsu's method [155]) to segment the SEM-BSE image into membrane vesicles (heavily stained) and filaments (lightly stained), followed by morphological operations (dilation and opening) to remove small objects and refine segmentation. This segmentation procedure is demonstrated in Fig 3.3a. In the segmented images (Fig 3.3a, third column), features in black represent membrane vesicles, and those in grey represent filaments.

Next, to quantitate the spatial distribution of Ras molecules relative to these structures, we calculated the distances from each Ras molecule to the segmented features. Ras molecules that were within 20 nm to (including those that overlap with) a feature are assigned to the feature. We chose 20 nm as the cutoff distance based on the localization uncertainty in SRM imaging. Of note, the same Ras molecule may be assigned to multiple features if the calculated distances were all within 20 nm; conversely, a Ras molecule may be omitted if none of the distances were within 20 nm. As demonstrated in Fig 3.3b, the green dots are Ras molecules proximal to the vesicles, the red dots are those assigned to filaments, and the yellow dots are those assigned to both features.

After assigning each molecule to the segmented features, we were able to calculate the fraction of Ras molecules localized to either the cortical cytoskeleton or the membrane vesicles. Overall, we observed a much higher fraction of Ras molecules proximal to the cortical cytoskeleton than to the membrane vesicles. This is mostly attributed to relative

abundance between the two features, i.e., the density of the cortical cytoskeleton is much higher than that of the membrane vesicles. Therefore, for each correlative image, we always generate ~100 simulated datasets with randomly distributed Ras molecules at the measured molecule density overlaid on the same SEM image. These simulated datasets are analyzed the same way as experimental images to obtain the mean and the standard deviation of the fraction of Ras molecules on either feature as expected from a random distribution. Results from the experimental and the simulated datasets were then compared to determine whether Ras preferentially localizes to either membrane feature.

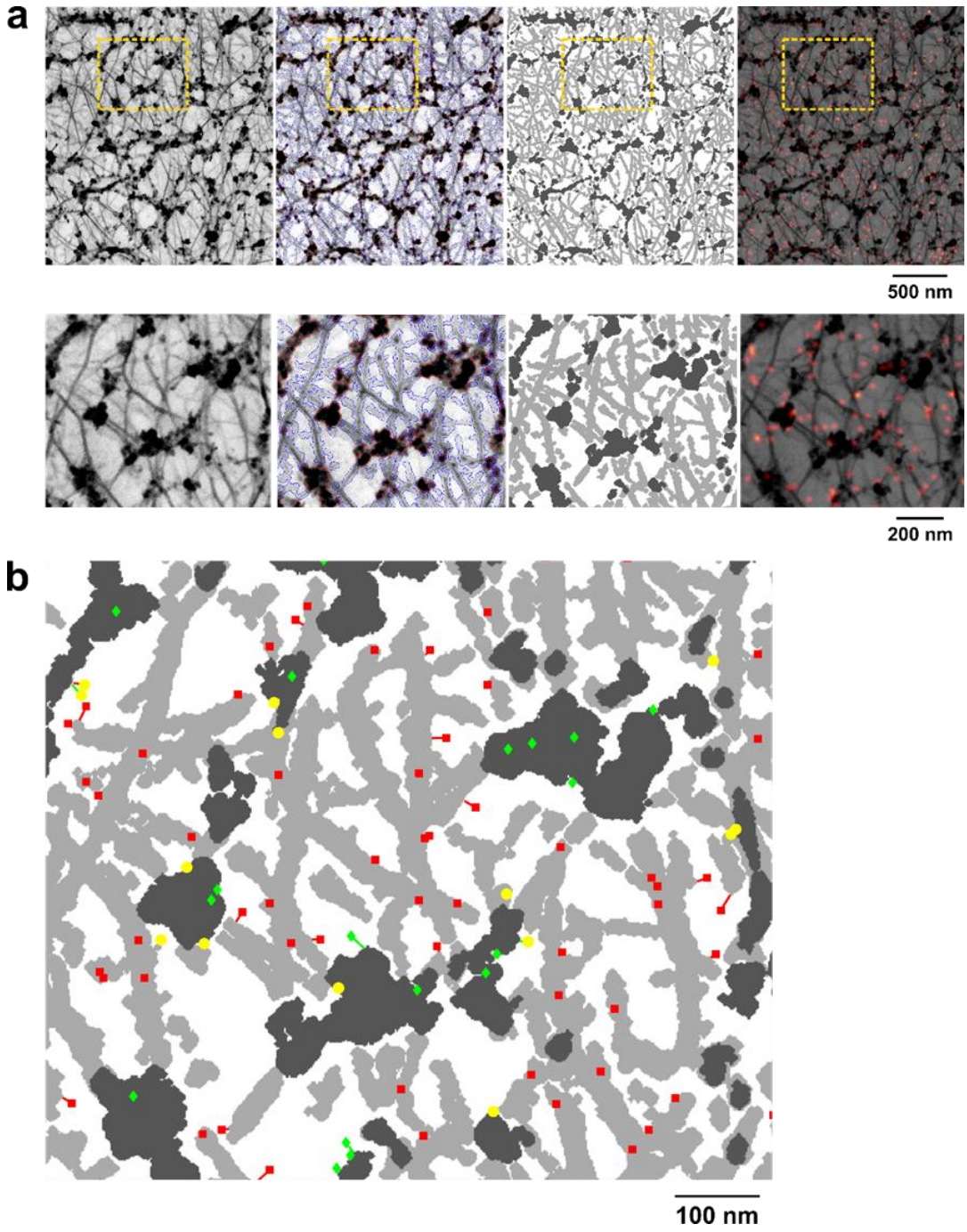

Figure 3.3 Statistical analysis of Ras association with the membrane ultrastructures. (a) Segmentation of vesicles and filaments of SEM image. Images are membrane of U2OS cells expressing PAmCherry1-tK. Features in black represents vesicles and features in grey represents filaments. Ras localization determined by SRM was then used to analyze their proximity to these segmented structures. (b) Proximity quantification of Ras molecules to the membrane structures. Green dot represents Ras molecules within 20 nm distance to vesicles, red dot represents Ras molecules within 20 nm distance to membrane filaments, and the yellow dots are those proximal both features.

3.2.2. tH and H-Ras^{G12V} preferentially localize to membrane vesicles and clathrin-caoted pits

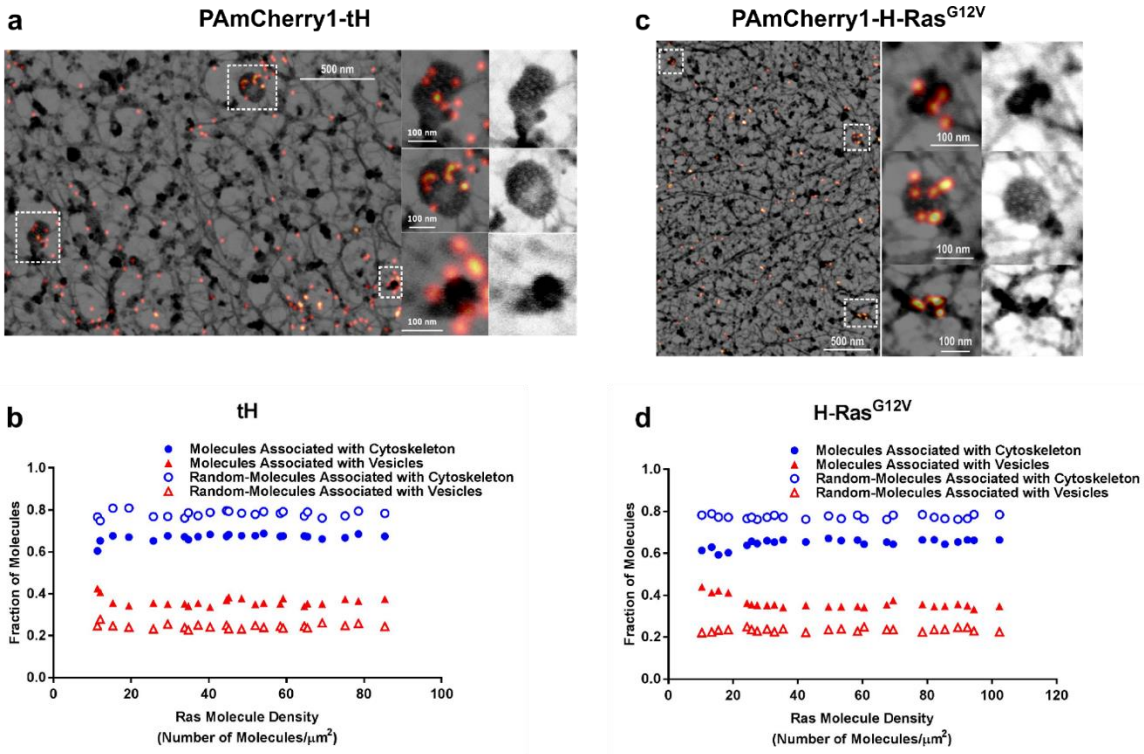

Figure 3.4 Preferential localization of tH and H-Ras^{G12V} to membrane vesicles and CCPs. (a) Correlative SRM and SEM images showed strong preference of tH localization of membrane vesicles and CCPs. (b) Quantitative analysis of proximity of tH to membrane vesicles and filament network at tH densities from ~10 to ~90 molecules/μm^2. (c) Correlative SRM and SEM imaging of H-Ras^{G12V} showed its high localization preference to membrane vesicles and CCPs. (d) Quantitative analysis of proximity of H-Ras^{G12V} to membrane vesicles and filament network at H-Ras^{G12V} densities ranging from ~10 to ~100 molecules/μm^2.

Quantitative analysis of the correlative images from membrane sheets expressing PAmCherry1-tH or full length H-Ras^{G12V} revealed a slight but significant preference of both tH and H-Ras^{G12V} localizing to membrane vesicles and CCPs. This preferred localization is first evident from visual inspection of the images (Figs 3.4a and c) and is clearly demonstrated in the quantification results (Figs 3.4b and d). For tH, the fractions of

molecules proximal to vesicles and to filaments were typically around 36% and 67%, respectively, and the fractions from random datasets were 26% and 78%, respectively. Of note, the sum of the two fractions in both datasets was greater than 100% because some molecules were assigned to both structures. In other words, the fraction of tH associated with membrane vesicles is about 10% higher than random distributions; by contrast, the fraction of tH next to the cortical cytoskeleton is about 11% lower than random. These numbers are almost identical to those of full length H-Ras^{G12V}, indicating a similar partitioning of H-Ras-GTP to that of tH between the cortical filaments and the membrane vesicles.

The preferred localization of both tH and H-Ras^{G12V} to membrane vesicles was observed across a wide range of expression levels. With single-molecule counting based on the SRM images, we determined that the membrane sheets expressed tH or H-Ras^{G12V} at molecular densities ranging from ~10 to ~100 molecules/μm^2, which allowed us to investigate how the localization of tH and H-Ras^{G12V} may change with the expression level. As shown in Figs 3.4b and d, the difference between experimental and simulated data remained almost constant across all molecular densities above 20 molecule/μm^2. Interestingly, at very low molecular densities (10-20 molecules/μm^2), both tH and H-Ras^{G12V} showed a stronger preference to membrane vesicles.

3.2.3. tK and K-Ras^{G12D} preferentially localizes to the vicinity of cortical cytoskeleton

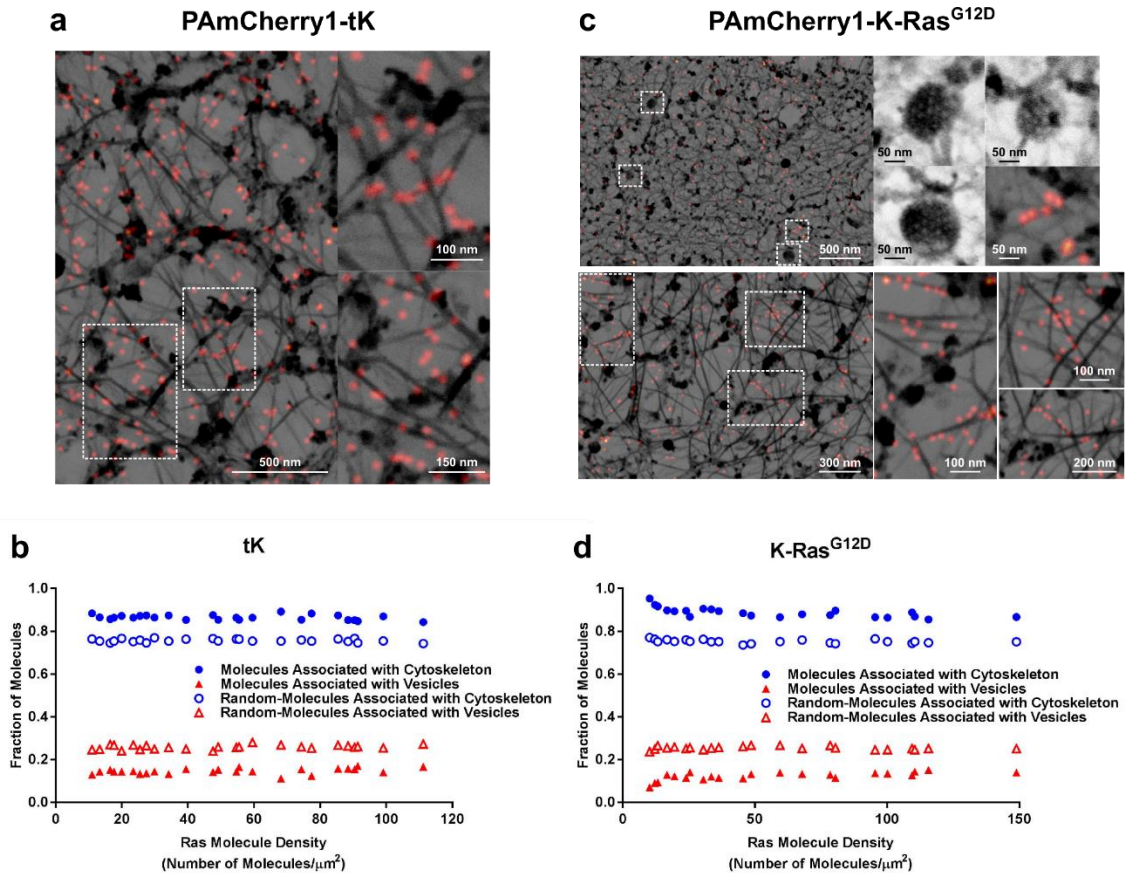

Figure 3.5 Preferential localization of tK and K-Ras^{G12D} to the vicinity of cortical cytoskeleton. (a) Correlative SRM and SEM images showed tK localizing to vicinity of cortical actin network. (b) Quantitative analysis of proximity of tK to membrane vesicles and filamentous network at tK densities from ~10 to ~110 molecules/μm^2. (c) Correlative SRM and SEM imaging of K-Ras^{G12D} showed its localization is excluded from vesicles and CCPs. Instead, localization of K-Ras^{G12D} showed high preference to filamentous network. (d) Quantitative analysis of proximity of K-Ras^{G12D} to membrane vesicles and filament network at molecule densities ranging from ~10 to ~150 molecules/μm^2.

While the abundance and arrangement of the vesicles and filaments are similar between tK/K-Ras^{G12D} and tH/H-Ras^{G12V} expressing membrane sheets, the spatial

distributions of tK and K-Ras^{G12D} are clearly different from tH and H-Ras^{G12V}. Specifically, most tK and K-Ras^{G12D} molecules are localized to membrane regions next to the cortical cytoskeleton. At high expression levels, many tK and K-Ras^{G12D} molecules even tracked the cortical filaments (Fig 3.5a). Only a minor fraction of tK or K-Ras^{G12D} molecules were observed on or next to membrane vesicles. Moreover, both tK and K-Ras^{G12D} were essentially excluded from the CCPs (Fig 3.5c). Using the same quantitative analysis described above, we found that the fractions of tK proximal to the vesicles and to the filaments are typically around 17% and 87%, respectively; those from simulated random datasets are 25% and 78%, respectively. Hence, the fraction of tK associated with the cortical cytoskeleton is about 9% higher than random distribution. The spatial distribution of K-Ras^{G12D} is almost identical to that of tK. About 15% and 88% of K-Ras^{G12D} molecules are proximal to membrane vesicles and filaments respectively, while the fractions from random datasets are about 26% and 77% respectively. Similar to the case of tH and H-Ras^{G12V}, the same pattern holds across a wide range of expression level of about 10-150 molecules/um^2. Interestingly, at low molecule densities (below 20 molecules/μm^2), K-Ras^{G12D} showed a stronger preference to the cortical filaments than at higher molecular densities, which was not observed for tK.

3.2.4. H-Ras and K-Ras multimers differ in location, density, and size.

Recent evidence suggests that Ras multimers, such as clusters and dimers, may be the active signaling units of Ras [156]. In all four cases (tH, H-Ras^{G12V}, tK, and K-Ras^{G12D}), formation of multimers was evident in the SRM images. To investigate the association between Ras multimers with either membrane compartment, we analyzed the location and the size of H-Ras^{G12V} and K-Ras^{G12D} multimers. Multimer identification and size

calculation were performed using simulation-aided DBSCAN [156] as described previously, which defines spatial clustering of point patterns based on variations in local molecular densities. After defining the multimers and the monomers, the spatial locations of each species relative to either membrane feature were analyzed as described for the whole population. This allows us to determine which type of membrane compartment is associated with H-Ras^{G12V} or K-Ras^{G12D} multimers in comparison with their respective monomers.

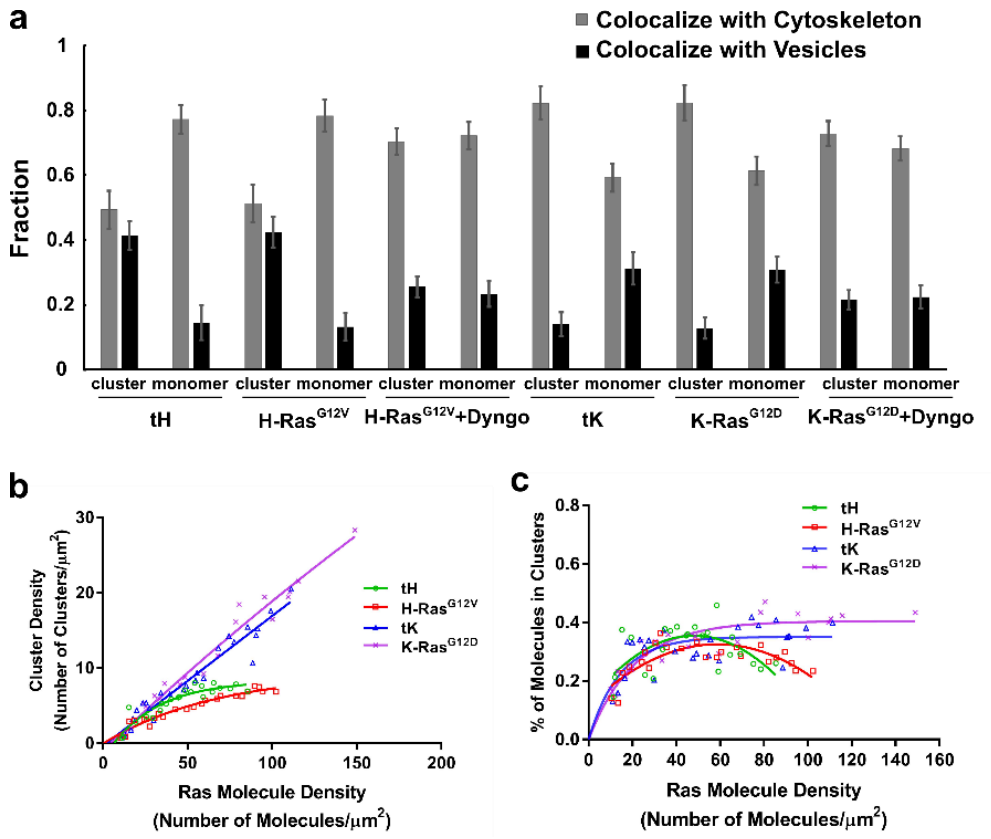

Figure 3.6 H- and K-Ras clusters differ in their membrane localization and cluster density. (a) Localization of H- and K-Ras clusters and monomers to filaments or vesicles. (b) Relationship between Ras cluster density and Ras molecule density. The Densities of both tH and H-Ras^{G12V} clusters reached a plateau beyond 60 molecules/μm^2, while those of tK and K-Ras^{G12D} clusters kept increasing linearly with Ras molecule density up to 150 molecules/μm^2. (c) Relationship between fraction of Ras molecules forming clusters and Ras molecule density.

We found that in all cases, the Ras multimers showed even stronger preference to a membrane compartment than the corresponding monomers. For tH and H-Ras^{G12V}, approximately 52% of the multimers colocalize with the membrane vesicles, compared with approximately 15% for the monomers. For tK and K-Ras^{G12D}, the multimers are predominantly (>82%) found at the cortical cytoskeleton. In comparison, only ~60% of the monomers are localizing to the filaments (Fig 3.6a). From Figs 3.4 and 3.5, we anticipated ~25% and ~75% of randomly distributed Ras species (multimers or monomers) to be located in proximity to the vesicles and the cortical cytoskeleton, respectively. Thus, we concluded that whereas the Ras monomers roughly follow a random distribution on the membrane, the Ras multimers have a strong preference for either membrane compartment, with H-Ras^{G12V} multimers preferring the membrane vesicles and K-Ras^{G12D} the cortical cytoskeleton.

Interestingly, multimers of H-Ras^{G12V} and K-Ras^{G12D} also differ in density and size, which refer to the number of multimers per unit area and the number of Ras molecules per multimer, respectively. The densities of both tH and H-Ras^{G12V} multimers reached a plateau beyond 60 molecules/μm^2, while those of tK and K-Ras^{G12D} multimers kept increasing linearly at a Ras density of up to 150 molecules/μm^2 (Fig 3.6b), which is the highest density measured in our experiments. For tH and H-Ras^{G12V}, the percentage of molecules forming clusters was increasing from 10% to ~38% within the molecule density at 10-60 molecules/μm^2. After it peaked at ~38%, the fraction gradually decreased to ~25% as molecules density continued to increase up to ~100 molecules/μm^2. Similar increasing trend was observed with tK and K-Ras^{G12D} within the density at 10-80 molecules/μm^2. But the fraction stays constant at ~40% beyond 80 molecules/μm^2 (Fig 3.6c).

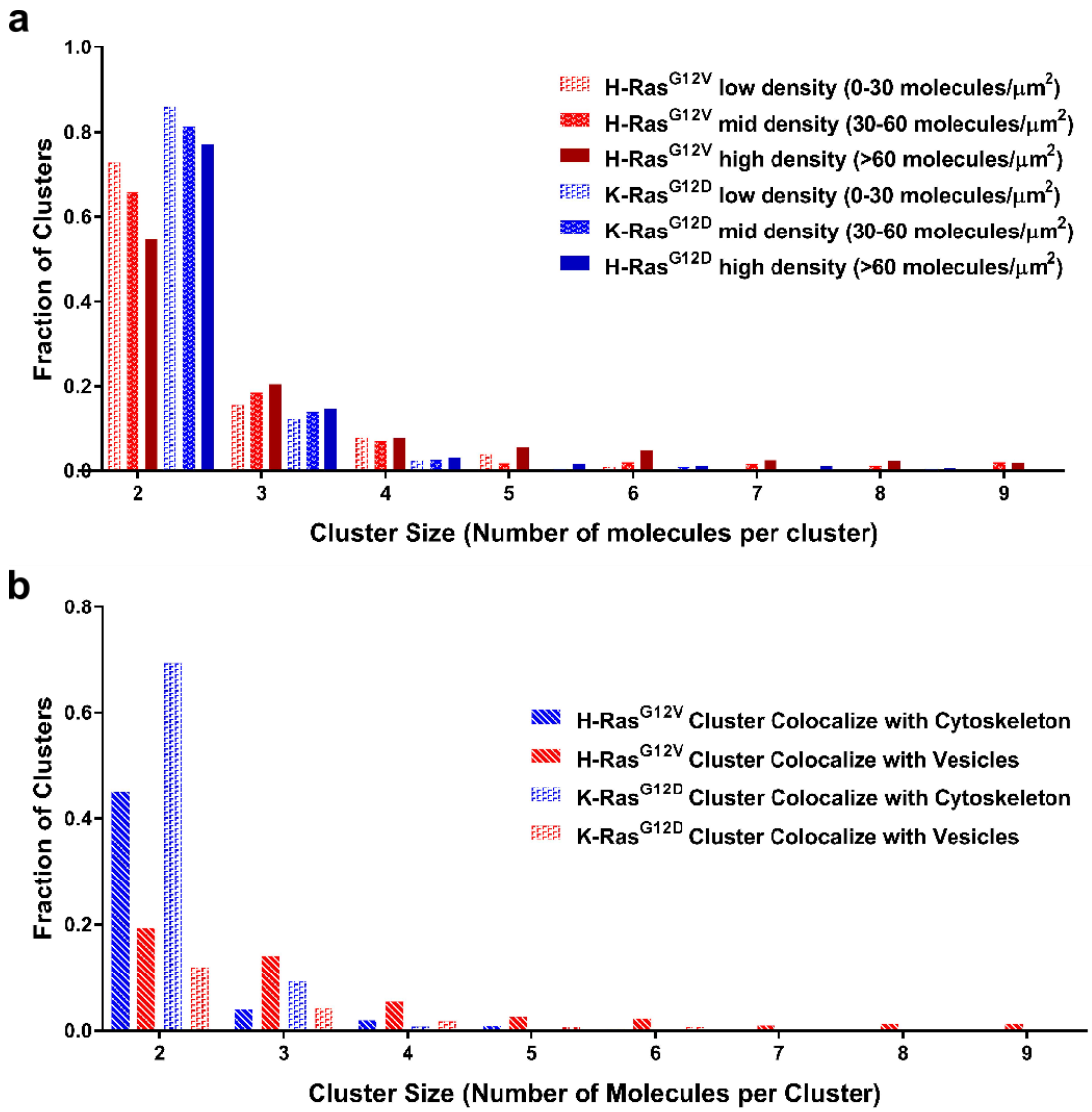

Figure 3.7 H- and K-Ras clusters differ in their cluster size. (a) Size distribution of H-Ras^{G12V} and K-Ras^{G12D} clusters at different molecule densities. H-Ras^{G12V} had higher percentage of large clusters (>2) while K-Ras predominantly formed dimers. (b) Size distributions of H-Ras^{G12V} and K-Ras^{G12D} clusters in either vesicles or cytoskeleton.

We also observed that H-Ras^{G12V} has a significantly higher fraction of large (>2 Ras molecules) multimers than K-Ras^{G12D} at all Ras molecular densities (Figs 3.7a). As the density of Ras molecules increases, H-Ras^{G12V} multimers became larger in size but the multimer density plateaued at 6-7 per um^2. By contrast, K-Ras^{G12D} predominantly remains

dimeric even at high molecular densities. These results suggest that H-Ras^{G12V} tends to form larger multimers in membrane vesicles and K-Ras^{G12D} tends to make dimers in compartments related to cortical filaments, indicating that potentially different mechanisms drive the multimer formation of Ras in the two membrane compartments.

3.2.5. Ras dimers predominantly localize to the cortical cytoskeleton, and larger multimers to the vesicles

Since H-Ras^{G12V} and K-Ras^{G12D} preferentially form multimers at the membrane vesicles and the cortical cytoskeleton, and the two Ras isoform predominantly forms dimers and mixed dimers and larger multimers, we asked whether the size of Ras multimers has a direct relationship with the associated membrane compartment. To address this question, we analyzed the multimer size distributions of both H-Ras^{G12V} and K-Ras^{G12D} in either membrane compartment. As shown in Fig 3.7b, both H-Ras^{G12V} and K-Ras^{G12D} dimers are predominantly associated with the cortical cytoskeleton. The fractions of H-Ras^{G12V} dimers associated with the membrane vesicles and the cortical cytoskeleton are 19% and 45%, respectively. For K-Ras^{G12D}, the fractions of dimers associated with the membrane vesicles and the cortical cytoskeleton are 11% and 69%, respectively.

By contrast, we found that larger Ras multimers (3-mer and up) are predominantly on membrane vesicles. For H-Ras^{G12V}, 36% of the multimers are the trimers and up; when separated by membrane compartments, ~28% and ~7% out of the 36% multimers are associated with the membrane vesicles and the cortical cytoskeleton, respectively. For K-Ras^{G12D}, 19% of the total multimers are the larger ones, out of which ~12% and ~7% are associated with the membrane vesicles and the cortical cytoskeleton, respectively.

Based on this analysis, we conclude that both H-Ras and K-Ras predominantly forms dimers in the cortical cytoskeleton-associated membrane compartment, and the vast majority of larger Ras multimers are formed in the membrane vesicles. Thus, it appears that the membrane compartment dictates the size of Ras multimers regardless of the isoform, indicating that the two types of the membrane compartments may drive Ras multimer formation through different mechanisms.

3.2.6. Ras cluster-associated membrane vesicles are dynamin-dependent endocytic precursors

Currently, the identities of the membrane vesicles associated with Ras multimers are unknown. Since some H-Ras^{G12V} multimers were found on the CCPs, we asked whether eliminating the CCPs, for example through inhibition of dynamin, would cause H-Ras^{G12V} to redistribute to other membrane compartments. For this purpose, we used Dyngo 4a, a potent dynamin inhibitor that blocks the scission of newly formed CCPs. To our surprise, treating U2OS cells with Dyngo 4a caused a massive loss of all the heavily stained membrane vesicles and not just the CCPs (Fig 3.8a). Indeed, previous reports suggested that several endocytic precursors including CCPs, caveolae, and RhoA-dependent endocytic vesicles, all depend on dynamin [157]. An increased membrane localization of both H-Ras^{G12V} and K-Ras^{G12D} was observed with Dyngo treatment (Fig 3.8b), indicating that dynamin inhibition leads to accumulation of both H-Ras^{G12V} and K-Ras^{G12D} at the cell membrane. Therefore, at least a subset of these dynamin-dependent vesicles is responsible for endocytic trafficking of both Ras isoforms.

3.2.7. Raf activation by H- and K-Ras has differential dependence on the multimer compartments

With insight into the two compartments where Ras forms multimers, we next sought to understand how the two compartments regulate Ras signaling. With Dyngo 4a treatment, the membrane vesicles were eliminated, leading to an accumulation and spatial redistribution of both H-Ras^{G12V} and K-Ras^{G12D} at the membrane (Fig 3.8b). In treated cells, only ~20% of H-Ras^{G12V} or K-Ras^{G12D} molecules were associated with residual vesicles, which is comparable with random distribution (Figs 3.8f and g). In addition, Dyngo 4a treatment also decreased the preference of H-Ras^{G12V} multimers to membrane vesicles. H-Ras^{G12V} still forms multimers, but only about 25% of H-Ras^{G12V} multimers were colocalized with the membrane vesicles (Fig 3.6a), which is 17% lower than the control; by contrast, 70% of H-Ras^{G12V} clusters are now located next to the cortical cytoskeleton. For K-Ras^{G12D}, about 21% of the multimers were associated with membrane vesicles after Dyngo 4a treatment, which is 9% higher than control (Fig 3.6a).

Next, we examined if the redistribution of H-Ras^{G12V} at the cell membrane affects its downstream signaling. We focused on the Raf-MAPK pathway using ppErk (dually phosphorylated Erk) as the readout, since previous studies on Ras multimers (including dimers) clearly indicated a role of these structures in Raf-MAPK activation. We observed that both H-Ras^{G12V} and K-Ras^{G12D} accumulated at the cell membrane with Dyngo 4a treatment, but the impacts on Raf-MAPK signaling output were opposite between the two Ras isoforms. Downstream ppERK signal of H-Ras^{G12V} decreased as a result (Fig 3.8d). In contrast, downstream signal of K-Ras^{G12D} was amplified with increased K-Ras level (Fig 3.8e).

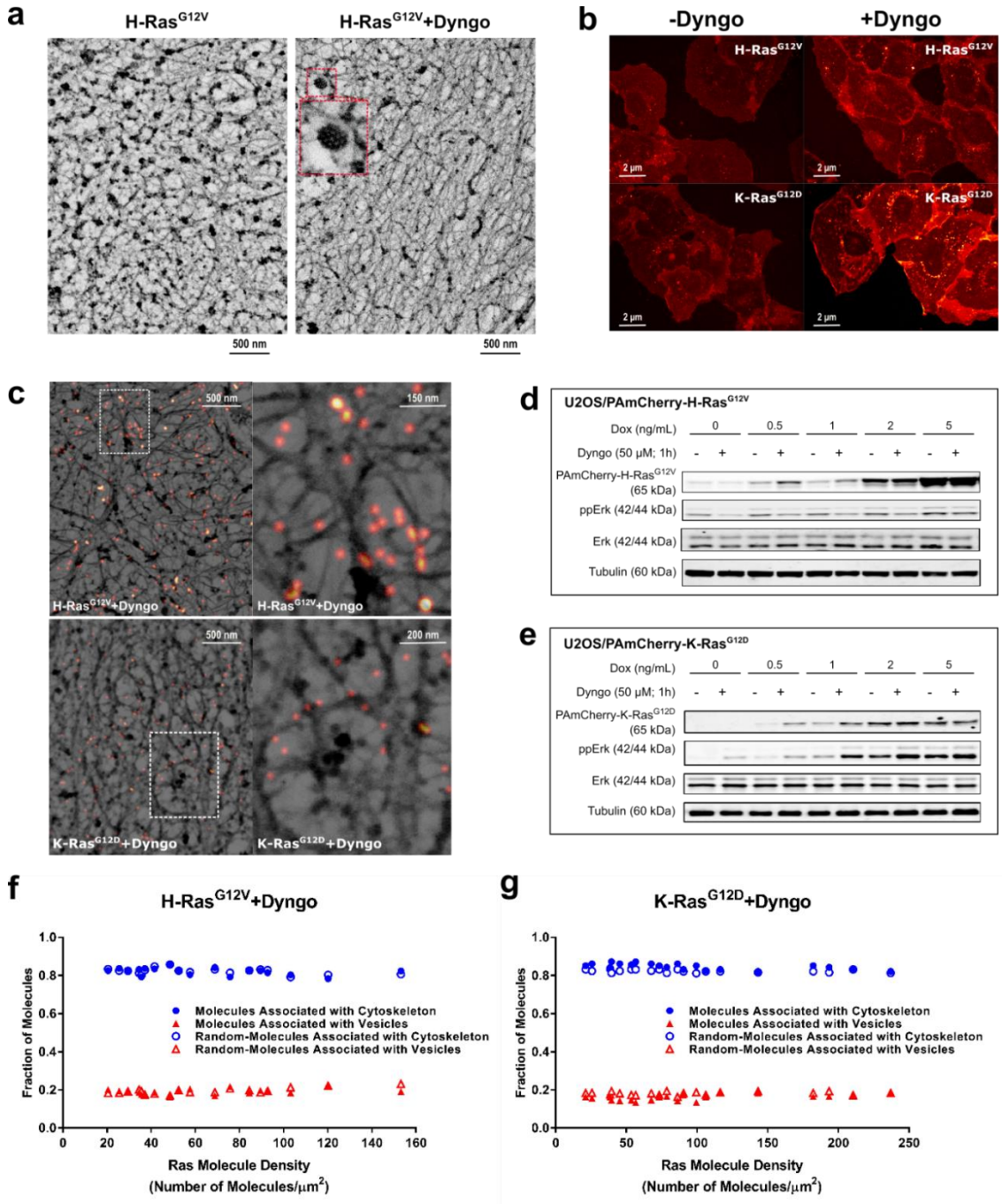

Figure 3.8 Redistribution of H- and K-Ras at the cell membrane by Dyngo 4a treatment leads to differential isoform-specific signaling outputs. (a) SEM-BSE images of membrane sheets with or without Dyngo treatment. An obvious decrease of membrane vesicles and CCPs was observed with the treatment. (b) Confocal florescence images of U2OS cells with or without Dyngo treatment. Both H-Ras^{G12V} and K-Ras^{G12D} were accumulated at the cell membrane after Dyngo treatment. (c) Correlative SRM and SEM images showed redistribution of both H-Ras^{G12V} and K-Ras^{G12D} at the cell membrane. (d)

Western blotting demonstrating the effect of Dyngo treatment on Raf-MAPK (as indicated by ppErk) activation in U2OS cells expressing PAmCherry1-H-Ras^{G12V}. (e) Western blotting demonstrating the effect of Dyngo treatment on Raf-MAPK activation in U2OS cells expressing PAmCherry1-K-Ras^{G12D}. (f) Quantitative analysis of proximity of H-Ras^{G12V} to membrane vesicles and filament network with Dyngo treatment. (g) Quantitative analysis of proximity of K-Ras^{G12D} to membrane vesicles and filament network with Dyngo treatment.

We also examined whether disruption of the cortical cytoskeleton would affect Ras membrane localization and downstream signaling. To this end, we treated the cells with cytochalasin-D (1 uM) for 30 minutes. Cytochalasin D blocks actin polymerization and filament elongation [158]. When examined using SEM, membrane sheets from cells treated with cytochalasin-D showed loosened actin bundles of ~2 μm wide in comparison with the untreated membrane sheets, where the bundles were much tighter (~200 to 500 nm wide) and straight (Fig 3.9a). However, this treatment did not dissolve filaments and had limited effect on disrupting the finer cortical cytoskeleton network. The meshwork of thinner (typically <50 nm) cortical filaments apparently survived cytochalasin D treatment (Fig 3.9a). Using western blotting, we also did not observe a significant effect on H-Ras or K-Ras mediated Raf-MAPK activation from cytochalasin-D treatment (Figs 3.9b and c). Other actin polymerization inhibitors such as latrunculin-A was too hash to the cells to allow reliable membrane sheet preparation and thus were not pursued further.

These results confirmed the differential effects of the two membrane compartments, particularly the membrane vesicles, on the spatial organization and signaling of H-Ras and K-Ras. The formation of membrane vesicles, including CCPs are important membrane ultrastructure that organizes H-Ras^{G12V} clusters and facilitates their downstream signaling.

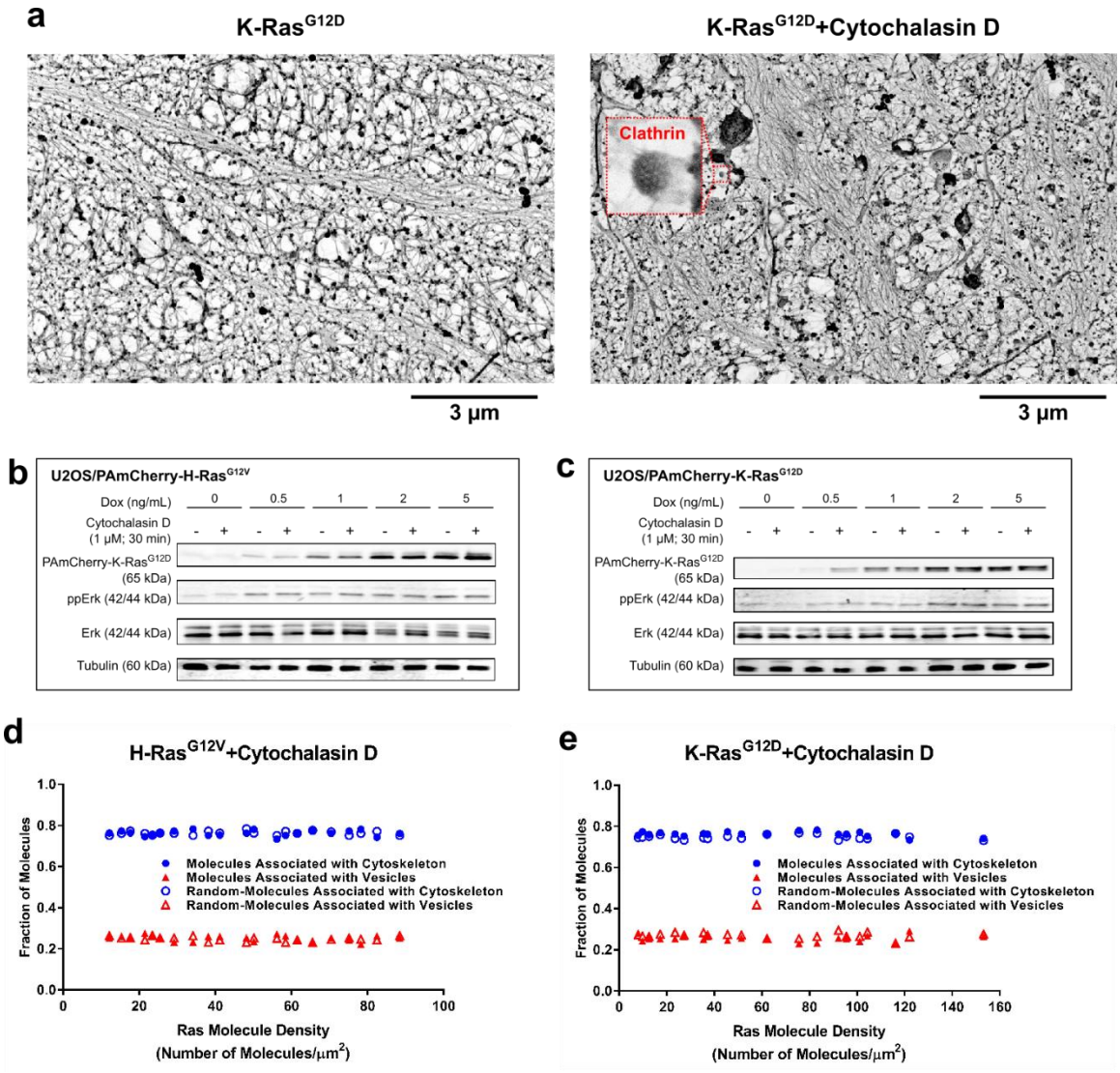

Figure 3.9 Effect of cytochalasin D treatment on cortical actin network and Ras distribution at the cell membrane. (a) SEM images of membrane sheet with or without cytochalasin D treatment. (b) Western blotting demonstrating the effect of Cytochalasin D treatment on Raf-MAPK activation in U2OS cells expressing PAmCherry1-H-Ras^{G12V}. (c) Western blotting demonstrating the effect of Cytochalasin D treatment on Raf-MAPK activation in U2OS cells expressing PAmCherry1-K-Ras^{G12D}. (d) Quantitative analysis of proximity of H-Ras^{G12V} to membrane vesicles and filament network with Cytochalasin D treatment. (e) Quantitative analysis of proximity of K-Ras^{G12D} to membrane vesicles and filament network with Cytochalasin D treatment.

3.3. Discussion

Despite strong evidence that different Ras isoforms are spatially segregated into different membrane compartments, the molecular and structural identities of the membrane compartments have mostly been indirectly inferred. We have used correlative SRM and SEM to investigate how Ras signaling in cells is spatially regulated by specialized membrane compartments. By taking advantage of the complementary information offered through SRM and SEM, we were able to directly visualize and identify the various membrane compartments associated with multimers of H-Ras or K-Ras. We further show that the membrane compartments had a major influence on how the Ras proteins form multimers regardless of the isoform. Lastly, we provide direct evidence that Ras isoform needs to be in the correct membrane compartment to activate its effectors. These results highlight the critical importance of the membrane, and in particular the heterogeneous membrane compartments, in governing the biological activities of Ras in cells.

Through quantitative analysis of the correlative SRM-SEM images, we were able to directly visualize and identify the membrane ultrastructures associated with the different multimeric states of each Ras isoform. When counting the whole population, H-Ras and K-Ras have a weak preference over the membrane vesicles and the cortical cytoskeleton. When separated by multimeric states, it became apparent that monomers of H-Ras and K-Ras are essentially randomly distributed across the membrane and that it is the multimers that are associated with specific compartments with a strong preference. For H-Ras^{G12V}, its multimers are found more often in various membrane vesicles (including CCPs), and this localization appears to be driven by its HVR, because tH showed almost identical partitioning between the two compartments. For K-Ras^{G12D}, the multimers are

predominantly associated with the cortical cytoskeleton, and the localization is also apparently driven by its HVR. Based on the same reasoning, it is likely that the G-domain of either Ras isoform did not play a major role in driving multimer localization. Hence, we expect the multimers of wild type Ras (GDP) to also follow a partitioning pattern between the two compartments to the corresponding Ras-GTP and HVR. That said, the exact nature of the compartments to which each of the Ras constructs (HVR, Ras-GDP, and Ras-GTP) localizes may still be different. After all, our current, simple classification of all vesicles or all membrane regions linked to the cortical actin to a single type may not be adequate.

A major finding from our work is that most, if not all, of the membrane vesicles associated with H-Ras are dynamin-dependent. These vesicles are likely endocytic precursors, and at least a subset of these is responsible for endocytic trafficking and subsequent turnover of H-Ras, because elimination of these vesicles through dynamin inhibition increased overall Ras protein level as well as the membrane localization of H-Ras. The treatment displaced H-Ras from the vesicles, after which H-Ras formed dimers proximal to the cortical cytoskeleton; surprisingly, these H-Ras multimers were not able to activate Raf-MAPK, underscoring the importance of these dynamin-dependent vesicles to H-Ras signaling activity. Additionally, this observation also indicates that, while H-Ras can form multimers in the cortical cytoskeleton membrane compartment, those H-Ras multimers may not be able to activate Raf-MAPK. By contrast, although K-Ras multimers were also found in small numbers on the same type of vesicles, eliminating these vesicles enhanced K-Ras activation of Raf-MAPK. This is likely because K-Ras signaling relies on the multimers at the cortical cytoskeleton sites, where the most K-Ras multimers reside. This is consistent with previous reports that the actin cytoskeleton seems to be involved in

K-Ras nanocluster formation, although no direct colocalization between actin filaments and K-Ras nanoclusters have been observed prior to our work. Thus, H-Ras and K-Ras not only form multimers in distinct types of membrane compartments, but also depend on their respective multimer compartments for signaling.

Dynamin has been implicated in several endocytic pathways, including CCP, caveolae, and RhoA-dependent endocytosis. While the differential role of endocytosis in signaling of H- and K-Ras have been examined before, previous studies point to clathrin-independent mechanisms for Ras signaling [159]. Our imaging results provide direct evidence that the CCPs, or clathrin-dependent endocytosis, may also be involved in multimer formation and signaling at least in the case of H-Ras. Of note, K-Ras is essentially excluded from the CCPs. Clathrin-mediated endocytosis, as a major endocytic pathway, has been shown to play an essential role for sustained EGFR signaling [160]. CCPs enhances the EGFR signaling by recycling the molecules to the membrane and thereby prolongs the duration of signaling. The role of CCPs in H-Ras signaling needs to be further investigated. One possible explanation for H-Ras localization to CCPs is that H-Ras, as a downstream signaling molecule of EGFR, is recruited to the CCPs as part of the EGFR signaling complex.

Aside from CCPs, we also observed localization of H-Ras multimers on unknown membrane vesicles that were typically 100 -150 nm in diameter and also seem to attach to the cortical cytoskeleton. These characteristics are consistent with caveolae and RhoA-dependent endocytic vesicles, which are typically in the ~100 nm size range and also involve actin in their biogenesis and invagination, but the identities of these small vesicles still need to be accurately defined. Work along this line is currently underway. We note

that, dynamin inhibitors such as Dynasore were shown to have side effects such as depletion of membrane cholesterol [157], thereby offering an alternative explanation to the observed loss of vesicles if the latter depend on cholesterol. It is unclear whether Dyngo 4a has the same effect on cholesterol; in all of our Dyngo 4a treatments, we did not observe increased cell rounding or other apparent adverse effects (Figs 3.6a and b) as seen in cholesterol depletion experiments using cyclodextrins (data not shown). Thus, it is possible that Dyngo 4a does not impact membrane cholesterol as Dynasore. Even if it does, it would have directly eliminated caveolae, among other vesicles, which were also dynamin-dependent. Therefore, the general conclusion that H-Ras multimers are associated with dynamin-dependent vesicles should remain valid.

Our work also provides evidence for the use of 'scaffold' mechanisms to facilitate Ras multimer formation, at least in the cases of H-Ras and K-Ras. Recently, there have been efforts to reconstitute Ras multimers on artificial membranes, using synthetic or native membrane linkers. For H-Ras, while it was originally reported that dimers were detected in a concentration (density) dependent manner on supported lipid bilayers [84], the observation was later shown to be an artifact due to photo-induced oxidation of Tyr 64 [85]. For K-Ras, the proteins were not able to dimerize over a wide range of concentrations or lipid compositions, even when phosphatidylserine was included. Thus, it appears that merely attaching Ras to the membrane is not sufficient to drive multimer formation. In single particle tracking (SPT) experiments, both H-Ras and K-Ras have been found to make transient 'stops' at the membrane, which were hypothesized to be regions, or scaffolds, on the membrane that mediate multimer formation [77].

Among other scaffolding mechanisms, localization to specialized, nanoscopic compartments such as the nanoscopic membrane vesicles, may offer an effective means to promote Ras multimer formation. Thus, for H-Ras, the scaffolds for multimer formation are offered in part through localization to dynamin-dependent endocytic vesicles. When all available vesicular compartments are occupied, no more H-Ras multimers would form. Instead, the H-Ras multimers could simply become larger, thus explaining why H-Ras multimer density reaches a plateau at high molecular densities. Our results also suggest that more than two Ras molecules can target to the endocytic vesicles to give rise to larger multimers (3-mers and up), which holds true for both H-Ras and K-Ras. We note that, compared to H-Ras, K-Ras only has a minor fraction targeted to the endocytic vesicles, in good agreement with the well-known fact that H-Ras has more active cycling between the plasma membrane and the cytoplasm than K-Ras [159].

Parallel to this passive targeting to membrane structures, recently there has been increasing evidence to support an active mechanism that drive protein multimer formation through dynamic polymerization and contraction of cortical actin filaments [161]. In this mechanism, a small 'aster' of polymerizing actin filaments pushes membrane proteins to form transient nanoclusters. Even classical 'lipid raft' markers such as GPI-anchored proteins were found to form membrane nanoclusters through this mechanism. In the present work, we found that K-Ras multimers predominantly form in membrane regions linked to the cortical cytoskeleton, raising the possibility that K-Ras multimers may form through this active mechanism. This hypothesis is supported by two pieces of evidence. First, multimers found at the cortical cytoskeleton sites were predominantly dimers for both K-Ras and H-Ras, suggesting a non-HVR driven multimer formation mechanism distinct

from that facilitated through targeting to endocytic vesicles. Second, the anionic lipid phosphatidylserine is implicated in the actin-driven mechanism, which has also been strongly implicated in K-Ras nanocluster formation in a few recent studies [82].

Currently, it remains unclear how K-Ras connects to the cortical cytoskeleton. Unlike other Ras isoforms, K-Ras4B HVR contains a single farnesyl modification and positively charged polylysine sequence. Earlier study has identified Serine 181 as a specific phosphorylation site required for oncogenic function of mutant K-Ras [162]. This site has also been implicated in targeting to membrane microdomains and regulation of downstream signaling of K-Ras. Therefore, it is important to define if residual Ser-181 assists mutant K-Ras gaining affinity to cortical actin network. In addition, phosphatidylserine, an anionic lipid, has been directly implicated in Ras cluster formation [82], but our observation connects the lipids with Ras through actin. Further research is needed to confirm if the affinity of K-Ras to cortical actin is established through phosphatidylserine.

In conclusion, our study demonstrated the power of correlative SRM and EM in revealing unseen details of biological molecules operating in a complex environment like the membrane. Using this tool, we have revealed distinct roles of distinct membrane compartments in organizing Ras small GTPases in an isoform-dependent manner. In addition to gaining initial insight into the identities of the compartments associated with H-Ras and K-Ras multimer formation and signaling, our results also suggest parallel mechanisms of multimer dynamics that impact both Ras isoforms. These exciting new insights motivate future work on further defining the molecular composition and dynamics of the membrane compartments linked to the multimers of various Ras isoforms.

Ultimately, these investigations may lead to novel strategies for targeting mutant Ras in diseases like human cancer.

3.4. Materials and Methods

3.4.1. Molecular cloning and establishment of stable cell lines

We used a genetically encoded photoactivatable fluorescent protein, PAmCherry1, to label C -terminal tail of H-Ras (tH), C -terminal tail of K-Ras (tK), H-Ras^{G12V} and K-Ras^{G12D} mutants. To generate expression plasmids for PAmCherry1-tH, PAmCherry1-tK, PAmCherry1-H-RAS-G12V and PAmCherry1-K-RAS-G12D, PCR fragments used for In-Fusion reactions were generated using Phusion High-Fidelity DNA Polymerase (M0530, New England Biolabs). We used the In-Fusion PCR HD Cloning kit (639649, Clontech) to generate genetic fusions in the pENTR (Life Technologies) backbones, and the Gateway LR Clonase II kit (11791, Life Technologies) to shuttle the resulting fusion constructs from the entry clones to expression clones. Lentiviral backbone (pLenti-puro-CMV/TetOn, 17293, Addgene) was used for expressing these clones. Viral particles containing pLenti-puro-CMV/Teton-PAmCherry1-tH, pLenti-puro-CMV/Teton-PAmCherry1-tK, pLenti-puro-CMV/Teton-PAmCherry1-H-Ras-G12V or pLenti-puro-CMV/Teton-PAmCherry1-K-Ras-G12D were generated using the ViraPower lentiviral packaging system (K497500, Life Technologies), which were then used to infect U2OS cells (HTB-96, ATCC) to make stable cell lines expressing PAmCherry1-tH, PAmCherry1-tK, PAmCherry1-H-Ras^{G12V} or PAmCherry1-K-Ras^{G12D} under tetracycline or doxycline regulation. Single clones were

isolated, grown out and assayed for repression of dox-induced gene expression; good clones were used for subsequent studies.

3.4.2. Preparation of membrane sheet

Cells were cultured at 37°C and 5% CO_2 in DMEM supplemented with 10% FBS (11995 and 10082 respectively, Life Technologies) and were plated on 25 mm diameter coverslips (72225-01, Electron Microscopy Sciences). To obtain isolated membrane sheet, cells are about 70% confluent before peeling. For Cytochalasin-D treated samples, cells were incubated with 1 µM cytochalasin-D for 30 minutes at 37 °C and briefly washed before peeling. To inhibit the formation of membrane vesicles and clathrin coated pits, cells were incubated with 50 µM Dyngo® 4a (ab120689, Abcam) for 1 hour at 37 °C.

Membrane sheet are prepared according to the protocol from Prior IA et al [ref]. #1.5 indium-tin-oxide (ITO) coated coverslips (06486-AB, SPI supplies) as a secondary surface were coated with 1 mg/ml poly-L-lysine (P1399, Sigma-Aldrich). Cells growing on normal coverslips (primary surface where cells originally growing on) were facing down and were pressed onto the poly-L-lysine coated ITO coverslips by a cork. Two coverslips were then carefully separated and membrane sheets attached to ITO coverslips were ripped off from cells. Surface of ITO coverslips were gentling washed with KOAc buffer (25mM Hepes, 115mM KOAc, 2.5mM MgCl2, pH 7.4) and membrane sheets were fixed immediately with 3.7% PFA and 0.1% glutaraldehyde in KOAc buffer for 20 min at room temperature. Gold particles (~100 nm in size, Cytodiagnotics, G-100-20) were added about 20–30 min prior to imaging so they could adhere to the coverslip and be used as fiduciaries.

3.4.3. Western Blot

For Western blotting, cells were plated in six-well plates at densities to reach confluency in 24-48 h. Cells were treated as indicated and harvested using a RIPA cell lysis buffer (Thermo Scientific, no. 89901) supplemented with a mixture of phosphatase and protease inhibitors (ThermoFisher no. 88668) and a cell scraper. Collected cell lysates were incubated on ice for 15 min and vortexed 3–5 times in the period. The lysates were then centrifuged at 12,000 × g and 4 °C for 10 min on an Eppendorf 5424 centrifuge equipped. Supernatants were collected and assayed with a BCA kit (ThermoFisher no. 23225) to measure the total protein concentrations. Equal amounts (10–20 μg) of total proteins for each sample were mixed with a 4× NuPAGE LDS loading buffer (Life Technologies, no. NP0007), supplemented with β-mercaptoethanol (βME). The mixture is brought to the correct volume with water, mixed, and heated at 95 °C for 10 min. After cooling down to room temperature, samples were loaded into a Bris-Tris gradient gel (4–12%, LifeTechnologies no. NP0323) and run at 110 V for 30 min and then 160 V for 60 min at room temperature. Protein transfer was performed on a wet-transfer system at 200 mA for 90 min with water cooling, using a low fluorescence PVDF membrane (EMD Milipore no. IPFL10100). Blots were incubated in blocking buffer (LiCOR no. 927–40000), primary antibodies diluted in blocking buffer, washed, followed by incubation with dye-secondary antibodies for imaging on a LiCOR Odyssey imager. Antibodies used for Western blotting in this study are: H-Ras (Rabbit polyclonal, Santa Cruz Biotechnology no. sc-520), KRas (Mouse monoclonal, Abcam no. ab55391), ppErk (Mouse monoclonal, Sigma-Aldrich no. M9692), tubulin (Mouse monoclonal, Life Technologies no. 32–2600), and total Erk (Mouse monoclonal, Cell Signaling Technology no. 4695).

3.4.4. Correlative imaging on membrane sheet

SRM imaging was performed on a Nikon Ti-U inverted microscope equipped with a Nikon 60× APO TIRF objective (NA = 1.49). Total internal reflection (TIR) illumination was used in all SRM imaging experiments. An open source software, μManager [134], was used to acquire raw SRM images. SRM image reconstruction was performed using home-written scripts in Matlab (MathWorks, MA).

After PALM imaging, membrane sheets on ITO coverslips were stained with 0.3% uranyl acetate solution (in water, pH=4.5) on ice for 1 hour. The samples were then dehydrated by a graded series of ethanol (50%, 60%, 70%, 80%, 90%, 95% and three times 100%) at 20 minute intervals. Following dehydration, solvent was removed with a critical point dryer (CPD300, Leica). Samples were then coated with 5 nm carbon using a Leica ACE600 coater before SEM imaging.

SEM images were taken at 2 kV with a FEI Helios 650 Nanolab FIB/SEM. Imaging was performed using the solid state concentric backscatter detector at a working distance of 4 mm.

3.4.5. Image analysis

SRM-SEM images were registered by 100 nm gold nanoparticles. Image registration was done using custom scripts based on the Control Point Registration toolbox in Matlab (Mathworks, Natick, MA). Typically a total number of 15–20 gold nanoparticles were used to register each SRM-SEM dataset.

To categorize vesicles and filamentous structures in SEM image, a simple intensity thresholding (i.e., Otsu's method 1) was applied to segment membrane vesicles and

filaments followed by morphological operation including dilation and erosion with chosen parameters to remove small objects and refine segmentation. After segmentation, the association of Ras molecules to segmented structures was determined by a colocalization analysis. To quantify proximity of Ras molecules to these microdomains, we calculated the distance from each Ras molecule to segmented microdomains and then assign each molecule to the microdomains within 20nm distance. If a Ras molecule is within 20 nm to both filaments and vesicles, it will be assigned twice to both filaments and vesicles since the localization precision of SEM is 20 nm.

To determine if the quantification result of SRM-SEM images is statistical significance, each SRM-SEM dataset was compared with a random condition. The random condition was created by shuffling the Ras molecules in a SRM image with fixed molecule density. This random distribution was then processed for a colocalization analysis with its corresponding segmented structures in SEM images. We shuffled the SRM images 100 times for each SRM-SEM dataset and an average quantification data was used to compare with experimental data.

Chapter IV. Future Direction

Ying Zhang, Ting Zheng, Lei Wu, Fehmi Civitci, Carey Phelps, Xiaolin Nan

Author contributions

Y. Zhang and X. Nan developed the hypothesis, conceptual and experimental designs, and are responsible for data analysis and interpretation. Y. Zhang performed all experiments and image processing. F. Civitci and C. Phelps helped with imaging process and oligo design. T. Zheng and L. Wu prepared and purified DNA-antibody conjugates. Y. Zhang and X. Nan wrote the manuscript.

Abstract

In Chapter 2, we have established optimal workflows for correlative SRM and SEM. In Chapter 3, we used correlative SRM and SEM to investigate the spatial organization and signaling of Ras in its membrane context. We were able to identify two distinct membrane compartments that regulate Ras multimer formation and signaling to Raf-MAPK, one as dynamin-dependent endocytic vesicles and the other as the cortical cytoskeleton. Being able to capture the morphological and structural characteristics, SRM-SEM offered important insight into the potential molecular identities of the two membrane compartments. Guided by these results, we propose to take advantage of multicolor imaging capability of SRM to further define the two membrane compartments. In particular, multicolor SRM allows *in situ* analysis of multiple molecular species at high spatial resolution, which can be correlated to SEM using an identical workflow as established in Chapters 2 and 3. This will provide more complete information about molecular compositions of Ras multimer-associated membrane compartments and aid in uncovering the biological identities of the membrane compartments.

4.1. Introduction

Photoactivated localization microscopy (PALM) [101] and stochastic optical reconstruction microscopy (STORM) [163] are two single molecule localization based imaging methods that achieve image resolution beyond the diffraction limit. These techniques use stochastic blinking of fluorescent probes so that their spatial localization can be determined with subdiffration precision [154]. PALM utilizes genetically encoded photoactivable/photoswitchable proteins that are tagged to the protein of interest. These fluorescent proteins are not fluorescent prior to photoswitching or activation. Single molecules are turned on in a stochastic manner, typically by irradiation with 405 nm laser. By contrast, STORM relies on organic dyes and special buffer conditions to assist photoswitching. Typical STORM imaging buffers contain catalase, glucose and glucose oxidase in combination with a reducing agent.

To understand the complexity of biological systems, multicolor super-resolution imaging is a powerful tool for detecting and locating a multitude of key molecular components. Multicolor SRM imaging was first achieved by using dichroic mirrors and bandpass filters to discriminate between fluorophores whose emission spectra are separated by 50-100 nm [153]. Due to their wide spectrum and heavy crosstalk, fluorescent proteins were rarely used in multicolor SRM imaging. Even with organic fluorophores, this filter-based signal separation method limits the practical spectral resolution to 3-4 colors, which requires 4-5 lasers and as expected, suffers from server spectral crosstalk between the fluorescence channels.

More recently, spectrally resolved stochastic optical reconstruction microscopy (SR-STORM) [164] and multispectral super-resolution microscopy (MSSRM) [165] were introduced for simultaneous imaging of four dyes with their emission maximum only 10 nm apart. The MSSRM was developed in our lab independently from the SR-STORM. In the SR-STORM imaging setup, two opposing objectives were used in a wide-field scheme to collect two images per fluorophore. The image collected through path 1 was used to determine the position of each fluorophore. In path 2, a dispersing prism was placed at the Fourier plane between the two relay lenses to generate spectra of the same fluorophore. The MSSRM uses a single-objective to collect signals from the field of view, after which the signals are split between a positional channel (~1/3) and a spectral channel (~2/3) for simultaneous location and spectrum determination. These approaches allowed concurrent four color SRM imaging using four spectrally overlapping dyes and a single-laser excitation, with an effective spectral resolution of 10-15 nm. Due to the stringent requirement in spectral resolution, SR-STORM and MSSRM demand robust photoswitching and high brightness of all the fluorescent dyes.

While PALM and STORM are both capable of multicolor imaging with optimized sample labeling, it is often difficult to combine PALM and STORM in a single experiment due to the incompatibility of most fluorescent proteins with STORM imaging buffer. Fluorescent proteins switch poorly in the STORM imaging buffer. For SRM imaging of Ras, currently PAmCherry1 remains the best probe because of the lack of isoform-specific antibodies. Thus, extending the current SRM-SEM workflow to a multicolor scheme for imaging Ras and the membrane compartments at once requires a solution other than STORM or the related SR-STORM and MSSRM.

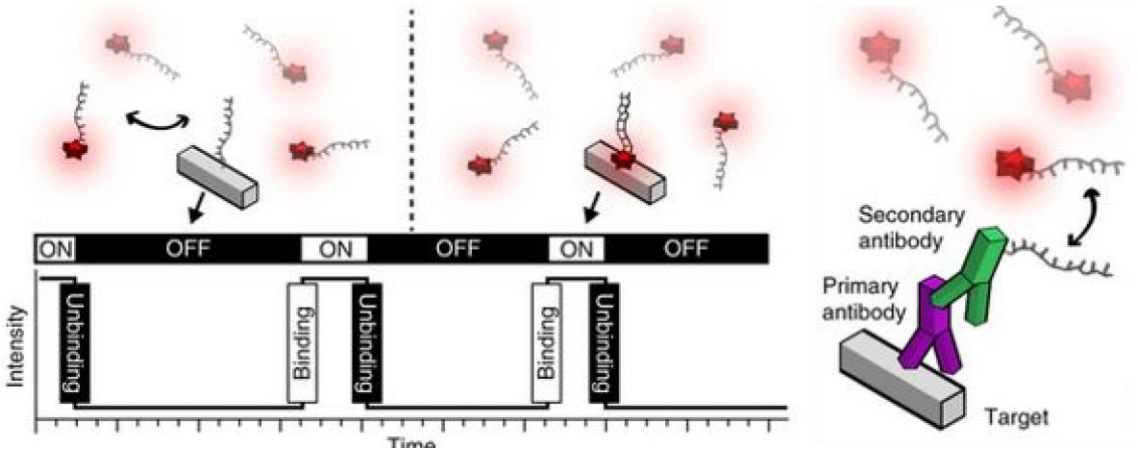

Figure 4.1 DNA-PANT concept (left) and labeling strategy using DNA-conjugated secondary antibodies (right) [165].

DNA-based point accumulation for imaging in nanoscale topography (DNA-PAINT) is a recent strategy for cyclic super-resolution imaging without needing to use photoswitching fluorophore or buffers. In DNA-PAINT, a target of interest is labeled with an antibody conjugated to a short DNA oligo (the 'docking strand' or DS); a complimentary DNA oligo is conjugated to a fluorophore (the 'imaging strand' or IS) and added to the solution at a concentration of a few nanomolar (nM). Transient binding of the IS to their complementary DS creates the 'blinking' at each target position to enable super-resolution imaging via single molecule localization (Fig 4.1) [166]. DNA-PAINT is in principle suited for multiplexed imaging because orthogonal DNA sequences can be used to label multiple targets and the imaging strands can be washed out to permit multiple rounds of labeling and imaging. Importantly, DNA-PAINT can be readily combined with PALM to achieve more colors because the imaging buffer for DNA-PAINT is typically PBS supplemented with sodium chloride, which is compatible with photoswitchable or

activatable fluorescent proteins used for PALM. This compatibility is very useful when one target is a small molecule that is difficult to label with an antibody.

We have developed a hybrid DNA-PAINT and PALM workflow to enable multicolor super-resolution imaging of Ras and several membrane structures in fixed cells. In the previous chapter, by using correlative super-resolution and scanning electron microscopy, we have identified the differential roles of membrane vesicles and cortical filamentous network in organizing H- and K-Ras signaling complexes at the cell membrane. However, the composition of the membrane vesicles has not be determined because SEM mostly provides structural and morphological information and lacks chemical specificity. Here, we used immunofluorescence to label multiple membrane components including clathrin, caveolae and actin. By linking DNA-PAINT docking strands to antibodies, we are able to implement multicolor SRM imaging with DNA-PAINT to image those targets. We demonstrated the performance of sequential multiplexing using the same fluorescent dye for DNA-PAINT and obtained three-color images. These results have clearly showed the feasibility of using DNA-PAINT and SRM to investigate nanoscopic heterogeneities in membrane organization, which can be used to further identify the ultrastructures that organize Ras proteins at the cell membrane.

4.2. Materials and Methods

4.2.1. Materials

Unmodified and fluorescently modified DNA oligonucleotides were purchased from Integrated DNA Technologies. Phalloidin amine was purchased from Santa Cruz Biotechnology. CF 640R succinimidyl ester was purchased from Biotium (#92108). DBCO-Sulfo-NHS ester and azido-PEG4-NHS ester were purchased from Click Chemistry Tools. NHS-azide was purchased from Thermofisher Scientific. Primary antibodies including mouse anti-clathrin heavy chain antibody and rabbit-anti-caveolin-1 antibody were purchased from Abcam. Unmodified AffiniPure Rabbit Anti-Mouse IgG (Jackson ImmunoResearch, 315-005-003) and AffiniPure Donkey Anti-Rabbit IgG (Jackson ImmunoResearch, 711-005-152) were purchased from Jackson Immuno Research. Ethylene carbonate was purchased from Sigma-Aldrich (#E26258). Lab-Tek II chambered coverglass was purchased from Thermo Fisher Scientific.

4.2.2. Conjugation of DNA strands to antibodies

As illustrated in Fig 4.2, docking strand conjugated secondary antibodies were generated with the following 3 steps.

1) DBCO-Sulfo-NHS was first incubated with Cy3-DNA docking strand-NH_2 in PBS (pH adjusted by $NaHCO_3$) for 2 hours at room temperature on a shaker covered in aluminum foil. Inclusion of Cy3 is useful for calculating the ratio of DNA docking strands to antibody in the conjugation products and observing cell immunostaining with docking strand-antibody conjugates before DNA PAINT experiments. The NHS ester will react with amine on the fluorescently modified DNA docking strands. After the reaction is

completed, DNA conjugates were purified by ethanol precipitation. To do this, 10% of total volume of 3M NaCl and 2.5X volume of 100% ethanol were mixed with product solution and then put in -80°C for 30 minutes to precipitate DNA. Centrifuge the product mixture at 14,000g for 40 minutes at 4°C and discard supernatant. Rinse the DNA pellet with 100% ethanol for three times. Discarded ethanol supernatant and let residuals evaporate. The DNA pellet was then dissolved in TBS.

2) Next, we used NHS-PEG4-N_3 to react with the NH_2 groups on the antibody. The PEG4 was introduced as a link spacer between the bulky antibody and the oligonucleotide. Reaction mixture contains a 10:1 molar ratio of NHS-PEG4-N_3 to antibody, with the pH adjusted by $NaHCO_3$. Incubate the solution for 2 hours at room temperature on a shaker. After the reaction is completed, unreacted NHS-PEG4-N_3 was removed using Amicon 50k centrifugal column (Millipore, #UFC505024). The column was first washed by 400 µL PBS. Discard flow-though, load the product solution and add 40 µL PBS. Spin the column at 1,500g for 1 minute at room temperature and discard flow-throug. Wash the column with 400 µL PBS for 15 times. To collect conjugated product, invert the column in an empty 1.5 mL vial and collect the flow-through by centrifuging. Measure the concentration on the NanoDrop spectrophotometer. The concentration of antibody is usually around 1.2 mg/ml, which is about ~70% yield. After this step, the antibody contained azide groups that were ready to react with DBCO on the DNA docking strands.

3) Finally, DBCO-DNA docking strand-Cy3 binds to azide-modified antibodies via copper-free click chemistry [134]. To do this, create a 10:1 ratio of DNA strands to antibody and incubate overnight at room temperature on a shaker covered in aluminum foil. The unreacted DNA strands were removed by using Amicon 50k centrifugal column

(Millipore, #UFC505024). The filter was first washed by 400 µL PBS. Discard flow-though, load the product solution and add 40 µL PBS. Spin the column at 1,500g for 1 minute at room temperature. Discard flow-through, wash the column with 400 µL PBS and spin at 1,500g for 1 min, repeat this washing by 3 times. To collect conjugated product, invert the column in an empty 1.5 mL vial and collect the flow-through by centrifuging. The antibody concentration and DNA to antibody ratio is measured using NanoDrop spectrophotometer. Typically ~1.2 mg/ml antibody and 3:1 DNA to antibody ratio can be obtained.

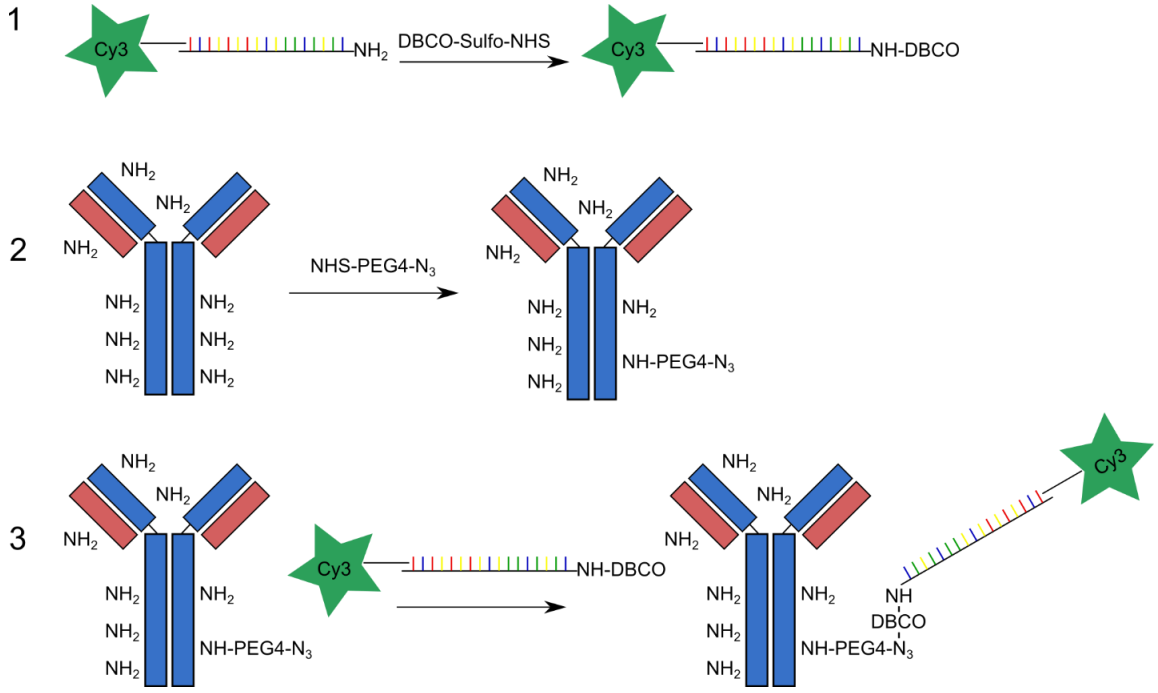

Figure 4.2 Schematic representation of DNA docking strands and antibody conjugation. DBCO-Sulfo-NHS first reacts with Cy3-DNA docking strand-NH2 to introduce DBCO group to the DNA docking strands. Next, NHS-PEG4-N_3 was used to react with the NH_2 groups on the antibody. Finally, DBCO-DNA docking strand-Cy3 binds to azide-modified antibodies via copper-free click chemistry.

The imager strand was generated in the similar method as the first step above. CF 640R NHS ester was first incubated with DNA imager strand-NH_2 in PBS (pH adjusted by $NaHCO_3$) for 2 hours at room temperature on a shaker covered in aluminum foil. After the reaction is completed, 10% of total volume of 3M NaCl and 2.5X volume of 100% ethanol were mixed with product solution and then put in -80°C for 30 minutes to precipitate DNA. Centrifuge the product mixture at 14,000g for 40 minutes at 4°C and discard supernatant. Rinse the DNA pellet with 100% ethanol for three times. Discarded ethanol supernatant and let ethanol residuals evaporate. The DNA pellet was then dissolved in TBS.

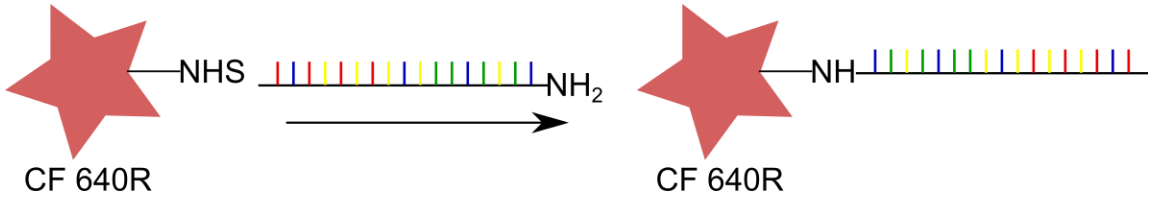

Figure 4.3 Schematic representation of DNA imager strands and dye conjugation.

4.2.3. Cell immunostaining

U2OS cells (human osteosarcoma, ATCC, HTB-96) were cultured at 37°C and 5% CO_2 in DMEM supplemented with 10% FBS (11995 and 10082 respectively, Life Technologies) and were seeded into Lab-Tek chambered coverglass (Thermo, 155409) 24 hours before fixation. Clathrin, Caveolae and actin were immunostained with the following procedure: fixation with freshly made 3.7% PFA in PHEM buffer (60mM Pipes, 25mM Hepes, 10mM EGTA, 2mM $MgCl_2$, PH 6.9) for 20 min; washing with PBS; block and permeabilize with 3% BSA (w/v) and 0.1% Saponin (w/v) for 30 min; incubation overnight with mouse anti-clathrin heavy chain antibody (abcam, ab24578), rabbit-anti-caveolin-1 antibody (abcam, ab32577) or preassembled phalloidin-DNA conjugates diluted to 10

μg/ml in 3% BSA (w/v) and 0.1% Saponin (w/v) plus 0.5 mg/ml Salmon Sperm DNA solution (Invitrogen, 15632011); washing with PBS for three times; incubation with preassembled anti-mouse-DNA and anti-rabbit-DNA conjugates diluted in in 3% BSA (w/v) and 0.1% Saponin (w/v) plus 0.5 mg/ml Salmon Sperm DNA solution for 1 hour; washing with PBS for three times; post-fixation with 3.7% PFA and 0.1% GA in PHEM buffer for 10 min; washing and adding 50 nm gold nanoparticles for drift correction.

4.2.4. Image acquisition and Image analysis

For single color imaging, the imaging buffer contained 10 nM CF 640R-labeled imager strands in 10% (v/v) ethylene carbonate in buffer C (1× PBS, 500 mM NaCl, pH 8). For multiplexed imaging, each target of interest were imaged sequentially with buffer exchange. In each cycle, 10 nM CF 640R-labeled imager strands imager strands in 10% (v/v) ethylene carbonate in buffer C (1× PBS, 500 mM NaCl, pH 8) was added to chambered-well. After image acquisition, imager strands were washed out completed before next cycle.

Image acquisition was performed on a Nikon Ti-U inverted microscope equipped with a Nikon 60× APO TIRF objective (NA = 1.49). Total internal reflection (TIR) illumination was used in imaging experiments. An open source software, μManager [134], was used to acquire raw dataset. Image reconstruction was performed using home-written scripts in Matlab (MathWorks, MA).

Multiplexed images were registered by 50 nm gold nanoparticles. Image registration was done using custom scripts based on the Control Point Registration toolbox in Matlab

(Mathworks, Natick, MA). Typically a total number of 8–15 gold nanoparticles were used to register each multi-color dataset.

4.3. Results

4.3.1. Imaging membrane ultrastructures with DNA-PAINT

We first tested the possibility of using oligo conjugation to secondary antibodies for imaging cell membrane structures with SRM based DNA-PAINT. Three membrane structures, clathrin, caveolae and actin were targeted. The results demonstrated that conjugation to docking strand does not influence the specific labeling of secondary antibodies. With optimized imaging conditions, SRM based DNA-PAINT was capable of resolving the morphology of nanoscopic structures on the cell membrane.

With DNA-PAINT, we first imaged clathrin coated pits (CCPs) in U2OS cells. From the SEM images of CCPs in Chapter 3, CPPs are spherical cage-like structures that are about 150 -200 nm in size. They are assembled from clathrin, the adaptor protein AP-2 and many other accessory factors. The formation of CCPs is important for internalization of receptors and extracellular ligands, for the recycling of plasma membrane components, and for the retrieval of surface proteins destined for degradation [103]. To image CCPs, we immunostained U2OS cells with a primary antibody against clathrin and a secondary antibody-DS-Cy3 conjugate. The correct immunostaining of secondary antibody-DS-Cy3 conjugate was confirmed based on Cy3 signal. When imaged by conventional fluorescence microscopy, all CCPs appeared as nearly diffraction-limited spots with no discernable structures. For DNA-PAINT, an imaging buffer containing 10 nM of CF 640R-IS was

introduced into the sample chamber prior to imaging. Assisted by ethylene carbonate, constant association and disassociation of CF 640R to the cell membrane was observed. From the reconstructed SRM images (Fig 4.4), the circular ring-like structures of the pit periphery were unambiguously resolved. The size of CCPs measured from SRM images are typically around 150-200 nm, which agrees with the size observed using SEM as shown in Chapter 2.

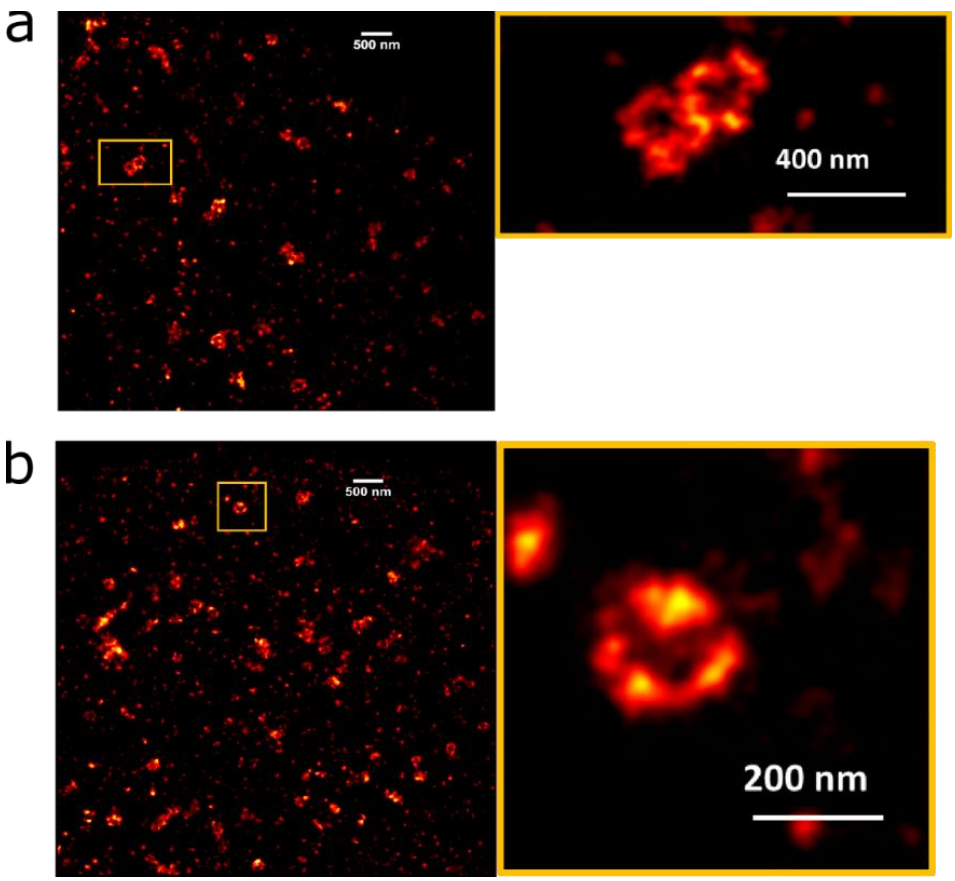

Figure 4.4 DNA-PAINT images of clathrin-coated pits in fixed cell.

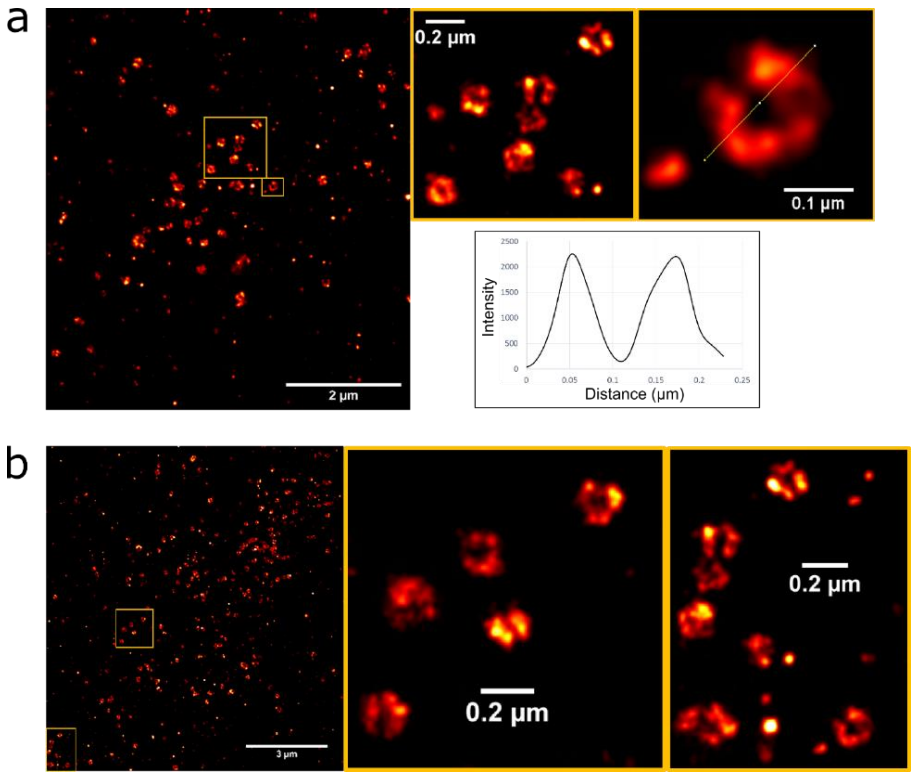

Figure 4.5 DNA-PAINT images of caveolae in fixed cell.

Next, we imaged caveolae, which mediate one of the dynamin-dependent but clathrin-independent endocytosis pathways. Caveolae are rich lipids such as cholesterol and sphingolipids and have been considered a special type of lipid rafts. Similar to the CCPs, caveolae appeared as nearly diffraction-limited spots when imaged with conventional fluorescence microscopy, which is expected since the size of caveolae ranges from 50-150 nm depending on the cell type. To image caveolae with DNA-PAINT, U2OS cells were stained with a primary antibody against caveolin-1 followed by incubation with a secondary antibody-DS-Cy3 conjugate. Here the DS has a distinct sequence to that used for caveolae imaging. SRM based DNA PAINT images clearly resolved the circular structure of the periphery of the caveolae at the cell membrane (Fig 4.5). According to the cross-sectional profiles of the caveolae in Fig 4.5a, the size of ring-like caveolae is ~120

nm as measured, which is consistent with the diameter of caveolae determined in previous EM studies.

We also tested DNA-PAINT imaging of the actin cytoskeleton in fixed cells by using a small molecule labeling agent instead of an antibody. To this end, a new DS-Cy3 was conjugated to phalloidin, which binds to F-actin with high specificity. After fixation and blocking, cells were stained with DS-phalloidin-Cy3 conjugates overnight at 4°C. It turned out that the DS-phalloidin-Cy3 conjugates stained actin with high specificity and high density. Networks of thick stress fibers and thinner filaments were both resolved in the reconstructed SRM images (Fig 4.6). In addition, we also observed many small actin clusters in the form of somewhat elongated dots. The presence of distinct cortical filaments suggests that the ultrastructure of the F-actin network is well-preserved and sufficiently stained with DNA-phalloidin conjugates. Thus, SRM based DNA-PAINT is capable of characterizing the cytoskeleton architecture on the cell membrane as well.

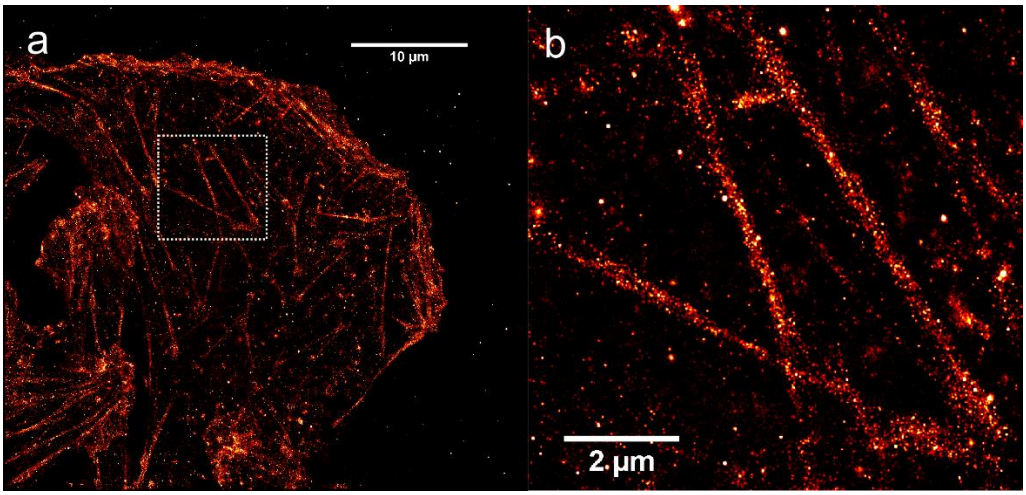

Figure 4.6 DNA-PAINT images of actin in fixed cell.

4.3.2. Multiplexed membrane imaging with DNA-PAINT

Next, we extended DNA-PAINT for multiplexed imaging of multiple membrane structures. This was obtained by coupling CF 640R to multiple IS with orthogonal sequences, each corresponding to a unique DS as previously used. The orthogonality of IS ensures that there is no crosstalk between the different target channels [103]. The experimental scheme for multiplexed DNA-PAINT imaging is illustrated in Fig 4.7, which is described as exchange-PAINT by Jungmann et al., [102]. Briefly, each target was labeled with an antibody carrying a unique DS oligo, and IS oligoes tagged with CF 640R were sequentially introduced into the same sample chamber prior to each imaging cycle after the last IS has been washed out. For example, during cycle 1, only IS1 was present in the imaging buffer, and actin was specifically imaged. After image acquisition of cycle 1 was complete, IS1 was washed out simply by flowing in blank imaging buffer (with no IS). Then, IS2 was introduced for imaging cycle 2, where CCPs were imaged. By repeating the imaging cycles three times, we achieved three color SRM imaging of cortical actin, CCPs, and caveolae using the same dye, CF 640R (Fig 4.7). SRM images from same field of view were registered using 50 nm gold nanoparticles as described in *Methods*. From the resulting SRM images, we observed that all three membrane structures are well resolved with much better spatial resolution compared to conventional fluorescence microscopy.

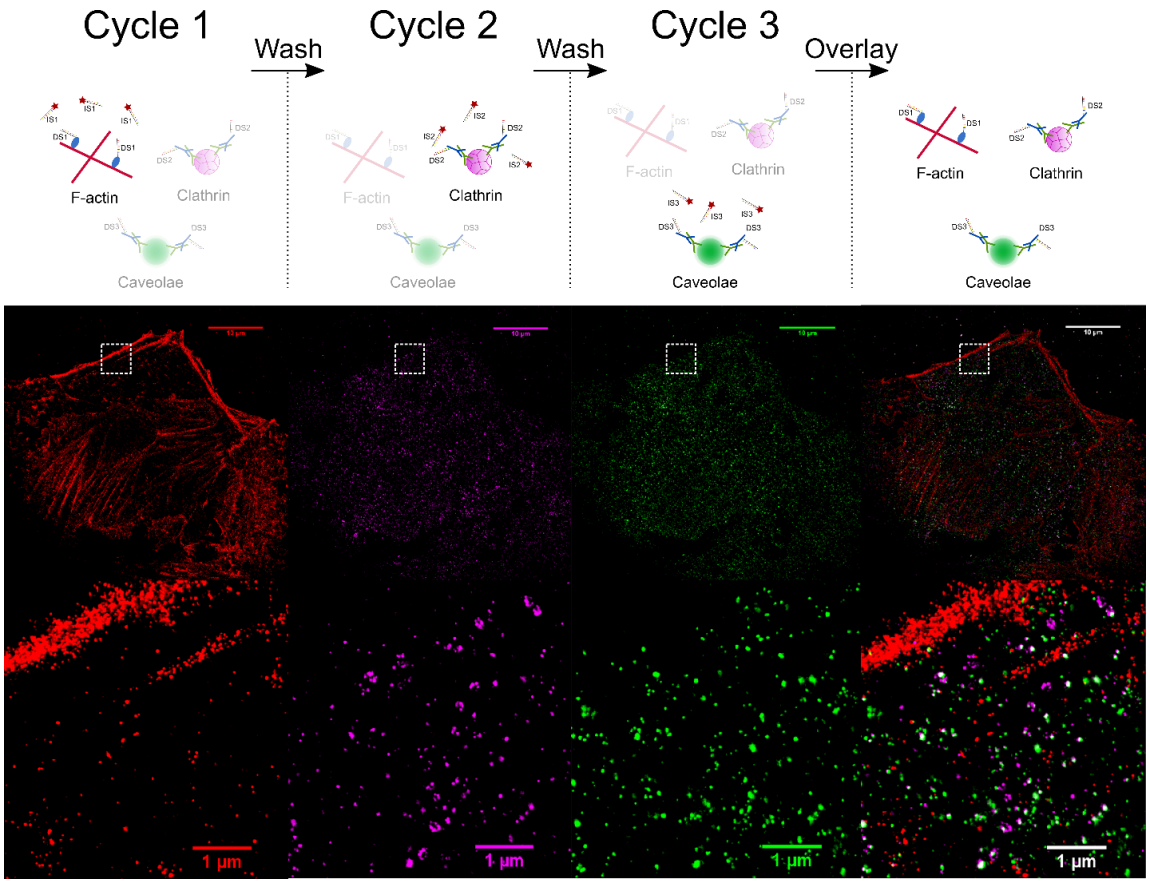

Figure 4.7 Multiplexed imaging of membrane structures with DNA-PAINT.

4.4. Discussion and future work

In this chapter, we demonstrated multiplexed imaging of three membrane ultrastructures using exchange-PAINT. Compared with prior SRM methods based on PALM [102] or STORM [101], exchange-PAINT enables multiplexed SRM simply through multi-round imaging using multiple, orthogonal DNA sequences. Multi-color SRM imaging was previously achieved by using dichroic mirror and bandpass filter [154] or by using dispersing prism [153,164] to distinguish the emission of different dyes.

However, these methods are heavily dependent on selection of spectrally distinct dyes. In exchange-PAINT, orthogonal docking strand sequences were used to tag different targets. Therefore, the targets are distinguished based on orthogonal DNA sequences instead of the spectra of the dyes. As such, multicolor imaging is achieved without having to deal with spectral crosstalk. Since the only limitation is the orthogonality of DNA sequences, multiplexed imaging can be extended to tens or even hundreds of targets. To date, exchange-PAINT has demonstrated nine-color SRM imaging in cells [103,167]. The use of secondary antibodies for multiplexed detection in our experiment, however, is limited by the availability of primary antibodies from different species. To address this issue, direct conjugation of DNA docking strands to primary antibodies or small molecules will be one of the future efforts to achieve more colors.

Other advantages of DNA-PAINT include the selection of optimal dyes with good photostability and photon yield. In previous multi-color imaging experiments, the photophysical properties of the dye used in each channel, such as the photoswitching performance, photon output, duty cycle, and compatibility with the imaging buffers, are all critical to successful high-resolution imaging. In DNA-PAINT, the same dye can be used to tag all IS oligos as long as their sequences are orthogonal (i.e., one IS does not hybridize with another DS). The remaining consideration will be the brightness of the dye. Since the imaging process of DNA-PAINT does not involve photoswitching, it becomes much more straightforward to choose an optimal fluorophore from the vast repertoire of existing fluorophores without having to go through a tedious step to screen for the best photoswitchers as in STORM. Once chosen, the dye can be used for all the imaging cycles. Moreover, DNA-PAINT is intrinsically insensitive to loss of fluorescent probes due to

photobleaching. Instead, there is essentially unlimited supply of dye-IS in the solution that can probe the same targets again and again during image acquisition. Hence, compared to STORM and PALM, DNA-PAINT is more likely to yield quantitative results by avoiding any loss of fluorescent probes, which is particularly valuable for low abundance targets.

In spite of these advantages, there are still some limitations to DNA-PAINT, one of which is the slow image acquisition. Each raw image frame in DNA-PAINT takes 100-300 ms, which is about an order of magnitude slower than STORM and PALM. This may be overcome by combing DNA-PAINT with spectral-resolved STORM [153] or MSSRM [164] with DNA-PAINT. Another limitation is that it remains difficult to use DNA-PAINT for live cell imaging, due to the need for using antibodies and for the slow imaging speed. For live cell SRM imaging, typically 100-1,000 raw image frames are needed to reconstruct a single SRM image, which makes the time resolution essentially impractical when using DNA-PAINT.

With future improvements on various aspects, multiplexed imaging with DNA-PAINT will be a powerful tool to resolve membrane ultrastructures that organizing Ras signaling complexes at the cell membrane. As discussed in Chapter 3, we have identified distinct roles of membrane filaments and vesicles including CCPs in organizing and regulating the membrane localization and signaling output of H- and K-Ras. CCPs can be easily defined with SEM based on their distinct morphology. Some other vesicles, such as caveolae, are more difficult to identify unambiguously since SEM does not provide composition information of those vesicles. Moreover, some of the Ras multimer-associated membrane compartment may not fall in any known categories. Therefore, we propose to use correlative DNA-PAINT with EM as the potential next step to further define the

membrane compartments. With more complete information about the molecular compositions of these membrane compartments, we will be able to bring our understanding of how the activities of the various Ras isoforms are intricately regulated by these heterogeneous, nanoscale structures to achieve robust yet versatile signaling.

References

1. Wennerberg K, Rossman KL, Der CJ. The Ras superfamily at a glance. J Cell Sci. The Company of Biologists Ltd; 2005;118: 843–6. doi:10.1242/jcs.01660

2. Rojas AM, Fuentes G, Rausell A, Valencia A. The Ras protein superfamily: Evolutionary tree and role of conserved amino acids. J Cell Biol. Rockefeller University Press; 2012;196: 545–545. doi:10.1083/jcb.2011030081964c

3. HARVEY JJ. An Unidentified Virus which causes the Rapid Production of Tumours in Mice. Nature. Nature Publishing Group; 1964;204: 1104–1105. doi:10.1038/2041104b0

4. Kirsten WH, Mayer LA. Morphologic responses to a murine erythroblastosis virus. J Natl Cancer Inst. 1967;39: 311–35. Available: http://www.ncbi.nlm.nih.gov/pubmed/18623947

5. Scolnick EM, Rands E, Williams D, Parks WP. Studies on the nucleic acid sequences of Kirsten sarcoma virus: a model for formation of a mammalian RNA-containing sarcoma virus. J Virol. American Society for Microbiology (ASM); 1973;12: 458–63. Available: http://www.ncbi.nlm.nih.gov/pubmed/4127029

6. Scolnick EM, Parks WP. Harvey sarcoma virus: a second murine type C sarcoma virus with rat genetic information. J Virol. 1974;13: 1211–9. Available: http://www.ncbi.nlm.nih.gov/pubmed/4364897

7. Shih TY, Weeks MO, Young HA, Scholnick EM. Identification of a sarcoma virus-coded phosphoprotein in nonproducer cells transformed by Kirsten or Harvey murine sarcoma virus. Virology. 1979;96: 64–79. Available: http://www.ncbi.nlm.nih.gov/pubmed/223311

8. Scolnick EM, Papageorge AG, Shih TY. Guanine nucleotide-binding activity as an assay for src protein of rat-derived murine sarcoma viruses. Proc Natl Acad Sci U S A. 1979;76: 5355–9. Available: http://www.ncbi.nlm.nih.gov/pubmed/228288

9. Maertens O, Cichowski K. An expanding role for RAS GTPase activating proteins (RAS GAPs) in cancer. Adv Biol Regul. 2014;55: 1–14. doi:10.1016/j.jbior.2014.04.002

10. Barbacid M. ras Genes. Annu Rev Biochem. Annual Reviews 4139 El Camino Way, P.O. Box 10139, Palo Alto, CA 94303-0139, USA ; 1987;56: 779–827. doi:10.1146/annurev.bi.56.070187.004023

11. Castellano E, Santos E. Functional specificity of ras isoforms: so similar but so different. Genes Cancer. Impact Journals, LLC; 2011;2: 216–31. doi:10.1177/1947601911408081

12. Prior IA, Lewis PD, Mattos C. A Comprehensive Survey of Ras Mutations in Cancer. Cancer Res. 2012;72: 2457–2467. doi:10.1158/0008-5472.CAN-11-2612

13. Hancock JF. Ras proteins: different signals from different locations. Nat Rev Mol Cell Biol. Nature Publishing Group; 2003;4: 373–385. doi:10.1038/nrm1105

14. Wohlgemuth S, Kiel C, Krä Mer A, Serrano L, Wittinghofer F, Herrmann C. Recognizing and Defining True Ras Binding Domains I: Biochemical Analysis. doi:10.1016/j.jmb.2005.02.048

15. Vetter IR. The Guanine Nucleotide-Binding Switch in Three Dimensions. Science (80-). 2001;294: 1299–1304. doi:10.1126/science.1062023

16. Wittinghofer A, Vetter IR. Structure-Function Relationships of the G Domain, a Canonical Switch Motif. Annu Rev Biochem. Annual Reviews ; 2011;80: 943–971. doi:10.1146/annurev-biochem-062708-134043

17. Milburn M V, Tong L, deVos AM, Brünger A, Yamaizumi Z, Nishimura S, et al. Molecular switch for signal transduction: structural differences between active and inactive forms of protooncogenic ras proteins. Science. American Association for the Advancement of Science; 1990;247: 939–45. doi:10.1126/SCIENCE.2406906

18. Schlichting I, Almo SC, Rapp G, Wilson K, Petratos K, Lentfer A, et al. Time-resolved X-ray crystallographic study of the conformational change in Ha-Ras p21 protein on GTP hydrolysis. Nature. Nature Publishing Group; 1990;345: 309–315. doi:10.1038/345309a0

19. Laude AJ, Prior IA. Palmitoylation and localisation of RAS isoforms are modulated by the hypervariable linker domain. J Cell Sci. The Company of Biologists Ltd; 2008;121: 421–7. doi:10.1242/jcs.020107

20. Ahearn IM, Haigis K, Bar-Sagi D, Philips MR. Regulating the regulator: post-translational modification of RAS. Nat Rev Mol Cell Biol. Nature Publishing Group; 2011;13: 39–51. doi:10.1038/nrm3255

21. Konstantinopoulos PA, Karamouzis M V., Papavassiliou AG. Post-translational modifications and regulation of the RAS superfamily of GTPases as anticancer targets. Nat Rev Drug Discov. Nature Publishing Group; 2007;6: 541–555. doi:10.1038/nrd2221

22. Loirand G, Sauzeau V, Pacaud P. Small G Proteins in the Cardiovascular System: Physiological and Pathological Aspects. Physiol Rev. American Physiological Society Bethesda, MD; 2013;93: 1659–1720. doi:10.1152/physrev.00021.2012

23. Cox AD, Der CJ, Philips MR. Targeting RAS Membrane Association: Back to the Future for Anti-RAS Drug Discovery? Disclosure of Potential Conflicts of Interest CME Staff Planners' Disclosures Learning Objectives. Clin Cancer Res. 21: 1819–27. doi:10.1158/1078-0432.CCR-14-3214

24. Schubbert S, Shannon K, Bollag G. Hyperactive Ras in developmental disorders and cancer. Nat Rev Cancer. Nature Publishing Group; 2007;7: 295–308. doi:10.1038/nrc2109

25. Repasky GA, Chenette EJ, Der CJ. Renewing the conspiracy theory debate: does Raf function alone to mediate Ras oncogenesis? doi:10.1016/j.tcb.2004.09.014

26. Zenonos K, Kyprianou K. RAS signaling pathways, mutations and their role in colorectal cancer. World J Gastrointest Oncol. Baishideng Publishing Group Inc; 2013;5: 97–101. doi:10.4251/wjgo.v5.i5.97

27. Dhillon AS, Hagan S, Rath O, Kolch W. MAP kinase signalling pathways in cancer. Oncogene. Nature Publishing Group; 2007;26: 3279–3290. doi:10.1038/sj.onc.1210421

28. Hung C-M, Garcia-Haro L, Sparks CA, Guertin DA. mTOR-dependent cell survival mechanisms. Cold Spring Harb Perspect Biol. Cold Spring Harbor Laboratory Press; 2012;4: a008771. doi:10.1101/cshperspect.a008771

29. Slomovitz BM, Coleman RL. The PI3K/AKT/mTOR pathway as a therapeutic target in endometrial cancer. Clin Cancer Res. American Association for Cancer Research; 2012;18: 5856–64. doi:10.1158/1078-0432.CCR-12-0662

30. Targeting PI3K/AKT/mTOR pathway in non small cell lung cancer. Biochem Pharmacol. Elsevier; 2014;90: 197–207. doi:10.1016/J.BCP.2014.05.011

31. Wolthuis R, Bos J. Ras caught in another affair: the exchange factors for Ral. Curr Opin Genet Dev. 1999;9: 112–117.

32. González-García A, Pritchard CA, Paterson HF, Mavria G, Stamp G, Marshall CJ. RalGDS is required for tumor formation in a model of skin carcinogenesis. Cancer Cell. 2005;7: 219–226. doi:10.1016/j.ccr.2005.01.029

33. Lambert JM, Lambert QT, Reuther GW, Malliri A, Siderovski DP, Sondek J, et al. Tiam1 mediates Ras activation of Rac by a PI(3)K-independent mechanism. Nat Cell Biol. Nature Publishing Group; 2002;4: ncb833. doi:10.1038/ncb833

34. Shibatohge M, Kariya K i, Liao Y, Hu CD, Watari Y, Goshima M, et al. Identification of PLC210, a Caenorhabditis elegans phospholipase C, as a putative effector of Ras. J Biol Chem. American Society for Biochemistry and Molecular Biology; 1998;273: 6218–22. doi:10.1074/JBC.273.11.6218

35. Ras oncogenes and their downstream targets. Biochim Biophys Acta - Mol Cell Res. Elsevier; 2007;1773: 1177–1195. doi:10.1016/J.BBAMCR.2007.01.012

36. Matallanas D, Birtwistle M, Romano D, Zebisch A, Rauch J, von Kriegsheim A, et al. Raf family kinases: old dogs have learned new tricks. Genes Cancer. Impact Journals, LLC; 2011;2: 232–60. doi:10.1177/1947601911407323

37. Dhillon AS, Meikle S, Yazici Z, Eulitz M, Kolch W. Regulation of Raf-1 activation and signalling by dephosphorylation. EMBO J. European Molecular Biology Organization; 2002;21: 64–71. doi:10.1093/EMBOJ/21.1.64

38. Chong H, Lee J, Guan KL. Positive and negative regulation of Raf kinase activity and function by phosphorylation. EMBO J. European Molecular Biology Organization; 2001;20: 3716–27. doi:10.1093/emboj/20.14.3716

39. Fabian JR, Vojtekt AB, Coopert JA, Morrison DK. A single amino acid change in Raf-1 inhibits Ras binding and alters Raf-1 function (signal transduction/GTP-

binding protein/protein-serine/threonine kinases). Biochemistry. 1994;91: 5982–5986. Available: http://www.pnas.org/content/91/13/5982.long

40. Leonard TA, Hurley JH. Regulation of protein kinases by lipids. Curr Opin Struct Biol. 2011;21: 785–791. doi:10.1016/j.sbi.2011.07.006

41. Freeman AK, Ritt DA, Morrison DK. The importance of Raf dimerization in cell signaling. Small GTPases. Taylor & Francis; 2013;4: 180–5. doi:10.4161/sgtp.26117

42. Rushworth LK, Hindley AD, Neill EO, Kolch W. Regulation and Role of Raf-1 / B-Raf Heterodimerization. Mol Cell Biol. 2006;26: 2262–2272. doi:10.1128/MCB.26.6.2262

43. Wan PTC, Garnett MJ, Roe SM, Lee S, Niculescu-Duvaz D, Good VM, et al. Mechanism of activation of the RAF-ERK signaling pathway by oncogenic mutations of B-RAF. Cell. 2004;116: 855–67. Available: http://www.ncbi.nlm.nih.gov/pubmed/15035987

44. Carnahan J, Beltran PJ, Babij C, Le Q, Rose MJ, Vonderfecht S, et al. Selective and potent Raf inhibitors paradoxically stimulate normal cell proliferation and tumor growth. Mol Cancer Ther. American Association for Cancer Research; 2010;9: 2399–410. doi:10.1158/1535-7163.MCT-10-0181

45. Weber CK, Slupsky JR, Andreas Kalmes H, Rapp UR. Active ras induces heterodimerization of cRaf and BRaf. Cancer Res. 2001;61: 3595–3598.

46. Nan X, Tamgüney TM, Collisson EA, Lin L-J, Pitt C, Galeas J, et al. Ras-GTP dimers activate the Mitogen-Activated Protein Kinase (MAPK) pathway. Proc Natl Acad Sci U S A. National Academy of Sciences; 2015;112: 7996–8001. doi:10.1073/pnas.1509123112

47. Plowman SJ, Muncke C, Parton RG, Hancock JF. H-ras, K-ras, and inner plasma membrane raft proteins operate in nanoclusters with differential dependence on the actin cytoskeleton. Proc Natl Acad Sci. 2005;102: 15500–15505. doi:10.1073/pnas.0504114102

48. Scheffzek K, Ahmadian MR, Kabsch W, Wiesmüller L, Lautwein A, Schmitz F, et al. The Ras-RasGAP Complex: Structural Basis for GTPase Activation and Its Loss in Oncogenic Ras Mutants. Science (80-). American Association for the Advancement of Science; 1997;277: 333–338. doi:10.1126/science.277.5324.333

49. Simanshu DK, Nissley D V, Mccormick F. RAS Proteins and Their Regulators in Human Disease. Lead Edge Rev. 2017;170: 17–33. doi:10.1016/j.cell.2017.06.009

50. Ostrem JM, Peters U, Sos ML, Wells JA, Shokat KM. K-Ras(G12C) inhibitors allosterically control GTP affinity and effector interactions. Nature. Nature Publishing Group; 2013;503: 548–551. doi:10.1038/nature12796

51. Maurer T, Garrenton LS, Oh A, Pitts K, Anderson DJ, Skelton NJ, et al. Small-molecule ligands bind to a distinct pocket in Ras and inhibit SOS-mediated nucleotide exchange activity. Proc Natl Acad Sci U S A. National Academy of

Sciences; 2012;109: 5299–304. doi:10.1073/pnas.1116510109

52. Shima F, Yoshikawa Y, Ye M, Araki M, Matsumoto S, Liao J, et al. In silico discovery of small-molecule Ras inhibitors that display antitumor activity by blocking the Ras-effector interaction. Proc Natl Acad Sci U S A. National Academy of Sciences; 2013;110: 8182–7. doi:10.1073/pnas.1217730110

53. Alberts B, Johnson A, Lewis J, Raff M, Roberts K, Walter P. Molecular biology of the cell. Garland Science; 2002.

54. Cichowski K, Jänne PA. Drug discovery: Inhibitors that activate. Nature. Nature Publishing Group; 2010;464: 358–359. doi:10.1038/464358a

55. Samatar AA, Poulikakos PI. Targeting RAS–ERK signalling in cancer: promises and challenges. Nat Rev Drug Discov. Nature Publishing Group; 2014;13: 928–942. doi:10.1038/nrd4281

56. Singer SJ, Nicolson GL. The fluid mosaic model of the structure of cell membranes. Science. 1972;175: 720–31. Available: http://www.ncbi.nlm.nih.gov/pubmed/4333397

57. Steck TL, Yu J. Selective solubilization of proteins from red blood cell membranes by protein perturbants. J Supramol Struct. 1973;1: 220–232. doi:10.1002/jss.400010307

58. Kurzchalia T V., Friedrichson T. Microdomains of GPI-anchored proteins in living cells revealed by crosslinking. Nature. 1998;394: 802–805. doi:10.1038/29570

59. Pralle A, Keller P, Florin EL, Simons K, Hörber JK. Sphingolipid-cholesterol rafts diffuse as small entities in the plasma membrane of mammalian cells. J Cell Biol. 2000;148: 997–1008. Available: http://www.ncbi.nlm.nih.gov/pubmed/10704449

60. Mayor S, Varma R. GPI-anchored proteins are organized in submicron domains at the cell surface. Nature. 1998;394: 798–801. doi:10.1038/29563

61. van Meer G, Stelzer EH, Wijnaendts-van-Resandt RW, Simons K. Sorting of sphingolipids in epithelial (Madin-Darby canine kidney) cells. J Cell Biol. 1987;105: 1623–35. Available: http://www.ncbi.nlm.nih.gov/pubmed/3667693

62. Brown DA, Rose JK. Sorting of GPI-anchored proteins to glycolipid-enriched membrane subdomains during transport to the apical cell surface. Cell. 1992;68: 533–44. Available: http://www.ncbi.nlm.nih.gov/pubmed/1531449

63. Sharmin N. Ahmed ‡, Deborah A. Brown ‡,‖ and, Erwin London* ‡,§,‖. On the Origin of Sphingolipid/Cholesterol-Rich Detergent-Insoluble Cell Membranes: Physiological Concentrations of Cholesterol and Sphingolipid Induce Formation of a Detergent-Insoluble, Liquid-Ordered Lipid Phase in Model Membranes. American Chemical Society ; 1997; doi:10.1021/BI971167G

64. Sezgin E, Levental I, Mayor S, Eggeling C. The mystery of membrane organization: composition, regulation and roles of lipid rafts. Nat Rev Mol Cell Biol. 2017;18: 361–374. doi:10.1038/nrm.2017.16

65. Heerklotz H. Triton Promotes Domain Formation in Lipid Raft Mixtures. Biophys J. 2002;83: 2693–2701. doi:10.1016/S0006-3495(02)75278-8

66. Simons K, Ikonen E. Functional rafts in cell membranes. Nature. Nature Publishing Group; 1997;387: 569–572. doi:10.1038/42408

67. Marwali MR, Rey-Ladino J, Dreolini L, Shaw D, Takei F. Membrane cholesterol regulates LFA-1 function and lipid raft heterogeneity. Blood. American Society of Hematology; 2003;102: 215–22. doi:10.1182/blood-2002-10-3195

68. Pike LJ. Lipid rafts: heterogeneity on the high seas. Biochem J. Portland Press Limited; 2004;378: 281–92. doi:10.1042/BJ20031672

69. Yang S-T, Kreutzberger AJB, Kiessling V, Ganser-Pornillos BK, White JM, Tamm LK. HIV virions sense plasma membrane heterogeneity for cell entry. Sci Adv. American Association for the Advancement of Science; 2017;3: e1700338. doi:10.1126/sciadv.1700338

70. Kusumi A, Nakada C, Ritchie K, Murase K, Suzuki K, Murakoshi H, et al. Paradigm Shift of the Plasma Membrane Concept from the Two-Dimensional Continuum Fluid to the Partitioned Fluid: High-Speed Single-Molecule Tracking of Membrane Molecules. Annu Rev Biophys Biomol Struct. 2005;34: 351–378. doi:10.1146/annurev.biophys.34.040204.144637

71. Suzuki K, Ritchie K, Kajikawa E, Fujiwara T, Kusumi A. Rapid hop diffusion of a G-protein-coupled receptor in the plasma membrane as revealed by single-molecule techniques. Biophys J. The Biophysical Society; 2005;88: 3659–80. doi:10.1529/biophysj.104.048538

72. Sadegh S, Higgins JL, Mannion PC, Tamkun MM, Krapf D. The Plasma Membrane is Compartmentalized by a Self-Similar Cortical Actin Meshwork. 2017; Available: https://arxiv.org/pdf/1702.03997.pdf

73. Klammt C, Lillemeier BF. How membrane structures control T cell signaling. Front Immunol. Frontiers Media SA; 2012;3: 291. doi:10.3389/fimmu.2012.00291

74. Prior IA, Parton RG, Hancock JF. Observing Cell Surface Signaling Domains Using Electron Microscopy. Sci Signal. 2003;2003. Available: http://stke.sciencemag.org/content/2003/177/pl9.full

75. Prior IA, Muncke C, Parton RG, Hancock JF. Direct visualization of Ras proteins in spatially distinct cell surface microdomains. J Cell Biol. The Rockefeller University Press; 2003;160: 165–70. doi:10.1083/jcb.200209091

76. Garcia-Parajo MF, Cambi A, Torreno-Pina JA, Thompson N, Jacobson K. Nanoclustering as a dominant feature of plasma membrane organization. J Cell Sci. doi:10.1242/jcs.146340

77. Murakoshi H, Iino R, Kobayashi T, Fujiwara T, Ohshima C, Yoshimura A, et al. Single-molecule imaging analysis of Ras activation in living cells. Proc Natl Acad Sci U S A. National Academy of Sciences; 2004;101: 7317–22. doi:10.1073/pnas.0401354101

78. Niv H, Gutman O, Kloog Y, Henis YI. Activated K-Ras and H-Ras display different interactions with saturable nonraft sites at the surface of live cells. J Cell Biol. 2002;157: 865–872. doi:10.1083/jcb.200202009

79. Tian T, Harding A, Inder K, Plowman S, Parton RG, Hancock JF. Plasma membrane nanoswitches generate high-fidelity Ras signal transduction. Nat Cell Biol. 2007;9: 905–914. doi:10.1038/ncb1615

80. Harding A, Hancock JF. Ras nanoclusters: Combining digital and analog signaling. Cell Cycle. Taylor & Francis; 2008;7: 127–134. doi:10.4161/cc.7.2.5237

81. Abankwa D, Gorfe AA, Hancock JF. Ras nanoclusters: Molecular structure and assembly. Semin Cell Dev Biol. Academic Press; 2007;18: 599–607. doi:10.1016/J.SEMCDB.2007.08.003

82. Zhou Y, Wong C-O, Cho K, van der Hoeven D, Liang H, Thakur DP, et al. Membrane potential modulates plasma membrane phospholipid dynamics and K-Ras signaling. Science. American Association for the Advancement of Science; 2015;349: 873–6. doi:10.1126/science.aaa5619

83. Güldenhaupt J, Rudack T, Bachler P, Mann D, Triola G, Waldmann H, et al. N-Ras forms dimers at POPC membranes. Biophys J. The Biophysical Society; 2012;103: 1585–93. doi:10.1016/j.bpj.2012.08.043

84. Lin W-C, Iversen L, Tu H-L, Rhodes C, Christensen SM, Iwig JS, et al. H-Ras forms dimers on membrane surfaces via a protein-protein interface. Proc Natl Acad Sci U S A. National Academy of Sciences; 2014;111: 2996–3001. doi:10.1073/pnas.1321155111

85. Chung JK, Lee YK, Lam HYM, Groves JT. Covalent Ras Dimerization on Membrane Surfaces through Photosensitized Oxidation. J Am Chem Soc. NIH Public Access; 2016;138: 1800–3. doi:10.1021/jacs.5b12648

86. Spencer-Smith R, Koide A, Zhou Y, Eguchi RR, Sha F, Gajwani P, et al. Inhibition of RAS function through targeting an allosteric regulatory site. Nat Chem Biol. Nature Publishing Group; 2016;13: 62–68. doi:10.1038/nchembio.2231

87. Chen M, Peters A, Huang T, Nan X. Ras Dimer Formation as a New Signaling Mechanism and Potential Cancer Therapeutic Target. Mini Rev Med Chem. Bentham Science Publishers; 2016;16: 391–403. doi:10.2174/1389557515666151001152212

88. Tamm LK, McConnell HM. Supported phospholipid bilayers. Biophys J. Cell Press; 1985;47: 105–113. doi:10.1016/S0006-3495(85)83882-0

89. Veatch SL, Keller SL. Separation of liquid phases in giant vesicles of ternary mixtures of phospholipids and cholesterol. Biophys J. The Biophysical Society; 2003;85: 3074–83. doi:10.1016/S0006-3495(03)74726-2

90. Kahya N, Scherfeld D, Bacia K, Schwille P. Lipid domain formation and dynamics

in giant unilamellar vesicles explored by fluorescence correlation spectroscopy. J Struct Biol. Academic Press; 2004;147: 77–89. doi:10.1016/J.JSB.2003.09.021

91. Sezgin E, Kaiser H-J, Baumgart T, Schwille P, Simons K, Levental I. Elucidating membrane structure and protein behavior using giant plasma membrane vesicles. Nat Protoc. Nature Publishing Group; 2012;7: 1042–1051. doi:10.1038/nprot.2012.059

92. Grove J, Metcalf DJ, Knight AE, Wavre-Shapton ST, Sun T, Protonotarios ED, et al. Flat clathrin lattices: stable features of the plasma membrane. Mol Biol Cell. American Society for Cell Biology; 2014;25: 3581–94. doi:10.1091/mbc.E14-06-1154

93. Wilson BS, Pfeiffer JR, Raymond-Stintz MA, Lidke D, Andrews N, Zhang J, et al. Exploring Membrane Domains Using Native Membrane Sheets and Transmission Electron Microscopy. Humana Press; 2007. pp. 245–261. doi:10.1007/978-1-59745-513-8_17

94. Plowman SJ, Hancock JF. Ras signaling from plasma membrane and endomembrane microdomains. 2005; doi:10.1016/j.bbamcr.2005.06.004

95. Saxton MJ, Jacobson K. SINGLE-PARTICLE TRACKING:Applications to Membrane Dynamics. Annu Rev Biophys Biomol Struct. 1997;26: 373–399. doi:10.1146/annurev.biophys.26.1.373

96. Dufrêne YF, Ando T, Garcia R, Alsteens D, Martinez-Martin D, Engel A, et al. Imaging modes of atomic force microscopy for application in molecular and cell biology. Nat Nanotechnol. Nature Publishing Group; 2017;12: 295–307. doi:10.1038/nnano.2017.45

97. Usukura E, Narita A, Yagi A, Ito S, Usukura J. An Unroofing Method to Observe the Cytoskeleton Directly at Molecular Resolution Using Atomic Force Microscopy. Sci Rep. Nature Publishing Group; 2016;6: 27472. doi:10.1038/srep27472

98. Hell SW, Wichmann J. Breaking the diffraction resolution limit by stimulated emission: Stimulated-emission-depletion fluorescence microscopy. Opt Lett. 1994;19. Available: http://citeseerx.ist.psu.edu/viewdoc/download?doi=10.1.1.555.6285&rep=rep1&type=pdf

99. Gustafsson MGL. Surpassing the lateral resolution limit by a factor of two using structured illumination microscopy. SHORT COMMUNICATION. J Microsc. Blackwell Science Ltd; 2000;198: 82–87. doi:10.1046/j.1365-2818.2000.00710.x

100. Bailey B, Farkas DL, Taylor DL, Lanni F. Enhancement of axial resolution in fluorescence microscopy by standing-wave excitation. Nature. Nature Publishing Group; 1993;366: 44–48. doi:10.1038/366044a0

101. Rust MJ, Bates M, Zhuang X. Sub-diffraction-limit imaging by stochastic optical reconstruction microscopy (STORM). Nat Methods. 2006;3: 793–5.

doi:10.1038/nmeth929

102. Betzig E, Patterson GH, Sougrat R, Lindwasser OW, Olenych S, Bonifacino JS, et al. Imaging intracellular fluorescent proteins at nanometer resolution. Science. 2006;313: 1642–5. doi:10.1126/science.1127344

103. Jungmann R, Avendaño MS, Woehrstein JB, Dai M, Shih WM, Yin P. Multiplexed 3D cellular super-resolution imaging with DNA-PAINT and Exchange-PAINT. Nat Methods. Nature Publishing Group; 2014;11: 313–318. doi:10.1038/nmeth.2835

104. Thompson RE, Larson DR, Webb WW. Precise Nanometer Localization Analysis for Individual Fluorescent Probes. Available: https://www.ncbi.nlm.nih.gov/pmc/articles/PMC1302065/pdf/11964263.pdf

105. Xu K, Zhong G, Zhuang X. Actin, spectrin, and associated proteins form a periodic cytoskeletal structure in axons. Science. 2013;339: 452–6. doi:10.1126/science.1232251

106. Manley S, Gillette JM, Patterson GH, Shroff H, Hess HF, Betzig E, et al. High-density mapping of single-molecule trajectories with photoactivated localization microscopy. Nat Methods. Nature Publishing Group; 2008;5: 155–157. doi:10.1038/nmeth.1176

107. Kopek BG, Shtengel G, Grimm JB, Clayton D a, Hess HF. Correlative photoactivated localization and scanning electron microscopy. PLoS One. 2013;8: e77209. doi:10.1371/journal.pone.0077209

108. Watanabe S, Punge A, Hollopeter G, Willig KI, Hobson RJ, Davis MW, et al. Protein localization in electron micrographs using fluorescence nanoscopy. Nat Methods. 2011;8: 80–4. doi:10.1038/nmeth.1537

109. Kim D, Deerinck TJ, Sigal YM, Babcock HP, Ellisman MH, Zhuang X. Correlative stochastic optical reconstruction microscopy and electron microscopy. PLoS One. 2015;10: 1–20. doi:10.1371/journal.pone.0124581

110. Segala MGP, Sun MG, Shtengel G, Viswanathan S, Baird MA, Macklin JJ, et al. Fixation-resistant photoactivatable fluorescent proteins for correlative light and electron microscopy. Nat Methods. 2015;12: 215–218.

111. Chang Y-W, Chen S, Tocheva EI, Treuner-Lange A, Löbach S, Søgaard-Andersen L, et al. Correlated cryogenic photoactivated localization microscopy and cryo-electron tomography. Nat Methods. 2014;11: 737–739. doi:10.1038/nmeth.2961

112. Johnson E, Seiradake E, Jones EY, Davis I, Grünewald K, Kaufmann R. Correlative in-resin super-resolution and electron microscopy using standard fluorescent proteins. Sci Rep. 2015;5: 9583. doi:10.1038/srep09583

113. Perkovic M, Kunz M, Endesfelder U, Bunse S, Wigge C, Yu Z, et al. Correlative Light- and Electron Microscopy with chemical tags. J Struct Biol. Elsevier Inc.; 2014;186: 205–213. doi:10.1016/j.jsb.2014.03.018

114. Zhang Y, Huang T, Jorgens DM, Nickerson A, Lin L-J, Pelz J, et al. Quantitating morphological changes in biological samples during scanning electron microscopy sample preparation with correlative super-resolution microscopy. Abraham T, editor. PLoS One. Public Library of Science; 2017;12: e0176839. doi:10.1371/journal.pone.0176839

115. Schnell U, Dijk F, Sjollema KA, Giepmans BNG. Immunolabeling artifacts and the need for live-cell imaging. Nat Methods. Nature Research; 2012;9: 152–158. doi:10.1038/nmeth.1855

116. Talbot MJ, White RG. Methanol fixation of plant tissue for Scanning Electron Microscopy improves preservation of tissue morphology and dimensions. Plant Methods. BioMed Central; 2013;9: 36. doi:10.1186/1746-4811-9-36

117. Hochberg R, Litvaitis MK. Hexamethyldisilazane for scanning electron microscopy of Gastrotricha. Biotech Histochem. 2000;75: 41–4. Available: http://www.ncbi.nlm.nih.gov/pubmed/10810982

118. Gusnard D, Kirschner RH. Cell and organelle shrinkage during preparation for scanning electron microscopy: effects of fixation, dehydration and critical point drying. J Microsc. 1977;110: 51–7. Available: http://www.ncbi.nlm.nih.gov/pubmed/409847

119. Nation JL. A New Method Using Hexamethyldisilazane for Preparation of Soft Insect Tissues for Scanning Electron Microscopy. Stain Technol. Taylor & Francis; 2009; Available: http://www.tandfonline.com/doi/abs/10.3109/10520298309066811

120. Boyde A, Weiss RA, Veselý P. Scanning electron microscopy of cells in culture. Exp Cell Res. 1972;71: 313–324. doi:10.1016/0014-4827(72)90299-6

121. Arborgh B, Bell P, Brunk U, Collins VP. The osmotic effect of glutaraldehyde during fixation. A transmission electron microscopy, scanning electron microscopy and cytochemical study. J Ultrastruct Res. 1976;56: 339–350. doi:10.1016/S0022-5320(76)90009-5

122. Pathan AK, Bond J, Gaskin RE. Sample preparation for SEM of plant surfaces. Mater Today. 2010;12: 32–43. doi:10.1016/S1369-7021(10)70143-7

123. Nation JL. A new method using hexamethyldisilazane for preparation of soft insect tissues for scanning electron microscopy. Stain Technol. 1983;58: 347–51. Available: http://www.ncbi.nlm.nih.gov/pubmed/6679126

124. Moran P, Coats B. Biological Sample Preparation for SEM Imaging of Porcine Retina. Micros Today. 2012;20: 28–31. doi:10.1017/S1551929511001374

125. Leser V, Drobne D, Pipan Z, Milani M, Tatti F. Comparison of different preparation methods of biological samples for FIB milling and SEM investigation. J Microsc. 2009;233: 309–19. doi:10.1111/j.1365-2818.2009.03121.x

126. Nordestgaard BG, Rostgaard J. Dimensional changes of isolated hepatocytes during processing for scanning and transmission electron microscopy. Micron

Microsc Acta. 1985;16: 65–75. doi:10.1016/0739-6260(85)90035-8

127. Nordestgaard BG, Rostgaard J. Critical-point drying versus freeze drying for scanning electron microscopy: a quantitative and qualitative study on isolated hepatocytes. J Microsc. 1985;137: 189–207. doi:10.1111/j.1365-2818.1985.tb02577.x

128. Penttila A, Kalimo H, Trump BF. Influence of glutaraldehyde and-or osmium tetroxide on cell volume, ion content, mechanical stability, and membrane permeability of Ehrlich ascites tumor cells. J Cell Biol. 1974;63: 197–214. Available: http://www.pubmedcentral.nih.gov/articlerender.fcgi?artid=2109340&tool=pmcentrez&rendertype=abstract

129. Rostgaard J, Frederiksen O. Fluid transport and dimensions of epithelial cells and intercellular spaces in frog gallbladder. Cell Tissue Res. 1981;215. doi:10.1007/BF00239111

130. Rostgaard J, Tranum-Jensen J. A procedure for minimizing cellular shrinkage in electron microscope preparation: a quantitative study on frog gall bladder. J Microsc. 1980;119: 213–232. doi:10.1111/j.1365-2818.1980.tb04091.x

131. Bahr GF, Bloom G, Friberg U. Volume changes of tissues in physiological fluids during fixation in osmium tetroxide or formaldehyde and during subsequent treatment. Exp Cell Res. 1957;12: 342–355. doi:10.1016/0014-4827(57)90148-9

132. Coetzee J, Merwe CF. The osmotic effect of glutaraldehyde-based fixatives on plant storage tissue. J Microsc. 1986;141: 111–118. doi:10.1111/j.1365-2818.1986.tb02705.x

133. Xu K, Zhong G, Zhuang X. Actin, spectrin, and associated proteins form a periodic cytoskeletal structure in axons. Science. 2013;339: 452–6. doi:10.1126/science.1232251

134. Edelstein A, Amodaj N, Hoover K, Vale R, Stuurman N, Edelstein A, et al. Computer Control of Microscopes Using μManager. Current Protocols in Molecular Biology. Hoboken, NJ, USA: John Wiley & Sons, Inc.; 2010. p. 14.20.1-14.20.17. doi:10.1002/0471142727.mb1420s92

135. Demignot S, Domurado D. Elimination of artifacts due to glutaraldehyde fixation in the histochemical detection of glucose oxidase with tetrazolium salts. Histochem J. 1988;20: 11–8. Available: http://www.ncbi.nlm.nih.gov/pubmed/2453488

136. Garcia-Patrone M, Algranati ID. Artifacts induced by glutaraldehyde fixation of ribosomal particles. Mol Biol Rep. Kluwer Academic Publishers; 1976;2: 507–515. doi:10.1007/BF00356940

137. Karnovsky MJ, Karnovsky M, Karnovsky M, Karnovsky MJ, Karnovsky MJ. A formaldehyde-glutaraldehyde fixative of high osmolarity for use in electron microscopy. 1965.

138. Wheatgerm agglutinin toxicity in pancreatic cancer 1755. Br J Cancer. 1999;80: 1754–1762.

139. RIEMERSMA JC. OSMIUM TETROXIDE FIXATION OF LIPIDS: NATURE OF THE REACTION PRODUCTS. J Histochem Cytochem. SAGE Publications; 1963;11: 436–442. doi:10.1177/11.3.436

140. Zaidel-Bar R, Cohen M, Addadi L, Geiger B. Hierarchical assembly of cell-matrix adhesion complexes. Biochem Soc Trans. 2004;32: 416–20. doi:10.1042/BST0320416

141. Huang F, Sirinakis G, Allgeyer ES, Toomre D, Booth MJ, Bewersdorf J, et al. Ultra-High Resolution 3D Imaging of Whole Cells Resource Ultra-High Resolution 3D Imaging of Whole Cells. Cell. The Authors; 166: 1028–1040. doi:10.1016/j.cell.2016.06.016

142. Araujo JC, Téran FC, Oliveira RA, Nour EAA, Montenegro MAP, Campos JR, et al. Comparison of hexamethyldisilazane and critical point drying treatments for SEM analysis of anaerobic biofilms and granular sludge. J Electron Microsc (Tokyo). Oxford University Press; 2003;52: 429–33. doi:10.1093/JMICRO/52.4.429

143. Hazrin-Chong NH, Manefield M. An alternative SEM drying method using hexamethyldisilazane (HMDS) for microbial cell attachment studies on sub-bituminous coal. J Microbiol Methods. 2012;90: 96–9. doi:10.1016/j.mimet.2012.04.014

144. Santarpia L, Lippman SM, El-Naggar AK. Targeting the MAPK-RAS-RAF signaling pathway in cancer therapy. Expert Opin Ther Targets. NIH Public Access; 2012;16: 103–19. doi:10.1517/14728222.2011.645805

145. Abdellatif M, Schneider MD. An Effector-like Function of Ras GTPase-activating Protein Predominates in Cardiac Muscle Cells*. 1997; Available: http://www-jbc.stanford.edu/jbc/

146. Hancock JF, Cadwallader K, Marshall CJ. Methylation and proteolysis are essential for efficient membrane binding of prenylated p21K-ras(B). EMBO J. 1991;10: 641–646.

147. Hancock JF, Magee AI, Childs JE, Marshall CJ. All ras proteins are polyisoprenylated but only some are palmitoylated. Cell. Cell Press; 1989;57: 1167–1177. doi:10.1016/0092-8674(89)90054-8

148. Prior IA, Harding A, Yan J, Sluimer J, Parton RG, Hancock JF. GTP-dependent segregation of H-ras from lipid rafts is required for biological activity. Nat Cell Biol. Nature Publishing Group; 2001;3: 368–375. doi:10.1038/35070050

149. Plowman SJ, Muncke C, Parton RG, Hancock JF. H-ras, K-ras, and inner plasma membrane raft proteins operate in nanoclusters with differential dependence on the actin cytoskeleton. Proc Natl Acad Sci. 2005;102: 15500–15505. doi:10.1073/pnas.0504114102

150. Yan J, Roy S, Apolloni A, Lane A, Hancock JF. Ras isoforms vary in their ability to activate Raf-1 and phosphoinositide 3-kinase. J Biol Chem. American Society for Biochemistry and Molecular Biology; 1998;273: 24052–6. doi:10.1074/JBC.273.37.24052

151. Janosi L, Li Z, Hancock JF, Gorfe AA. Organization, dynamics, and segregation of Ras nanoclusters in membrane domains. Proc Natl Acad Sci U S A. National Academy of Sciences; 2012;109: 8097–102. doi:10.1073/pnas.1200773109

152. Güldenhaupt J, Rudack T, Bachler P, Mann D, Triola G, Waldmann H, et al. N-Ras Forms Dimers at POPC Membranes. Biophys J. 2012;103: 1585–1593. Available: http://www.sciencedirect.com/science/article/pii/S0006349512009708

153. Zhang Z, Kenny SJ, Hauser M, Li W, Xu K. Ultrahigh-throughput single-molecule spectroscopy and spectrally resolved super-resolution microscopy. Nat Methods. Nature Publishing Group; 2015;12: 935–938. doi:10.1038/nmeth.3528

154. Bates M, Huang B, Dempsey GT, Zhuang X. Multicolor Super-Resolution Imaging with Photo-Switchable Fluorescent Probes. 2007; 1749–1754.

155. Otsu N. A Threshold Selection Method from Gray-Level Histograms. IEEE Trans Syst Man Cybern. 1979;9: 62–66. doi:10.1109/TSMC.1979.4310076

156. Ester M, Kriegel H-P, Sander J, Xu X. A Density-Based Algorithm for Discovering Clusters in Large Spatial Databases with Noise. 1996; Available: www.aaai.org

157. Preta G, Cronin JG, Sheldon IM. Dynasore - not just a dynamin inhibitor. Cell Commun Signal. BioMed Central; 2015;13: 24. doi:10.1186/s12964-015-0102-1

158. Casella JF, Flanagan MD, Lin S. Cytochalasin D inhibits actin polymerization and induces depolymerization of actin filaments formed during platelet shape change. Nature. Nature Publishing Group; 1981;293: 302–305. doi:10.1038/293302a0

159. Roy S, Wyse B, Hancock JF. H-Ras signaling and K-Ras signaling are differentially dependent on endocytosis. Mol Cell Biol. American Society for Microbiology; 2002;22: 5128–40. doi:10.1128/MCB.22.14.5128-5140.2002

160. Sigismund S, Argenzio E, Tosoni D, Cavallaro E, Polo S, Di Fiore PP. Clathrin-Mediated Internalization Is Essential for Sustained EGFR Signaling but Dispensable for Degradation. Dev Cell. Cell Press; 2008;15: 209–219. doi:10.1016/J.DEVCEL.2008.06.012

161. Gowrishankar K, Ghosh S, Saha S, C R, Mayor S, Rao M. Active remodeling of cortical actin regulates spatiotemporal organization of cell surface molecules. Cell. Elsevier; 2012;149: 1353–67. doi:10.1016/j.cell.2012.05.008

162. Barceló C, Paco N, Morell M, Alvarez-Moya B, Bota-Rabassedas N, Jaumot M, et al. Phosphorylation at Ser-181 of oncogenic KRAS is required for tumor growth. Cancer Res. American Association for Cancer Research; 2014;74: 1190–9. doi:10.1158/0008-5472.CAN-13-1750

163. Huang B, Bates M, Zhuang X. Super-resolution fluorescence microscopy. Annu Rev Biochem. 2009;78: 993–1016. doi:10.1146/annurev.biochem.77.061906.092014

164. Huang T, Phelps C, Wang J, Lin L-J, Bittel A, Scott Z, et al. Simultaneous Multicolor Single-Molecule Tracking with Single-Laser Excitation via Spectral Imaging. Biophys J. Elsevier; 2018;114: 301–310. doi:10.1016/j.bpj.2017.11.013

165. Schnitzbauer J, Strauss MT, Schlichthaerle T, Schueder F, Jungmann R. Super-resolution microscopy with DNA-PAINT. Nat Protoc. Nature Publishing Group; 2017;12: 1198–1228. doi:10.1038/nprot.2017.024

166. Gong H, Holcomb I, Ooi A, Wang X, Majonis D, Unger MA, et al. Simple Method To Prepare Oligonucleotide-Conjugated Antibodies and Its Application in Multiplex Protein Detection in Single Cells. Bioconjug Chem. 2016;27: 217–225. doi:10.1021/acs.bioconjchem.5b00613

167. Agasti SS, Wang Y, Schueder F, Sukumar A, Jungmann R, Yin P. DNA-barcoded labeling probes for highly multiplexed Exchange-PAINT imaging. Chem Sci. Royal Society of Chemistry; 2017;8: 3080–3091. doi:10.1039/C6SC05420J